TECHNISCHE UNIVERSITÄT MÜNCHEN
Lehrstuhl für Theoretische Chemie

Monte Carlo wave packet propagators for multidimensional vibrational spectroscopy

Andriy Samsonyuk

Vollständiger Abdruck der von der Fakultät für Chemie der Technischen Universität München zur Erlangung der akademischen Grades eines

Doktors der Naturwissenschaften

genehmigten Dissertation.

Vorsitzender:	Univ.-Prof. Dr. Steffen J. Glaser
Prüfer der Dissertation:	
1.	Univ.-Prof. Dr. Wolfgang Domcke
2.	Univ.-Prof. Dr. Mathias Nest

Die Dissertation wurde am 2. September 2013 bei der Technische Universität München eingereicht und durch die Fakultät für Chemie am 14. Oktober 2013 angenommen.

Contents

Summary

A direct Monte Carlo wave packet sampling method for Liouville space pathways, based on the solution of the quantum stochastic differential equation in a doubled Hilbert space, was developed to widen the scope of nonlinear spectroscopy simulations. Using this method we can: compute third order infrared response functions for systems with thousands of states, which was not possible before; simulate a very broad range of experiments with any number of pulse interactions; reduce the computational cost through selection of „important" perturbative terms represented by Feynman diagrams.

Zusammenfassung

Zur Erweiterung des Anwendungsbereichs der theoretischen Beschreibung mehrdimensionaler Schwingungsspektroskopie durch Pfade im Liouvilleraum wurde, basierend auf der Lösung quantenstochastischer Differentialgleichungen im doppelten Hilbertraum, ein direkter Ansatz zu deren Monte Carlo Wellenpaket Sampling entwickelt. Dieser erlaubt Responsefunktionen höherer Ordnungen für Systeme mit über tausend Konfigurationen zu berechnen, eine große Vielfalt von Experimenten mit beliebiger Anzahl von Wechselwirkungen mit einem externem Feld zu simulieren, sowie den Rechenaufwand durch die Auswahl „wichtiger" Störungsterme (dargestellt durch die Feynman-Diagramme) zu reduzieren.

Резюме

Для расширения возможностей теории нелинейной многомерной спектроскопии мы разработали статистический метод Монте Карло, основаный на решении стохастических дифференциальных уравнений в удвоеном пространстве Гильберта для пространственных путей Лиувиля. Наш метод позволяет: расчитывать функции отклика для систем более тысячи конфигураций, что ранее не было возможно; моделировать эксперементы с любым количеством взаимодействий с электромагнитным полем; уменьшить обём вычислений благодаря выбору „важных" членов, представленых в виде диаграмм Фейнмана.

Chapter A

Introduction

The Guide is definitive. Reality is frequently inaccurate.

Douglas Adams

Multidimensional infrared spectroscopy is a cutting-edge technique that provides us with new insights relevant for a very broad range of disciplines like energy sciences, biophysics, physical chemistry etc. It can be applied to all time-scales observed in chemical processes. For example, its fast time-resolution allows us to follow electron transfer indirectly and solvent dynamics directly. We also can study long time-scale kinetics in a „snapshot" mode. Multidimensional infrared spectroscopy can be applied to different kind of samples like solutions, solid-state systems, or membranes [1]. But the most important advantage of multidimensional vibrational spectroscopy for this work lies in its structural sensitivity, which not only provides us with new insights into the structure and vibrational motion of polyatomic molecules [2, 3] but also gives us information about couplings between different vibrational modes, which is crucial for many biochemical processes [4].

The vibrational spectrum of a sample is determined not only by the three-dimensional structure of the molecules in that sample, but also by their intra- and intermolecular interactions. Therefore, the amount of information about the system studied, which can be retrieved from such spectra, is very high.

The challenge of multidimensional vibrational spectroscopy lies not only in the complicated experimental setup, but also in a very complex theory, whose main limitation is a highly superlinear scaling of the computational effort with system size. For that reason, to the best of our knowledge, it is so far applicable to small model systems or with very crude approximations only [2].

In this work we aim to go beyond the model system approach and to develop an approximative method that allows for the computation of vibrational 2D spectra for molecular systems with more than 1000 dimensional Hamiltonian matrices.

Because of the superlinear scaling of the computational effort of the Liouville space based methods, we have to move away from the exact solution of the master equation and focus on approximations based on the quantum stochastic differential equation in Hilbert space.

In Chap. B we are going to survey the state-of-the-art of the theory behind vibrational spectroscopy. We will start with a comparison between the Hilbert and Liouville space based formalisms. Then we will introduce matter-light interaction and formally solve the resulting master equation. In the next step we will present the perturbative approach for computation of the response functions. An interaction with the environment will be presented semi-classically and in form of the Lindblad formalism. Having done that we will show the equality of a quantum stochastic differential equation and the master equation based on [5]. We describe the doubled Hilbert space propagators and introduce a Monte Carlo sampling algorithm as a stochastic quantum jump approach for vibrational spectroscopy. The Monte Carlo sampling algorithm is new and its development is based on results from [6–12].

In Chap. C we will test the theory and implementation for some well understood benchmark systems. We start with a single harmonic oscillator, compute its first order response functions in time and frequency domains and introduce line broadening. As our next step we will examine third order response functions in a perturbative way. We represent the perturbative terms as double-sided Feynman diagrams and introduce low temperature and rotating wave approximations to reduce the number of terms. The distinct choice of an experiment gives us further possibilities of term selection due to the different detection directions of the rephasing and non-rephasing signals. Anharmonicity is introduced and the number of oscillators is increased to three. We observe the anharmonic and cross-peaks in 2D spectra. Since the applicability of the exact propagation for three (an-)harmonic oscillators in the Lindblad formalism is reaching its limit we implement a parallel version of the Chebyshev polynomial propagator for the Liouville and Hilbert space based methods. We examine the semiclassical approximation as a very practical approach for computing (in-)homogeneous dephasing. We introduce the relaxation matrix and solve the resulting stochastic differential equations in doubled Hilbert space for the same benchmark systems.

In Chap. D we proceed with applications on „real" molecular systems. We have chosen the water and formamide molecules for testing purposes. The Hamiltonian and dipole matrices were computed with quantum chemistry programs. At this point we are interested in the general applicability of the method and not in absolute values of the matrix elements, therefore no computationally expensive quantum chemical methods were used in this work. Both first and third order response functions for the sum of the rephasing and non-rephasing signals were

computed.

In Chap. E we present the result of a joint work with the experimental group of Tobias Steinel. The measured linear FTIR spectrum of 2-pyrrolidinone deviated from the initial theoretical predictions. The deviation of the spectra occurs because of aggregation effects in solution. We developed a vibrational tight-binding model to describe those effects. The results presented in Chap. E were published in Ref. [13].

Chapter B

„Need to know"s

B.01 Hilbert space

A time-dependent state of a quantum mechanical system can be described by a wavefunction $|\psi(t)\rangle$. To define a linear vector space, called Hilbert space, we define an addition (superposition) and scalar multiplication operations as

$$|\psi(t)\rangle = c_a |\psi_a\rangle + c_b |\psi_b\rangle , \quad c_a, c_b \in \mathbb{C},$$

where $\psi_{a,b}$ are orthonormal eigenfunctions of the time independent Hamilton operator

$$H |\psi_k\rangle = \epsilon_k |\psi_k\rangle , \quad k = a, b, \ldots$$

and

$$\langle \psi_a \mid \psi_b \rangle = \delta_{ab}, \tag{B.01.1}$$

where δ_{ab} is the Kronecker delta function

$$\delta_{ab} = \begin{cases} 1, & a = b \\ 0, & a \neq b \end{cases} . \tag{B.01.2}$$

The scalar product in the Eq. (B.01.1) is defined as

$$\langle \psi_a(\mathbf{x}) \mid \psi_b(\mathbf{x}) \rangle = \int \psi_a^*(\mathbf{x}) \psi_b(\mathbf{x}) \mathrm{d}\mathbf{x} \tag{B.01.3}$$

for more precise definitions see Ref. [4] and references therein.

The expectation value of a dynamical variable A in the Schrödinger picture is given by

$$\langle \psi(t) |A| \phi(t) \rangle = \int \psi^*(\mathbf{x}, t) A \phi(\mathbf{x}, t) \mathrm{d}\mathbf{x}. \tag{B.01.4}$$

To obtain the wavefunction ($|\psi(t)\rangle$) as a function of time the Schrödinger equation has to be solved

$$i\hbar\frac{\partial|\psi\rangle}{\partial t} = \widehat{H}(t)|\psi\rangle\,, \tag{B.01.5}$$

where $\widehat{H}$ is the, in general time-dependent, total Hamiltonian of the system.

We introduce the evolution operator $\widehat{U}(t,t_0)$, which acts on the wavefunction at the t_0 and transforms it to the wavefunction at t.

$$|\psi(t)\rangle = \widehat{U}(t,t_0)|\psi(t_0)\rangle \tag{B.01.6}$$

$\widehat{U}(t_0,t_0)$ is defined to be the a unity operator ($|\psi(t_0)\rangle = \widehat{U}(t_0,t_0)|\psi(t_0)\rangle$).

Inserting equation (B.01.6) into equation (B.01.5) yields

$$i\hbar\frac{\partial\widehat{U}(t,t_0)|\psi(t_0)\rangle}{\partial t} = \widehat{H}(t)\widehat{U}(t,t_0)|\psi(t_0)\rangle\,, \tag{B.01.7}$$

which leads us to

$$i\hbar\frac{\partial\widehat{U}(t,t_0)}{\partial t} = \widehat{H}(t)\widehat{U}(t,t_0). \tag{B.01.8}$$

Since equation (B.01.7) must hold for any initial $|\psi(t_0)\rangle$. Integrating this equation results in

$$\widehat{U}(t,t_0) = 1 - \frac{i}{\hbar}\int_{t_0}^{t}\widehat{H}(\tau)\widehat{U}(\tau,t_0)\mathrm{d}\tau. \tag{B.01.9}$$

by plugging this equation into itself and solving it iteratively we obtain

$$\widehat{U}(t,t_0) = 1 + \sum_{n=1}^{\infty}\left(\frac{i}{\hbar}\right)^n\int_{t_0}^{t}\mathrm{d}\tau_n\int_{t_0}^{\tau_n}\mathrm{d}\tau_{n-1}\cdots\int_{t_0}^{\tau_2}\mathrm{d}\tau_1\widehat{H}(\tau_n)\widehat{H}(\tau_{n-1})\cdots\widehat{H}(\tau_1). \tag{B.01.10}$$

If the Hamilton operators at different times commute, then the time ordering is not of a concern and we can write the r.h.s. of Eq. (B.01.10) as

$$\widehat{U}(t,t_0) = \exp\left\{-\frac{i}{\hbar}\int_{t_0}^{t}\mathrm{d}\tau\widehat{H}(\tau)\right\}. \tag{B.01.11}$$

At this point it turns out to be very useful to define the interaction picture and to transform Eq. (B.01.11) accordingly. In the interaction picture the total Hamiltonian consists of two parts

$$\widehat{H}(t) = \widehat{H}_0(t) + \widehat{H}'(t) \tag{B.01.12}$$

$\widehat{H}_0$ is a simple Hamiltonian and its time evolution can be calculated exactly. $\widehat{H}'(t)$ is a more complicated contribution and is treated perturbatively. The relation

between wavefunctions in the Schrödinger (ψ_S) and the interaction (ψ_I) picture, respectively, is presented in the following equation

$$\begin{aligned} |\psi_S(t)\rangle =& \widehat{U}_0(t,t_0)\,|\psi_I(t)\rangle \\ =& \widehat{U}_0(t,t_0)\widehat{U}_I(t,t_0)\,|\psi_I(t_0)\rangle \\ =& \widehat{U}_0(t,t_0)\widehat{U}_I(t,t_0)\,|\psi_S(t_0)\rangle \end{aligned} \tag{B.01.13}$$

The derivation of the final expression for the evolution is straightforward and therefore we will only present the result for the not time ordered expression, with the integration variables $\mathrm{d}\tau_1, \ldots, \mathrm{d}\tau_n$ (see [4] for further details).

$$\begin{aligned} \widehat{U}(t,t_0) =& \sum_{n=0}^{\infty} \left(-\frac{i}{\hbar}\right)^n \int_{t_0}^{t} \mathrm{d}\tau_n \cdots \int_{t_0}^{\tau_2} \mathrm{d}\tau_1 \\ & \widehat{U}_0(t,\tau_n)\widehat{H}'(\tau_n)\cdots\widehat{U}_0(\tau_2,\tau_1)\widehat{H}'(\tau_1)\widehat{U}_0(\tau_1,t_0) \end{aligned} \tag{B.01.14}$$

In this equation the free propagation of the system under the system Hamiltonian $\widehat{U}_0$ and interaction with the perturbation $\widehat{H}'$ are subsequent. This result will be used to describe the dynamics of the system combined with field interaction.

B.02 Liouville space

A wavefunction describes the system in a pure state. However, a general state of a system may be an ensemble, which consists of a distribution of pure states. Such a system can be described by a density matrix [14]

$$\rho(t) = \sum_k P_k\,|\psi_k(t)\rangle\,\langle\psi_k(t)| \tag{B.02.1}$$

where $P_k \geq 0$ is the probability to find the system in a state $|\psi_k(t)\rangle$ with normalization $\sum_k P_k = 1$. If P_k is equal 1 for one particular value of k and 0 for every other value of k, then the system is in a pure state. Otherwise the state of the system is incompletely defined (mixed state).

In the case of density matrices the expectation value of an arbitrary operator A can be computed as (compare with Eq. (B.01.4))

$$\langle A(t)\rangle = \langle\langle A\,|\,\rho(t)\rangle\rangle = \mathrm{tr}\left\{A^\dagger\rho(t)\right\}, \tag{B.02.2}$$

where $A^\dagger$ is the adjoint (conjugate transpose) of the operator A and $\mathrm{tr}\{\cdot\}$ is the

trace operation

$$\begin{aligned} \mathrm{tr}\left\{A^\dagger B\right\} &= \sum_m \left(\sum_n \left(\mathbf{A}^\dagger\right)_{mn} \mathbf{B}_{nm} \right) \\ &= \sum_m \left(\sum_n \mathbf{A}^*_{nm} \mathbf{B}_{nm} \right) \\ &= \langle \mathrm{vec}\left(\mathbf{A}\right) \mid \mathrm{vec}\left(\mathbf{B}\right) \rangle , \end{aligned} \tag{B.02.3}$$

where $\mathrm{vec}\left(\cdot\right)$ is the vectorization operator [15]. The expression $\langle\langle \cdot \mid \cdot \rangle\rangle$ defines a scalar product in Liouville space. For further details on the properties of Liouville and Hilbert spaces we recommend Ref. [4, 16] and references therein.

The time evolution of the density operator can be described with the quantum Liouville equation (Liouville – von Neumann equation)

$$\begin{aligned} i\hbar \frac{\partial \rho}{\partial t} &= \mathcal{L}\rho \\ &= \widehat{H}\rho - \rho\widehat{H} \\ &= \left[\widehat{H}, \rho\right] \end{aligned} \tag{B.02.4}$$

The formal solution of this equation is given by

$$\rho(t) = \widehat{U}(t, t_0)\rho(t_0)\widehat{U}^\dagger(t, t_0). \tag{B.02.5}$$

In equation (B.02.5) we implicitly defined the Liouville space propagator

$$\rho(t) = \mathcal{U}(t, t_0)\rho(t_0). \tag{B.02.6}$$

We can solve the time dependent Schrödinger equation for the operator $\mathcal{U}(t, t_0)$ as it was done in Eq. (B.01.8)

$$i\hbar \frac{\partial \mathcal{U}(t, t_0)}{\partial t} = \mathcal{L}(t)\mathcal{U}(t, t_0) \tag{B.02.7}$$

the solution of this equation is

$$\mathcal{U}(t, t_0) \equiv \exp\left\{ -\frac{i}{\hbar}\mathcal{L}(t - t_0) \right\}. \tag{B.02.8}$$

After deriving of the Liouville space operators, we want to compare them to the previously defined Hilbert space operators.

$$\mathcal{U}(t, t_0)\rho(t_0) \Leftrightarrow \widehat{U}(t, t_0)\rho(t_0)\widehat{U}^\dagger(t, t_0) \tag{B.02.9}$$

$$\exp\left[-\frac{i}{\hbar}\mathcal{L}(t) \right] \rho(0) \Leftrightarrow \exp\left[-\frac{i}{\hbar}\widehat{H}t \right] \rho(0) \exp\left[\frac{i}{\hbar}\widehat{H}t \right] \tag{B.02.10}$$

Switching to the interaction picture

$$\mathcal{L}(t) = \mathcal{L}_0(t) + \mathcal{L}'(t) \tag{B.02.11}$$

in complete analogy to Sec. B.01, we get the not time ordered expansion for the evolution operator ($\mathcal{U}(t, t_0)$) in Liouville space

$$\begin{aligned}\mathcal{U}(t, t_0) =& \mathcal{U}_0(t, t_0) + \sum_{n=1}^{\infty} \left(-\frac{i}{\hbar}\right)^n \int_{t_0}^{t} \mathrm{d}\tau_n \cdots \int_{t_0}^{\tau_2} \mathrm{d}\tau_1 \\ & \mathcal{U}_0(t, \tau_n)\mathcal{L}'(\tau_n) \cdots \mathcal{U}_0(\tau_2, \tau_1)\mathcal{L}'(\tau_1)\mathcal{U}_0(\tau_1, \tau_0),\end{aligned} \tag{B.02.12}$$

which is analogous to Eq. (B.01.14)

B.03 Matter-light interaction

We have already considered a time evolution of the system using Hilbert and Liouville space formulations. Now we want to describe an interaction with a radiation field.

The interaction Hamiltonian in the dipole approximation, also known as long wavelength approximation (LWA), has the following form

$$\begin{aligned}\widehat{H}_{\mathrm{int}}(t) &= -E(\mathbf{r}, t)\widehat{\mu} \\ \mathcal{L}_{\mathrm{int}}(t) &= -E(\mathbf{r}, t)\mathcal{M},\end{aligned} \tag{B.03.1}$$

where $\mathcal{M}A = [\widehat{\mu}, A]$.

The total Hamilton operator therefore becomes

$$\widehat{H}(t) = \widehat{H}_0 + \widehat{H}_{\mathrm{int}}(t) \tag{B.03.2}$$

and the Liouville – von Neumann equation (B.02.4) will become (compare to Eq. (B.02.11))

$$\begin{aligned}i\hbar\frac{\mathrm{d}\rho}{\mathrm{d}t} &= \mathcal{L}(t)\rho = \mathcal{L}_0\rho + \mathcal{L}_{\mathrm{int}}(t)\rho \\ &= \left[\widehat{H}_0, \rho\right] + \left[\widehat{H}_{\mathrm{int}}(t), \rho\right]\end{aligned} \tag{B.03.3}$$

The equations (B.03.2) and (B.03.3) have a form suited for the perturbative approach introduced by the interaction picture in sections B.01 and B.02.

B.04 Hilbert vs. Liouville space formulation

Having derived a total system Hamiltonian for Hilbert and Liouville formalism in Eqs. (B.03.2) and (B.03.3), we can compare both of them.

In most experimental setups we are dealing with ensembles of particles and therefore mixed states. The Liouville space time propagation can handle mixed states exactly but for the price of greater computational cost. The corresponding Hilbert space methods are cheaper, but require further considerations to describe mixed states.

We use Eqs. (B.02.6) and (B.02.12), setting $\mathcal{L}'(t) = \mathcal{L}_{\text{int}}(t)$ from Eq. (B.03.1) and change the time variables to

$$t_1 \equiv \tau_2 - \tau_1, \quad t_2 \equiv \tau_3 - \tau_2, \ldots \quad , t_n \equiv t - \tau_n.$$

Further we can set $t_0 \to -\infty$, since we start with the equilibrium density operator and it does not evolve with time when subject to the material Hamiltonian without field $\mathcal{G}(\tau_1 - t_0)\rho(t_0) = \rho(t_0)$. Assuming an n-th order interaction with light pulses and changing the time variables as described above, we will get an expression:

$$\begin{aligned} \rho^{(n)}(\mathbf{r},t) = \left(\frac{i}{\hbar}\right)^n \int_0^\infty \mathrm{d}t_n \ldots \int_0^\infty \mathrm{d}t_1 \\ E(\mathbf{r}, t - t_n) \ldots E(\mathbf{r}, t - t_1 - \ldots - t_n) \\ \mathcal{G}(t_n)\mathcal{M} \ldots \mathcal{G}(t_1)\mathcal{M} \left|\psi(-\infty)\right\rangle \left\langle\psi(-\infty)\right| , \end{aligned} \tag{B.04.1}$$

where $t_n > 0$ are time intervals between successive interactions and

$$\mathcal{G}(t) = \theta(t) \exp\left(-\frac{i}{\hbar}\mathcal{L}t\right), \tag{B.04.2}$$

with the Heavyside step function

$$\theta(t) = \begin{cases} 1, & t \geq 0 \\ 0, & t < 0 \end{cases} \tag{B.04.3}$$

Since the dipole operators $\mathcal{M}$ are commutators, we have 2^n terms in our n-th order dipole correlation function.

The corresponding expressions for the wavefunctions are

$$\begin{aligned} \left|\psi^{(0)}(\mathbf{r},t)\right\rangle &= \left|\psi(-\infty)\right\rangle \\ \left|\psi^{(1)}(\mathbf{r},t)\right\rangle &= \left(\frac{i}{\hbar}\right) \int_{-\infty}^{t} \mathrm{d}\tau_1 E(\mathbf{r},\tau_1) G(t-\tau_1)\widehat{\mu} \left|\psi(-\infty)\right\rangle \\ &\vdots \\ \left|\psi^{(n)}(\mathbf{r},t)\right\rangle &= \left(\frac{i}{\hbar}\right)^n \int_{-\infty}^{t} \mathrm{d}\tau_n \ldots \int_{-\infty}^{\tau_2} \mathrm{d}\tau_1 E(\mathbf{r},\tau_1) \ldots E(\mathbf{r},\tau_n) \\ &\qquad G(t-\tau_n)\widehat{\mu} \ldots G(\tau_2 - \tau_1)\widehat{\mu} \left|\psi(-\infty)\right\rangle , \end{aligned} \tag{B.04.4}$$

where

$$G(t) = \theta(t) \exp\left(-\frac{i}{\hbar}\widehat{H}t\right). \tag{B.04.5}$$

If we want to construct the density matrix that describes the n-th order light interaction out of wavefunctions, we have to consider every ket-bra $\left|\psi^{(k)}\right\rangle\left\langle\psi^{(n-k)}\right|$ term in the following equation, whose sum over left and right order is equal to n

$$\begin{aligned}\rho^{(n)}(\mathbf{r},t) =& c_0 \left|\psi^{(n)}(\mathbf{r},t)\right\rangle\left\langle\psi^{(0)}(\mathbf{r},t)\right| + c_1 \left|\psi^{(n-1)}(\mathbf{r},t)\right\rangle\left\langle\psi^{(1)}(\mathbf{r},t)\right| + \ldots \\ &+ c_n \left|\psi^{(0)}(\mathbf{r},t)\right\rangle\left\langle\psi^{(n)}(\mathbf{r},t)\right|\end{aligned} \tag{B.04.6}$$

Obviously, we have only $n+1$ terms in the sum of the Eq. (B.04.6) in comparison to 2^n terms of the Eq. (B.04.1). This discrepancy lies in the fact that in the case of multiple time variables acting on bra and ket we will have to split single terms, considering every possible time ordering between them, which is not an issue of the Liouville space formulation.

In the Liouville space formulation we maintain a simultaneous bookkeeping of the interactions with the ket and with the bra and each of the resulting terms has a complete well-defined time ordering.

Each time ordering is calculated as a distinct Liouville space pathway (see Sec. B.06), which is not the case in the Hilbert space formalism, where different terms only reflect the order of the interactions within the bra and the ket (but not the relative time ordering of bra and ket interactions)

B.05 Response functions

Electronic and nuclear motions and relaxation processes will show up in optical measurements only through their effect on the optical polarization $P(\mathbf{r},t)$, which is the only material quantity that appears in the Maxwell equations. Therefore the calculation of $P(\mathbf{r},t)$ is the main goal of any theory of optical spectroscopy.

Having introduced Eq. (B.04.1), the value of $P(\mathbf{r},t)$ is given by the expectation value of the dipole operator $\widehat{\mu}$

$$P(\mathbf{r},t) = \langle\langle\widehat{\mu}\,|\,\rho(t)\rangle\rangle\,. \tag{B.05.1}$$

The polarization function (B.05.1) can be expanded in powers of the radiation field $E(\mathbf{r},t)$

$$P(\mathbf{r},t) = P^{(1)}(\mathbf{r},t) + P^{(2)}(\mathbf{r},t) + P^{(3)}(\mathbf{r},t) + \ldots \tag{B.05.2}$$

with

$$P^{(n)}(\mathbf{r},t) = \left\langle\left\langle\widehat{\mu}\,\right|\,\rho^{(n)}(t)\right\rangle\right\rangle \tag{B.05.3}$$

Each order in the expansion (B.05.2) represents a different class of optical measurements. $P^{(1)}$ is responsible for linear effects, whereas $P^{(2)}$ and $P^{(3)}$ are responsible for second- and third-order nonlinear processes respectively. We are especially interested in the computation of $P^{(1)}$ and $P^{(3)}$, which will be used to describe linear absorption and 2D-spectra.

$P^{(2)}$ vanishes in an isotropic medium because of its symmetry. This is valid for all even order response functions, because if the direction of all fields acting on the response function is reversed, then the polarization will reverse its direction $P^{(2n)} \to -P^{(2n)}$. On the other hand, since E^{2n} (see Eq. (B.03.1)) does not change its sign $P^{(2n)} \to P^{(2n)}$. This is possible only when $P^{(2n)}$ vanishes.

If we insert Eq. (B.04.1) into expression (B.05.3) we obtain

$$P^{(n)}(\mathbf{r},t) = \int_0^\infty \mathrm{d}t_n \ldots \int_0^\infty \mathrm{d}t_1 S^{(n)}(t_n,\ldots,t_1) E(\mathbf{r},t-t_n)\ldots E(\mathbf{r},t-t_1-\ldots-t_n) \tag{B.05.4}$$

with

$$S^{(n)}(t_n,\ldots,t_1) = \left(\frac{i}{\hbar}\right)^n \langle\langle \widehat{\mu}\,|\mathcal{G}(t_n)\mathcal{M}\ldots\mathcal{G}(t_1)\mathcal{M}|\,\rho(-\infty)\rangle\rangle \tag{B.05.5}$$

The complete microscopic information necessary for the computation of optical measurements is carried by the $S^{(n)}$ (n-th order nonlinear response function).

Eq. (B.05.5) can either be evaluated in Liouville space, or as a combination of ordinary correlation functions in Hilbert space.

B.06 Liouville space pathways

As it was mentioned in the Sec. B.04 the response function $S^{(n)}$ contains 2^n terms after all $\mathcal{M}$ commutators are evaluated. We will show, that only half of these terms should be explicitly evaluated, since the other half is simply the complex conjugate of the former. The overall sign of the term is calculated as $(-1)^n$, where n is the number of dipole operator ($\mathcal{M}$) actions from the right, because each time $\mathcal{M}$ acts from the right in a commutator, it carries a minus sign.

Now let us take an explicit look at

$$\begin{aligned}
S^{(1)}(t_1) &= \left(\frac{i}{\hbar}\right) \langle\langle \widehat{\mu} \,|\mathcal{G}(t_1)\mathcal{M}|\, \rho(-\infty)\rangle\rangle \\
&= \left(\frac{i}{\hbar}\right) \theta(t_1) \,\langle\langle \widehat{\mu}(t_1) \,|\mathcal{M}(0)|\, \rho(-\infty)\rangle\rangle \\
&= \left(\frac{i}{\hbar}\right) \theta(t_1) \,\langle [\widehat{\mu}(t_1), \widehat{\mu}(0)]\, \rho(-\infty)\rangle \\
&= \left(\frac{i}{\hbar}\right) \theta(t_1) \,(\langle \widehat{\mu}(t_1)\widehat{\mu}(0)\rho(-\infty)\rangle - \langle \widehat{\mu}(0)\widehat{\mu}(t_1)\rho(-\infty)\rangle) \\
&= \left(\frac{i}{\hbar}\right) \theta(t_1) \,(J(t_1) - J^*(t_1))\,,
\end{aligned} \tag{B.06.1}$$

where

$$J(t_1) \equiv \langle \widehat{\mu}(t_1)\widehat{\mu}(0)\rho(-\infty)\rangle = \langle \widehat{\mu}(t_1)\rho(-\infty)\widehat{\mu}(0)\rangle^* \,. \tag{B.06.2}$$

In analogy to Eq. (B.06.1) we can derive the explicit formulation for the third order nonlinear response function

$$\begin{aligned}
S^{(3)}(t_3,t_2,t_1) &= \left(\frac{i}{\hbar}\right)^3 \langle\langle \widehat{\mu} \,|\mathcal{G}(t_3)\mathcal{M}\mathcal{G}(t_2)\mathcal{M}\mathcal{G}(t_1)\mathcal{M}|\, \rho(-\infty)\rangle\rangle \\
&= \left(\frac{i}{\hbar}\right)^3 \theta(t_1)\theta(t_2)\theta(t_3) \\
&\times \langle [[[\widehat{\mu}(t_3+t_2+t_1), \widehat{\mu}(t_2+t_1)]\,, \widehat{\mu}(t_1)]\,, \widehat{\mu}(0)]\, \rho(-\infty)\rangle \\
&= \left(\frac{i}{\hbar}\right)^3 \theta(t_1)\theta(t_2)\theta(t_3)\Big(\\
&\quad \langle \widehat{\mu}(t_3+t_2+t_1)\widehat{\mu}(t_2+t_1)\widehat{\mu}(t_1)\widehat{\mu}(0)\rho(-\infty)\rangle_{IV} \\
&- \langle \widehat{\mu}(t_2+t_1)\widehat{\mu}(t_3+t_2+t_1)\widehat{\mu}(t_1)\widehat{\mu}(0)\rho(-\infty)\rangle_{III} \\
&- \langle \widehat{\mu}(t_1)\widehat{\mu}(t_3+t_2+t_1)\widehat{\mu}(t_2+t_1)\widehat{\mu}(0)\rho(-\infty)\rangle_{II} \\
&+ \langle \widehat{\mu}(t_1)\widehat{\mu}(t_2+t_1)\widehat{\mu}(t_3+t_2+t_1)\widehat{\mu}(0)\rho(-\infty)\rangle_{I} \\
&- \langle \widehat{\mu}(0)\widehat{\mu}(t_3+t_2+t_1)\widehat{\mu}(t_2+t_1)\widehat{\mu}(t_1)\rho(-\infty)\rangle_{I} \\
&+ \langle \widehat{\mu}(0)\widehat{\mu}(t_2+t_1)\widehat{\mu}(t_3+t_2+t_1)\widehat{\mu}(t_1)\rho(-\infty)\rangle_{II} \\
&+ \langle \widehat{\mu}(0)\widehat{\mu}(t_1)\widehat{\mu}(t_3+t_2+t_1)\widehat{\mu}(t_2+t_1)\rho(-\infty)\rangle_{III} \\
&- \langle \widehat{\mu}(0)\widehat{\mu}(t_1)\widehat{\mu}(t_2+t_1)\widehat{\mu}(t_3+t_2+t_1)\rho(-\infty)\rangle_{IV} \\
&\quad \Big).
\end{aligned} \tag{B.06.3}$$

The numbering of terms in Eq. (B.06.3) is made in accordance with the one used by Mukamel [4]. It is obvious, that terms with the same roman subscripts are

complex conjugates and we can rewrite Eq. (B.06.3) as

$$S^{(3)}(t_3,t_2,t_1) = \left(\frac{i}{\hbar}\right)^3 \theta(t_1)\theta(t_2)\theta(t_3)\sum_{\alpha}\Big(R_\alpha(t_3,t_2,t_1) - R^*_\alpha(t_3,t_2,t_1)\Big), \quad \alpha = I, II, III, IV, \tag{B.06.4}$$

with

$$R_{IV}(t_3,t_2,t_1) = \langle\widehat{\mu}(t_3+t_2+t_1)\widehat{\mu}(t_2+t_1)\widehat{\mu}(t_1)\widehat{\mu}(0)\rho(-\infty)\rangle_{IV}\,, \tag{B.06.5}$$

and so on.

Before we show how the response function can be represented in terms of Feynman diagrams, we introduce the construction rules for the double-sided Feynman diagrams (see Fig. B.1):

(a) The vertical lines represent the time evolution of the density operator. The line on the left represents the ket and the line on the right the bra. Time runs from bottom to top.

(b) Interactions with the field are represented by arrows. The last arrow

$$\left\langle\widehat{\mu}(t_n)\rho^{(n)}\right\rangle$$

is emission from the ket (by convention) and represented by a different arrow. The corresponding diagrams with the emission from the bra do not carry any additional information.

(c) The sign of the diagram is $(-1)^k$, with k the number of interactions from the bra.

(d) An arrow pointing to the right represents an electric field contribution of $\mathrm{e}^{-i\omega_j t + i\mathbf{k}_j\mathbf{r} + i\phi}$ while an arrow pointing to the left represents an electric field contribution of $\mathrm{e}^{i\omega_j t - i\mathbf{k}_j\mathbf{r} - i\phi}$.

(e) Absorption of the light is represented by an arrow pointing to the bra or ket, whereas emission by an arrow pointing away from the bra or ket. Double-sided arrows represent a sum of both interactions.

(f) The last interaction must end in a population state $|f\rangle\langle f|\,, f = 0, 1, \ldots$.

At this point we will assign both terms of Eq. (B.06.1) and four positive terms (since negative terms are simply complex conjugates of the positive terms, they will be left out of the assignment) of the expansion in (B.06.3) to the double-sided Feynman diagrams (see Fig. B.1).

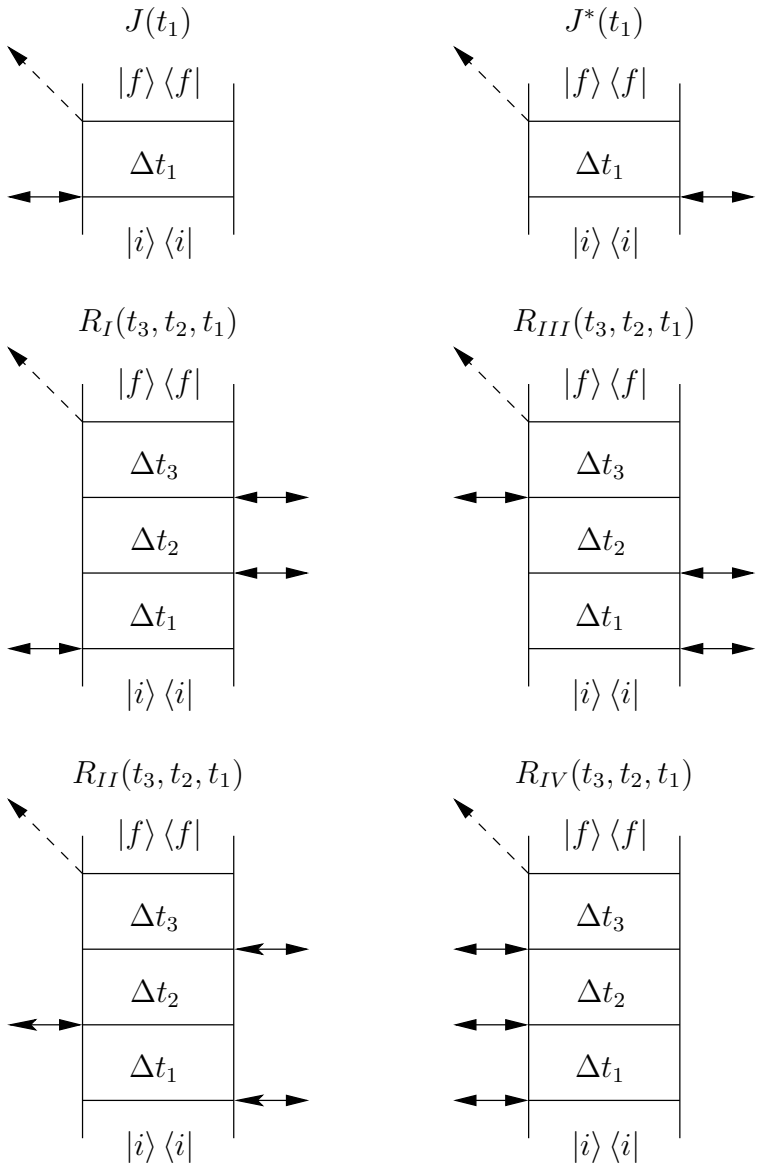

Figure B.1: Double-sided Feynman diagrams representing two terms of equation (B.06.1) and four positive terms of Eq. (B.06.3). The rules to describe the Feynman diagrams can be found on page 20. Δt_n is the time interval between the lower and the upper pulse and equals $t_n - t_{n-1}$. $|i\rangle\langle i|$ is the initial and $|f\rangle\langle f|$ is the final state.

The Feynman diagrams presented in Fig. B.1, are still complex and complicated to evaluate. In the Chap. C we will show what further approximations can be applied to select the response functions responsible for the observed signal [1] and further simplify their computational cost. We will also compute nonlinear signals for different test systems to verify the methodology used in this work.

B.07 Interaction with the environment A: Semiclassical approach

So far we have considered the solution of the master equation for an isolated system. But any system of molecules (or atoms) will interact with its environment (thermal bath).

These interactions are not only time dependent, but every single molecule is generally in a different environment at time t. We therefore have not only to include the frequency time dependence (or time trajectory) of single molecule, but average over a lot of such trajectories. This averaging is usually written as

$$\rho(t) \propto \left\langle \exp\left(-i\int_0^t \omega(\tau)\mathrm{d}\tau\right)\right\rangle \tag{B.07.1}$$

This time dependence of the transition frequency leads to inhomogeneous dephasing. There are a lot of ways of solving the Eq. (B.07.1). One of the most popular approaches is called the semiclassical theory of dephasing and its applicability will be studied in Sec. C.08. This theory treats the vibrational motions quantum mechanically and the inhomogeneous broadening classically [1].

To approximate the exponential in Eq. (B.07.1) one can use a multi-exponential approach, which allows to consider both inhomogeneous and homogeneous spectral broadening separately. To demonstrate the influence of this approach on the peak line shapes in the spectra, we show the real part of the Fourier-transformation (see Sec. C.02) of the first-order response function of the ω_{01} transition. The absorption spectrum

$$\begin{aligned} J(\omega) &\propto \Re\int_0^\infty \mathrm{e}^{i(\omega-\omega_{01})t}\mathrm{e}^{-\frac{t}{T_2^*}}\mathrm{e}^{-\frac{\Delta\omega^2 t^2}{2}}\mathrm{d}t \\ &\propto \frac{1}{(\omega-\omega_{01})^2+\left(\frac{1}{T_2^*}\right)^2}\cdot\mathrm{e}^{-\frac{(\omega-\omega_{01})^2}{2\Delta\omega^2}} \end{aligned} \tag{B.07.2}$$

becomes a Voigt profile [1, 4], which is a convolution of Lorentzian profiles for the homogeneous broadening and a Gaußian distribution function for the inhomogeneous broadening (this can be described as Bloch dynamics). Eq. (B.07.2)

introduces T_2^* and $\Delta\omega$ phenomenologically. The influence of those parameters on the 2D spectrum will be described in detail in Sec. C.08.

For the third order linear response functions in the time domain the exponential factors (compare to Eq. (B.07.2)) are [1]

$$\begin{aligned} R_{1,2,3}(t_3,t_2,t_1) &\propto \mathrm{e}^{-\frac{t_1+t_3}{T_2^*}}\mathrm{e}^{-\frac{\Delta\omega^2(t_1-t_3)^2}{2}} \\ R_{4,5,6}(t_3,t_2,t_1) &\propto \mathrm{e}^{-\frac{t_1+t_3}{T_2^*}}\mathrm{e}^{-\frac{\Delta\omega^2(t_1+t_3)^2}{2}} \end{aligned} \tag{B.07.3}$$

One of the important consequences of Eq. (B.07.3) is the difference between the second exponential function of the so-called rephasing ($R_{1,2,3}$) and non-rephasing ($R_{4,5,6}$) terms. This leads to the observed line narrowing in the antidiagonal direction. One of the reasons of the line narrowing is the correlation between ω_3 and ω_1. The system retains a memory of ω_1 during the ω_3 excitation [1]. The smaller bandwidth represents the inhomogeneous broadening, whereas the larger bandwidth is the sum of the homogeneous and the inhomogeneous one.

Another consequence of the semiclassical approach is its static limit: the line shape is independent of the population time t_2. In this approximation only the evolution of the phase is taken into account and during the population time t_2 time system does not acquire a phase (see [4] for the details).

B.08 Interaction with the environment B: Lindblad-Kossakowski approach

Another degree of sophistication in the description of the interaction with the environment is to take bath degrees of freedom into account [14, 17]. A complete description of the bath and its coupling to the system is rarely feasible and does not necessarily give new insights. A more common approach is to consider the reduced density matrix of the system and trace over the bath degrees of freedom [4]. An even simpler approach is to assume a continuous energy distribution of the bath modes and get phenomenological relaxation rates. For example, if we assume a heat bath of harmonic oscillators, then there has to be a reservoir transition that can absorb or emit a vibrational quantum of any system transition [18].

At this point we can define a system-reservoir interaction operator (relaxation operator) $\widehat{W}$. The relaxation operator is usually represented as a four index tensor. The $W_{m'mn'n}$ element of the relaxation operator describes the transition probability between $\rho_{m'm}$ and $\rho_{n'n}$ averaged over the reservoir degrees of freedom. If $m' = m$ and $n' = n$, we can interpret W_{mmnn} elements as transition rates between populations ρ_{mm} and ρ_{nn} ($W_{mmnn} \propto k_{n\to m}$) induced by the interaction with the reservoir. One important property of the relaxation operator is that it always has to satisfy the following relations [14, 17]:

(a) *Detailed balance*. The reservoir is assumed to be in thermal equilibrium, which is described by the Boltzmann distribution. Therefore the quotient of the transition probabilities between two states is equal to their Boltzmann factor

$$\frac{W_{mmnn}}{W_{nnmm}} = \exp\left\{-\frac{\hbar\omega_{mn}}{k_B T}\right\} \tag{B.08.1}$$

(b) *Conservation of probability*. Let us look, how the population state ρ_{mm} evolves with the time.

$$\dot{\rho}(t)_{mm} = \text{gain in } \rho(t)_{mm} - \text{loss from } \rho(t)_{mm} \tag{B.08.2}$$

The relaxation operator does not change the norm of the system, therefore the total change of the population states must be zero

$$\sum_m \dot{\rho}(t)_{mm} = 0. \tag{B.08.3}$$

Since

$$\sum_m \dot{\rho}(t)_{mm} = \sum_{n'n} \left(\sum_m W_{mmn'n} \right) \rho(t)_{n'n} \tag{B.08.4}$$

and, in general, $\rho_{n'n} \neq 0$

$$\sum_m W_{mmn'n} = 0 \tag{B.08.5}$$

for any n' and n. In other words, if we write the relaxation operator $\widehat{W}$ as a matrix, the sum of each column of elements must be zero.

After the introduction of the system-bath interaction the remaining question is how it will influence the master equation. To answer this question, we have to go back to Eq. (B.02.11). In this equation the $\mathcal{L}_0(t)$ term will gain an additional imaginary contribution

$$\mathcal{L}(t) = \mathcal{L}_0(t) - i\widehat{W}(t) + \mathcal{L}'(t) \tag{B.08.6}$$

There are many approaches to construct the operator $\widehat{W}$. For the dissipative dynamics to be of the Markovian character [5] we will use an approach first proposed by Kossakowski and Lindblad [19, 20]. The derivation of the Kossakowski-Lindblad equations can also be found in [5].

$$\widehat{W}\rho = \sum_k \frac{\gamma_k}{2} \left(2\widehat{\sigma}_k \rho \widehat{\sigma}_k^\dagger - \left[\rho, \widehat{\sigma}_k^\dagger \widehat{\sigma}_k \right]_+ \right) \tag{B.08.7}$$

$\widehat{\sigma}_k$ and $\widehat{\sigma}_k^\dagger$ can be selected as the lowering and raising operators, respectively. As an overview of the quantum mechanics represented in terms of raising and lowering operators we recommend Ref [21]. The rate (probability) of a k process is defined by γ_k. Eq. (B.08.7) expresses the tensor operator $\widehat{W}$ in terms of matrices σ and $\sigma^\dagger$. After the definition of $\widehat{W}$ we can insert the Liouville operator from Eq. (B.08.6) into Eq. (B.02.4).

$$i\hbar\frac{\partial\rho}{\partial t} = \mathcal{L}(t)\rho(t_0) = \left\{\mathcal{L}_0(t) - i\widehat{W}(t) + \mathcal{L}'(t)\right\}\rho(t_0) \tag{B.08.8}$$

We can treat the first two terms of Eq. (B.08.8) the same way we treated $\mathcal{L}_0$ in Sec. B.02. Doing this, we will obtain a new expression for the time evolution operator $\mathcal{U}(t, t_0)$

$$\mathcal{U}(t, t_0) = \exp\left[-\frac{i}{\hbar}\left(\mathcal{L}(t - t_0) - i\widehat{W}(t)\right)\right]. \tag{B.08.9}$$

Eq. (B.08.9) is an exponential function of a complex sparse matrix. The dimension of this matrix grows super-linearly with the size of the system. Therefore, solving of Eq. (B.08.9) presents one of the main difficulties of the Liouville space based methods. This equation can either be solved exactly or approximated with a truncated polynomial expansion. For a comparison of different approximations to calculate the exponential function of a matrix we recommend Ref. [22]. We will use both Liouville and Hilbert space based approaches on different example systems in Chap. C.

B.09 Quantum Stochastic Differential Equation

If the effects of the molecular environment (bath) are assumed to be random, the transition vibration ω becomes a stochastic function of time and one can prove the equivalence of the stochastic Schrödinger approach (in Hilbert space) and the generalized master equation (in Liouville space) [5, 6].

One possibility to express a stochastic process is to use so called quantum jumps [8]. After the definition of Eq. (B.08.7) we can define an effective non-hermitian Hamiltonian for a single trajectory

$$\widehat{H}_{\text{ef}} = \widehat{H} - i\Gamma, \tag{B.09.1}$$

where the Γ operator is defined as

$$\Gamma = \frac{\hbar}{2}\sum_k \gamma_k \widehat{\sigma}_k^\dagger \widehat{\sigma}_k, \tag{B.09.2}$$

the sum runs over all defined reservoir induced processes $\widehat{\sigma}_k^\dagger\widehat{\sigma}_k$, $\widehat{\sigma}_k^\dagger$ and $\widehat{\sigma}_k$ are raising and lowering operators respectively [21], as defined in the Kossakowski-Lindblad approximation (see Sec. B.08) and γ_k is the probability of the k process multiplied with the overall rate. Eq. (B.09.1) can be written as follows

$$\widehat{H}_{\text{ef}} = \widehat{H} - \frac{i\hbar}{2}\sum_k \gamma_k \widehat{\sigma}_k^\dagger\widehat{\sigma}_k \tag{B.09.3}$$

A quantum jump is defined as

$$|\psi(t+\mathrm{d}t)\rangle \longrightarrow w_k\widehat{\sigma}_k\,|\psi(t)\rangle \tag{B.09.4}$$

w_k is the probability of the $\widehat{\sigma}_k$ jump ($\sum_k w_k = 1$). We can summarize the quantum-jump procedure as follows:

(a) Calculate the jump probability

$$\mathrm{d}p = \mathrm{d}t\,\langle\psi(t)\,|\Gamma|\,\psi(t)\rangle \tag{B.09.5}$$

(b) Generate a random number between 0 and 1 ($r \in [0,1[$):

$r < \mathrm{d}p$: A quantum jump occurs.

$$|\psi(t+\mathrm{d}t)\rangle \longrightarrow \frac{w_k\widehat{\sigma}_k\,|\psi(t)\rangle}{\sqrt{\langle\psi(t)\,|\Gamma|\,\psi(t)\rangle}} \tag{B.09.6}$$

$r \geq \mathrm{d}p$: No quantum jump occurs. The system evolves under the influence of the Hamiltonian in Eq. (B.09.3)

$$|\psi(t+\mathrm{d}t)\rangle \longrightarrow \frac{1}{\sqrt{1-\mathrm{d}p}}\exp\left\{-\frac{i}{\hbar}\widehat{H}\mathrm{d}t - \Gamma\mathrm{d}t\right\}|\psi(t)\rangle \tag{B.09.7}$$

Different approaches suggested in the literature [8,23,24] use a truncated Taylor expansion instead of the exponential function in (B.09.7)

$$\exp\{\cdot\} \approx 1 - \frac{i}{\hbar}\widehat{H}\mathrm{d}t - \Gamma\mathrm{d}t \tag{B.09.8}$$

A more sophisticated approach to evaluate the exponential function [22] of the $\widehat{H}_{\text{ef}}$ operator (B.09.3) can and will be used in Chap. C.

(c) Continue the trajectory

(d) Average the observable over estimated trajectories

At a time $t + \mathrm{d}t$ we have the wave function after jump $\left|\tilde{\psi}\right\rangle$ with probability $\mathrm{d}p$ and the wave function without $\left|\breve{\psi}\right\rangle$ jump with probability $1 - \mathrm{d}p$.

$$|\psi(t+\mathrm{d}t)\rangle\langle\psi(t+\mathrm{d}t)| = \mathrm{d}p\left|\tilde{\psi}(t)\right\rangle\left\langle\tilde{\psi}(t)\right| + (1-\mathrm{d}p)\left|\breve{\psi}(t)\right\rangle\left\langle\breve{\psi}(t)\right| \tag{B.09.9}$$

If we combine those results, using the truncated Taylor expansions for simplicity, we will get

$$\mathrm{d}p\left|\tilde{\psi}(t)\right\rangle\left\langle\tilde{\psi}(t)\right| = \mathrm{d}t\sum_k \gamma_k\widehat{\sigma}_k|\psi\rangle\langle\psi|\,\widehat{\sigma}_k^\dagger \tag{B.09.10}$$

and

$$\begin{aligned}(1-\mathrm{d}p)\left|\breve{\psi}(t)\right\rangle\left\langle\breve{\psi}(t)\right| &= \left(1-\frac{i}{\hbar}\widehat{H}\mathrm{d}t-\Gamma\mathrm{d}t\right)|\psi(t)\rangle\langle\psi(t)|\left(1+\frac{i}{\hbar}\widehat{H}\mathrm{d}t-\Gamma\mathrm{d}t\right)\\ &\approx |\psi(t)\rangle\langle\psi(t)| - \frac{i}{\hbar}\mathrm{d}t\left[\widehat{H},|\psi(t)\rangle\langle\psi(t)|\right] - \left[\Gamma,|\psi(t)\rangle\langle\psi(t)|\right]_+\mathrm{d}t\end{aligned} \tag{B.09.11}$$

adding those two equations and substituting Γ accordingly to Eq. (B.09.2), substituting $|\psi(t)\rangle\langle\psi(t)|$ with $\rho(t)$ and $|\psi(t+\mathrm{d}t)\rangle\langle\psi(t+\mathrm{d}t)|$ with $\rho(t+\mathrm{d}t)$ we get

$$\rho(t+\mathrm{d}t) = \rho(t) - \frac{i}{\hbar}\mathrm{d}t\left[\left[\widehat{H},\rho(t)\right] - \sum_k\frac{\gamma_k}{2}\left(2\widehat{\sigma}_k\rho\widehat{\sigma}_k^\dagger - \left[\rho,\widehat{\sigma}_k^\dagger\widehat{\sigma}_k\right]_+\right)\right] \tag{B.09.12}$$

this is exactly the solution of the master equation in Lindblad form (B.08.7). Therefore Eq. (B.09.12) shows the equivalence of the two approaches. The full proof of the equality presented in Eq. (B.09.12) can be found in Ref. [5].

B.10 Propagation in doubled Hilbert space

One of several possible improvements to the quantum jump approach presented in the previous section is the introduction of the doubled Hilbert space method first proposed in Ref. [7]. Let us compare how the expectation value of an arbitrary operator A is computed in Liouville (B.02.2) and in Hilbert space Eq. (B.01.4). Using the definition of the trace operation in Eq. (B.02.3) and Eqs. (B.01.6),

(B.02.1) and (B.02.5), we can write for a two time correlation function

$$\begin{aligned}\langle B(t_2)A(t_1)\rangle &= \mathrm{tr}\left\{B(t_2)A(t_1)\rho(t_0)\right\} = \mathrm{tr}\left\{A(t_1)\rho(t_0)B(t_2)\right\}\\ &= \mathrm{tr}\left\{\mathcal{U}(t_2,t_0)A\mathcal{U}(t_1,t_0)\rho(t_0)B\right\}\\ &= \mathrm{tr}\left\{\mathcal{U}(t_2,t_0)A\mathcal{U}(t_1,t_0)\sum_k P_k\left|\psi_k(t_0)\right\rangle\left\langle\psi_k(t_0)\right|B\right\}\\ &= \sum_k P_k \mathrm{tr}\left\{\mathcal{U}(t_2,t_0)A\mathcal{U}(t_1,t_0)\left|\psi_k(t_0)\right\rangle\left\langle\psi_k(t_0)\right|B\right\}\\ &= \sum_k P_k \mathrm{tr}\left\{\widehat{U}(t_2,t_0)A\widehat{U}(t_1,t_0)\left|\psi_k(t_0)\right\rangle\left\langle\psi_k(t_0)\right|\widehat{U}^\dagger(t_1,t_0)\widehat{U}^\dagger(t_2,t_0)B\right\}\\ &= \sum_k P_k \left\langle\left\langle\psi_k(t_0)\right|\widehat{U}^\dagger(t_1,t_0)\widehat{U}^\dagger(t_2,t_0)B\,\middle|\,\widehat{U}(t_2,t_0)A\widehat{U}(t_1,t_0)\left|\psi_k(t_0)\right\rangle\right\rangle\end{aligned} \tag{B.10.1}$$

Eq. (B.10.1) is easily extendable to any number of operators and time variables. The third order response functions are, for example, three time four operator correlation functions. In the first step in Eq. (B.10.1) we have used the fact that the trace operation is invariant under cyclic permutations. Since trace and sum operations commute, we can write a sum operator in front of the trace operator. The last step shows us the equality between Hilbert and Liouville space approaches, in which case we have a pure state ($P_k = 1$ for one value of k and $P_k = 0$ otherwise) and can omit the sum in front of the equation. If the two time correlation function is computed as it is presented in the last step of Eq. (B.10.1), we formally have a propagation in negative time for the $\widehat{U}^\dagger$ operators. Since a quantum jump is relevant for both bra and ket at a certain time t, the propagation in negative time is not compatible with the Markov approximation.

The introduction of the doubled Hilbert space is a simple and effective method to retain the Markov approximation for the stochastic Schrödinger equation without noticeable changes in the computational effort. The new space is spanned by (ϕ, ψ). We can rewrite Eq. (B.10.1) as (assuming a pure state)

$$\begin{pmatrix}\left|\phi(t_2)\right\rangle\\ \left|\psi(t_2)\right\rangle\end{pmatrix} = \begin{pmatrix}B\widehat{U}(t_2,t_1)\widehat{U}(t_1,t_0)\left|\phi(t_0)\right\rangle\\ \widehat{U}(t_2,t_1)A\widehat{U}(t_1,t_0)\left|\psi(t_0)\right\rangle\end{pmatrix} \tag{B.10.2}$$

and in matrix form

$$\mathbf{x}(t_2) = \mathbf{B}\mathbf{U}(t_2,t_1)\mathbf{A}\mathbf{U}(t_1,t_0)\mathbf{x}(t_0), \tag{B.10.3}$$

where

$$\mathbf{x}(t) = \begin{pmatrix}\left|\phi(t)\right\rangle\\ \left|\psi(t)\right\rangle\end{pmatrix}, \tag{B.10.4}$$

$$\mathbf{U}(t_n, t_m) = \begin{pmatrix} \widehat{U}(t_n, t_m) & 0 \\ 0 & \widehat{U}(t_n, t_m) \end{pmatrix} \tag{B.10.5}$$

and

$$\mathbf{A} = \begin{pmatrix} A & 0 \\ 0 & 1 \end{pmatrix}, \quad \mathbf{B} = \begin{pmatrix} 1 & 0 \\ 0 & B \end{pmatrix} \tag{B.10.6}$$

depending on whether the operator A or B is acting from the left (on the ket) or from the right (on the bra), respectively. The expectation value is computed in complete analogy to Eq. (B.10.1) as

$$\langle \mathbf{x}(t) \rangle = \langle \psi(t) \,|\, \phi(t) \rangle \,. \tag{B.10.7}$$

The norm of $\mathbf{x}(t)$ is now

$$\|\mathbf{x}(t)\| = \|\psi(t)\| + \|\phi(t)\| = \langle \psi(t) \,|\, \psi(t) \rangle + \langle \phi(t) \,|\, \phi(t) \rangle \,. \tag{B.10.8}$$

It can be shown that for the non-hermitian operator H_{ef} the norm is a monotonically decaying function of time [9]:

$$\frac{\mathrm{d}(\|\mathbf{x}(t)\|)}{\mathrm{d}t} \leq 0. \tag{B.10.9}$$

The relaxation operators, defined in Sec. B.08, assume the following form:

$$\mathbf{\Gamma} = \begin{pmatrix} \Gamma & 0 \\ 0 & \Gamma \end{pmatrix} \tag{B.10.10}$$

Γ is defined in Eq. (B.09.2). We can also redefine the H_{ef}

$$\mathbf{H}_{\text{ef}} = \mathbf{H} - i\mathbf{\Gamma} = \begin{pmatrix} \widehat{H} & 0 \\ 0 & \widehat{H} \end{pmatrix} - i \begin{pmatrix} \Gamma & 0 \\ 0 & \Gamma \end{pmatrix} = \begin{pmatrix} \widehat{H} - i\Gamma & 0 \\ 0 & \widehat{H} - i\Gamma \end{pmatrix} \tag{B.10.11}$$

and write the double Hilbert space propagator as

$$\mathbf{U}(t_n, t_m) = \begin{pmatrix} \exp\left\{-\frac{i}{\hbar}\left(\widehat{H} - i\Gamma\right)\Delta t\right\} & 0 \\ 0 & \exp\left\{-\frac{i}{\hbar}\left(\widehat{H} - i\Gamma\right)\Delta t\right\} \end{pmatrix}, \tag{B.10.12}$$

where $t_n > t_m$ and $\Delta t = t_n - t_m$. From Eq. (B.10.2) it is obvious that ϕ and ψ are propagated simultaneously and forwards in time. Having defined a doubled Hilbert space and its operators we will proceed with the construction of a stochastic algorithm in the next section.

B.11 Monte Carlo Sampling along Feynman diagrams

Based on ideas proposed in [9], we may change and extend the basic algorithm introduced in Sec. B.09. We will explain the algorithm for the example of the two time correlation function $\langle B(t_2)A(t_1)\rangle$ presented in Eq. (B.10.1) and Eq. (B.10.3).

(a) Compute the norm of the starting vector

$$N_0 = \|\mathbf{x}(t_0)\| \tag{B.11.1}$$

(b) For $i = 1, \ldots, N$, where N is the number of time steps Δt

(i) Compute

$$\mathbf{x}(t_i) = \mathbf{U}(t_i, t_{i-1})\mathbf{x}(t_{i-1}) \tag{B.11.2}$$

(ii) And the norm of $\mathbf{x}(t_i)$

$$N_i = \|\mathbf{x}(t_i)\| \tag{B.11.3}$$

(iii) Draw a random number $r \in [0, N_0[$

if $N_i \geq r$: No quantum jump occurs. Propagate again according to Eq. (B.11.2).

if $N_i < r$: A quantum jump occurs. Compute

$$\widetilde{\mathbf{x}} = \mathbf{\Gamma} \cdot \mathbf{x}(t_i) \tag{B.11.4}$$

Since the quantum jump changes the norm, we have to recompute $N_0 = \|\widetilde{\mathbf{x}}\|$ and return to the propagation loop in Eq. (B.11.2) with $\mathbf{x}(t_{i-1}) = \widetilde{\mathbf{x}}$.

(iv) When i reaches N we apply the next operator (A in our case) and continue from Eq. (B.11.1). When i reaches the next value of N we apply the next operator (B) and so on.

(c) When all time variables reached their desired values, represented by the iteration counter i, we compute the expectation value of the correlation function according to Eq. (B.10.7).

This algorithm allows us to compute correlation functions in time domain as arrays of numbers. Every number of such array represents an expectation value $\langle S(t_i, t_j, \ldots)\rangle$ in the time domain. A comparison between the functions in time and frequency domains and some theory of Fourier transformation is explained on some illustrative examples in Sec. C.02.

Another practical aspect of the presented algorithm is the normalization. This approach is mathematically and numerically equivalent to normalization after every operator step and selecting random numbers $r \in [0, 1[$. The advantage in using non-normalized functions lies in the possibility of a direct comparison to the exact Liouville space propagation, starting from the same populated states (for example a Boltzmann distribution at room temperature).

This algorithm is used to compute the signal of different optical measurements in a perturbative bottom-up way. In this work we consider only first and third-order polarization as the most common experiments, however the method is not limited to these and can be easily expanded to any type of optical signal. We assume delta pulses and construct different signals (represented by double-sided Feynman diagrams) as described in Sec. B.05 and Sec. B.06. The response functions are calculated N times using the quantum jump approach described above. The mean response functions are estimated and used as an approximation to the Liouville space approach. The numerical results are presented in Chap. D.

On the other hand, there are approaches to compute the optical polarization non-perturbatively. The polarization then contains the sum of all different signals, in which it has to be decomposed according to the experimental requirements [10–12]. This decomposition is one of the main problems for the stochastic treatment and diverges easily [25].

Another advantage of the perturbative bottom-up approach is in its native parallelizability. Every single response function, which is responsible for some part of the observed signal, can be sampled independently from all other response functions. Since the samples are also independent, the computations can be massively parallelized.

Chapter C

From theory to numbers

After a brief introduction of the theory behind the multidimensional vibrational spectroscopy in Chap. B, we want to give some illustrative examples to describe the most important spectral features. In this chapter we will use the spectral nomenclature introduced by Hamm* in Ref. [1] to simplify the comparison of the computed spectra with the literature.

The code used in this chapter was written from scratch as a part of the THCTK package suite [26] using a combination of the Python, C and FORTRAN programming languages.

C.01 Single harmonic oscillator

First, we will compute linear absorption spectra represented by the $J(t_1)$ term in Eq. (B.06.1), which we can split into two different Feynman diagrams (see Fig. C.1 and compare to Fig. B.1). As a simple benchmark we choose one harmonic oscillator with frequency $\omega_{01} = 250$ cm^{-1} (or 7.49×10^{12} Hz). We also assume weak pulses and therefore allow only one level transitions ($0 \leftrightarrow 1$, $1 \leftrightarrow 2$, and so on). The system is initially in its ground state at t_0

$$\rho(t_0) = \begin{pmatrix} 1 & 0 \\ 0 & 0 \end{pmatrix}. \tag{C.01.1}$$

Under these restrictions all but the ground and the first excited states of the harmonic oscillator can be omitted. The Hamiltonian matrix sufficient for the linear absorption spectrum will become

$$\widehat{H} = \begin{pmatrix} 0 & 0 \\ 0 & \omega_{01} \end{pmatrix}, \tag{C.01.2}$$

*The third time domain along the abscissa and the first time domain along the ordinate.

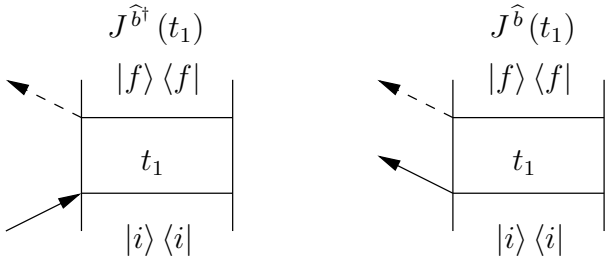

Figure C.1: Double-sided Feynman diagrams for a first order linear response function from Eq. (B.06.1) divided into terms due to the interaction with raising ($\widehat{b}^\dagger$ – left diagram) and lowering ($\widehat{b}$ – right diagram) operators as components of the dipole operator $\widehat{\mu}$. $|i\rangle\langle i|$ is the initial and $|f\rangle\langle f|$ is the final state.

while the transition dipole matrix is defined (for simplicity reasons) as

$$\widehat{\mu} = \begin{pmatrix} 0 & 1 \\ 1 & 0 \end{pmatrix} = \begin{pmatrix} 0 & 1 \\ 0 & 0 \end{pmatrix} + \begin{pmatrix} 0 & 0 \\ 1 & 0 \end{pmatrix} = \widehat{b} + \widehat{b}^\dagger \tag{C.01.3}$$

From the two upper diagrams in Fig. B.1 remains only the left one (the right one is its complex conjugate). This diagram can be further divided into two diagrams (see Fig. C.1). These Feynman paths do not necessarily have any physical meaning, but their sum does. Generally, though, the calculation of the response function can be greatly simplified, due to the fact that some of the terms can be neglected.

Since our system is in the ground state $|i\rangle\langle i| = |0\rangle\langle 0|$ (see Eq. (C.01.1)), the interaction of the system with lowering operators ($\widehat{b}$ from left and $\widehat{b}^\dagger$ from right) will not contribute to the response function. This approximation is called the Low Temperature Approximation (LTA). In case the system is not in the ground state at t_0 ($i \neq 0$ in Fig. C.1) the $J^{\hat{b}}(t_1)$ response function can be neglected because of the Rotating Wave Approximation (RWA) [16, 27]. Having only one remaining Feynman path $J^{\hat{b}^\dagger}(t_1)$ that describes the linear response function, omitting the $\widehat{b}^\dagger$ superscript and discretizing the time variable[†] ($\tau_i = \tau_{i-1} + \Delta\tau$, with $i = 1 \ldots, N$, time step $\Delta\tau$ and $\tau_0 = t_0$), we can compute it as

$$\begin{aligned} \rho'(\tau_0) &= \widehat{b}^\dagger \rho(\tau_0) \\ \rho'(\tau_i) &= \mathrm{e}^{-i\widehat{H}\Delta\tau} \rho'(\tau_{i-1}) \mathrm{e}^{i\widehat{H}\Delta\tau} \\ J(\tau_i) &= \left\langle \widehat{b}\, \rho'(\tau_i) \right\rangle, \; i = 1 \ldots, N \end{aligned} \tag{C.01.4}$$

$J(\tau_i)$ is an array of points with length N. To compute every single point of this

[†]We denote the discretized time with τ and the absolute time with t. The time points t_i and τ_i are equivalent.

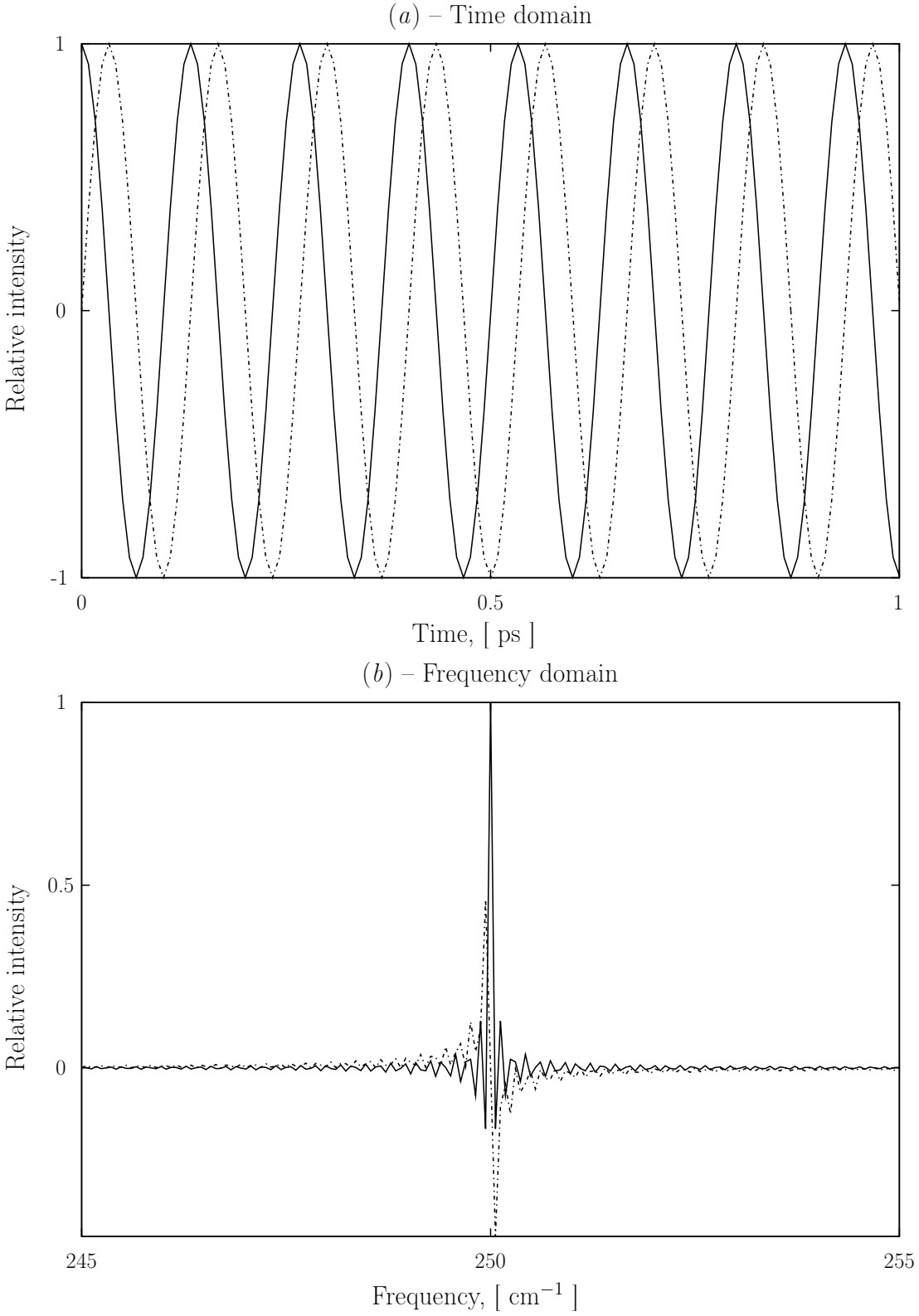

Figure C.2: First-order response function for a single harmonic oscillator with a frequency of 250 cm^{-1} computed in time domain (a) and transformed to frequency domain (b). The real part of the response function is plotted with solid lines, while the imaginary part is plotted with dotted lines.

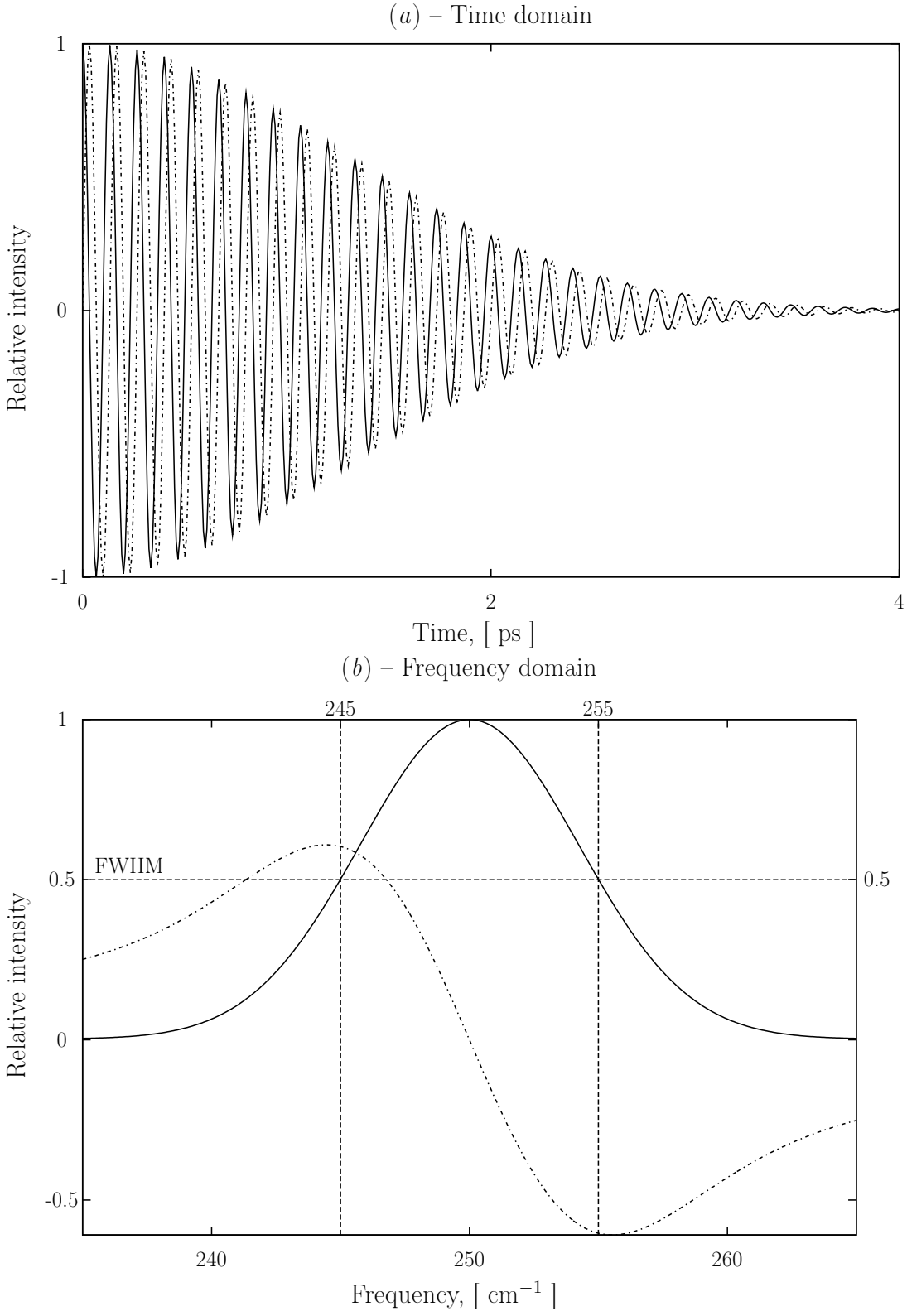

Figure C.3: First-order response function for a damped harmonic oscillator with a frequency of 250 cm^{-1} and FWHM of 10 cm^{-1} computed in time domain (a) and transformed to frequency domain (b). The real part of the response function is plotted with solid lines, while the imaginary part is plotted with dotted lines.

array one has to perform four matrix-matrix products and a trace operation. Since the matrix-vector products are much more convenient to work with than matrix-matrix products, especially while working with sparse matrices, we will work with the vectorized form of the Eq. (C.01.4). The rules how to use the vectorization operator $\mathrm{vec}\,(\cdot)$ can be found in Ref [15]. Eq. (C.01.4) then takes following form

$$J(\tau_i) = \mathrm{tr}\left\{ (\mathbf{I}\otimes\widehat{b}\,)\underbrace{\exp\left\{-i(\mathbf{I}\otimes\widehat{H}-\widehat{H}\otimes\mathbf{I})\Delta\tau\right\}}_{\mathcal{G}(\Delta\tau)}(\mathbf{I}\otimes\widehat{b}^{\dagger}\,)\mathrm{vec}\,(\rho(\tau_{i-1}))\right\} \tag{C.01.5}$$

It is more convenient to work with time steps $\Delta\tau$ instead of absolute times t (to compute the next step we only need the previous one and not the density matrix or wavefunction at time τ_0). The computing algorithm has a following form

$$\begin{aligned}
\mathrm{vec}\,(\rho'(\tau_0)) &= (\mathbf{I}\otimes\widehat{b}^{\dagger}\,)\mathrm{vec}\,(\rho(\tau_0)) \\
\mathrm{vec}\,(\rho'(\tau_i)) &= \exp\left\{-i(\mathbf{I}\otimes\widehat{H}-\widehat{H}\otimes\mathbf{I})\Delta\tau\right\}\mathrm{vec}\,(\rho'(\tau_{i-1})) \\
J(\tau_i) &= \mathrm{tr}\left\{(\mathbf{I}\otimes\widehat{b}\,)\mathrm{vec}\,(\rho'(\tau_i))\right\},\ i=1\ldots,N
\end{aligned} \tag{C.01.6}$$

The steps two and three of Eq. (C.01.6) are performed repeatedly, until the last point $J(\tau_N)$ is computed. The time resolution ($\Delta\tau$) and the total propagation time ($N\Delta\tau$) are parameters, which can be set depending on our requirements. In the frequency domain (see Sec. C.02) those parameters are connected to the maximal frequency via

$$\omega_{\max} = \frac{2\pi}{2\Delta\tau} \tag{C.01.7}$$

and the frequency resolution via

$$\Delta\omega = \frac{2\pi}{N\Delta\tau}. \tag{C.01.8}$$

$\omega_{\max}$ from the Eq. (C.01.7) is known as the Nyquist critical frequency described in Sec. C.02 and it is a consequence of the Nyquist-Shannon theorem on page 39. Setting $\omega_{\max}$ to 2000 cm^{-1} and $\Delta\omega$ to 0.1 cm^{-1} (which is equal to $\Delta\tau \approx 8.34$ fs and $N = 40000$) we compute the first order linear response function in the time domain. The Fourier transformation of this function (see Sec. C.02) gives us a first order response function in frequency domain (see Fig. C.2).

The linear response function of a harmonic oscillator is a benchmark case with well known result and therefore can be used for understanding, code checking and debugging purposes. The Liouville and Hilbert space computations yield the same result (since we have a pure state without any dissipation). We get one single

peak at 250 cm^{-1} (Fig. C.2-(b)) or less than 7.5 oscillations in one picosecond (Fig. C.2-(a)). In the frequency domain the peak appears as a $\mathrm{sinc}(x) = \frac{\sin(x)}{x}$ function. The reason for that is the rectangular shape of the time time domain function ($f(t)$). See Ref. [28] for details.

$$f(t) = \begin{cases} J(t), & t \in [\tau_0, \tau_N] \\ 0, & t < \tau_0 \cup t > \tau_N \end{cases} \tag{C.01.9}$$

The easiest way to simulate a dissipation processes is to assume a Gaussian-type population decay, which results in the convolution of the time-dependent signal with

$$\exp\left\{-\frac{\tau_i^2}{2\sigma^2}\right\} \tag{C.01.10}$$

The full width at half maximum (FWHM) of the resulting Gaussian function is given by

$$\mathrm{FWHM} = 2\sqrt{2\ln(2)}\sigma \tag{C.01.11}$$

or the other way around, if we want to get a peak with an artificial but defined value of FWHM we can also get a σ value from Eq. (C.01.11). In Fig. C.3 we computed the spectra from Fig. C.2 but with the FWHM set to 10 cm^{-1}.

C.02 Fourier transformation

So far response functions in time and in frequency domains were calculated. Since the relationship between both is very important for different kinds of spectroscopy, we will give a short description of the Fourier transformation in this section. For more detailed descriptions Ref. [1, 28] are recommended.

The Fourier transformation of a time domain function is defined as

$$f(\omega) = FT(f(t)) = \frac{1}{\sqrt{2\pi}} \int_{-\infty}^{\infty} f(t) \mathrm{e}^{i\omega t} \mathrm{d}t \tag{C.02.1}$$

its inverse operation is a transformation of a frequency domain function

$$f(t) = FT^{-1}(f(\omega)) = \frac{1}{\sqrt{2\pi}} \int_{-\infty}^{\infty} f(\omega) \mathrm{e}^{-i\omega t} \mathrm{d}\omega. \tag{C.02.2}$$

The condition is also known as the Fourier inversion theorem and it holds if both $f(t)$ and its Fourier transform are absolutely integrable (in the Lebesgue sense [29]) and $f(t)$ is continuous at the point t ($f(t) = FT^{-1}(FT(f(t)))$).

The 2D Fourier transformation is defined as

$$f(\omega_2, \omega_1) \propto \int_{-\infty}^{\infty} \int_{-\infty}^{\infty} f(t_2, t_1) \mathrm{e}^{i\omega_2 t_2} \mathrm{e}^{i\omega_1 t_1} \mathrm{d}t_2 \mathrm{d}t_1 \tag{C.02.3}$$

and

$$f(t_2,t_1) \propto \int_{-\infty}^{\infty}\int_{-\infty}^{\infty} f(\omega_2,\omega_1)\mathrm{e}^{-i\omega_2 t_2}\mathrm{e}^{-i\omega_1 t_1}\mathrm{d}\omega_2\mathrm{d}\omega_1. \tag{C.02.4}$$

Since the response functions are discretized, instead of using equations (C.02.1-C.02.4), one has to use the discrete Fourier transformation. The equations (C.02.1) and (C.02.2) will then become

$$f(\omega_n) = \frac{\Delta t}{\sqrt{2\pi}}\sum_{k=0}^{N-1} f(t_k)\mathrm{e}^{2\pi i\frac{kn}{N}} \tag{C.02.5}$$

and

$$f(t_k) = \frac{\Delta \omega}{\sqrt{2\pi}}\sum_{n=0}^{N-1} f(\omega_n)\mathrm{e}^{-2\pi i\frac{kn}{N}} \tag{C.02.6}$$

respectively. N is both the number of time steps and the length of the transformed array. Δt is the time step. The larger N and Δt are, the smaller $\Delta\omega$ (see Eq. (C.01.8)) and the higher the frequency resolution of the spectrum will be.

Eq. (C.01.7) is the result of the Nyquist–Shannon sampling theorem: *If a function $f(t)$ contains no frequencies higher than $\nu_{\max}$–Hertz, it is completely determined by giving its ordinates at a series of points spaced $\frac{1}{2\nu_{\max}}$ seconds apart.*

The consequence of the Nyquist–Shannon sampling theorem is the Nyquist critical frequency (Eq. (C.01.7)). All frequencies above $\omega_{\max}$ are folded back into the frequency window defined by the $\omega_{\max}$. This effect is called aliasing.

C.03 Third order response functions

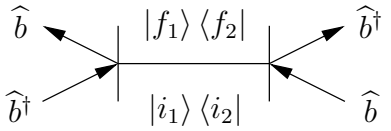

Figure C.4: Possible field interactions that lead to transition from the initial state $|i_1\rangle\langle i_2|$ to the final state $|f_1\rangle\langle f_2|$. Transition dipole $\widehat{\mu}$ is presented (see Eq. (C.01.3)) in terms of rising $\widehat{b}^\dagger$ and lowering $\widehat{b}$ operators.

Let us consider the third order nonlinear response function from Eq. (B.06.3) and $R_I,\ldots,R_{IV}$ from Fig. B.1. If we now divide the interactions with the radiation field as it was done in Eq. (C.01.3), we get four possible interactions (Fig. C.4). Since in the third order nonlinear response function we have three subsequent light interactions, we get 64 (4^3) possibilities, which can be represented in terms of Feynman diagrams. We can neglect all terms with $\widehat{b}$ being the first interaction

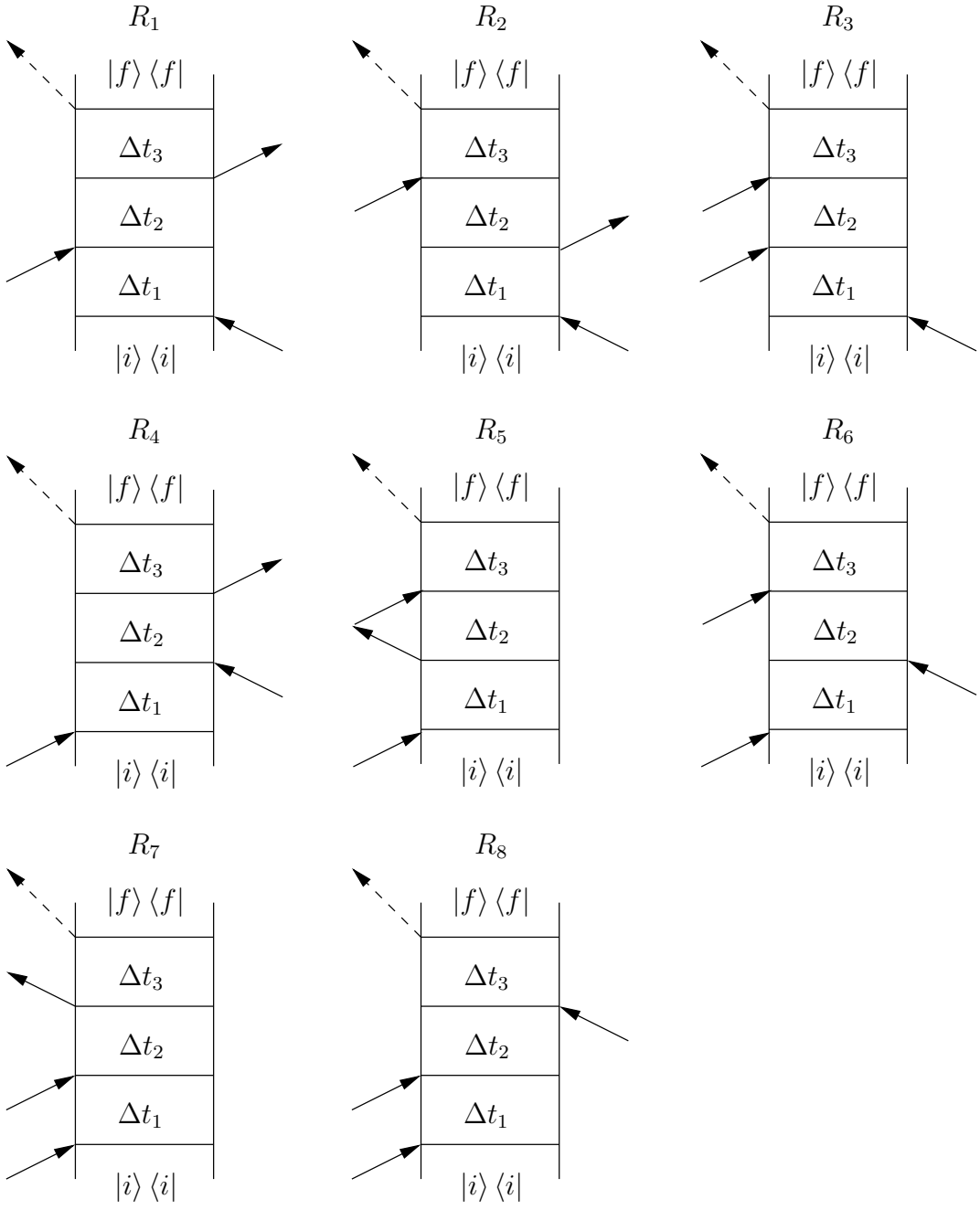

Figure C.5: Third order nonlinear response function terms (Eqs. (B.06.3) and (C.01.3)) that survive LTA and RWA (Sec. C.01). The numbering of the terms was chosen to match the nomenclature used in [1].

from the left and $\widehat{b}^{\dagger}$ – from the right applying the LTA (see Sec. C.01). This reduce the number of terms to 16. Using RWA (see Sec. C.01) we further reduce the number of terms to 8. The Feynman diagrams representing those terms are displayed in Fig. C.5.

The terms R_1, R_2, R_3 are emitted in the $-\vec{k}_1 + \vec{k}_2 + \vec{k}_3$ direction and can be separated from R_4, R_5, R_6 $(\vec{k}_1 - \vec{k}_2 + \vec{k}_3)$ and from R_7, R_8 $(\vec{k}_1 + \vec{k}_2 - \vec{k}_3)$ by phase matching. The most general form of a 2D IR experiment is called box-CARS[‡]. The generated signal field has the wave vector $\mp k_1 \pm k_2 + k_3$. The R_7 and R_8 diagrams represent a different experiment and are called two-quantum pulse sequences [1]. Our methods are not restricted by the experimental setup and we can simulate any pulse sequence. Since we will focus on method development and its comparison to the experiment, we will consider only rephasing and non-rephasing diagrams, which are discussed in detail in the following section.

C.04 Rephasing and non-rephasing spectra

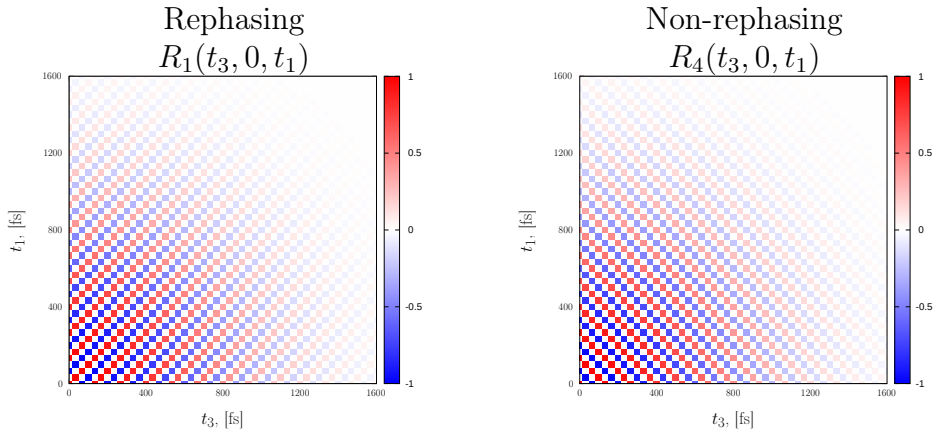

Figure C.6: The real parts of R_1 and R_4 are shown in time domain. Every point of the spectra represents a value of the normalized response function. The damping in both time dimensions was introduced phenomenologically in analogy to Fig. C.3 (see text for details). The value of t_2 is set to zero.

The contributions R_1, R_2, R_3 are the so-called rephasing diagrams, because the individual Bloch vectors rephase at $t_1 = t_3$, which leads to reappearance of a macroscopic polarization as photon echo (see Ref. [1] for details). The R_4, R_5, R_6 are non-rephasing response functions.

The rephasing terms can be separated from non-rephasing by phase matching. The diagrams R_1, R_2 and R_4, R_5 can be explained for the example of a single

[‡]Coherent Anti-Stokes Raman Spectroscopy (CARS) [1, 4]

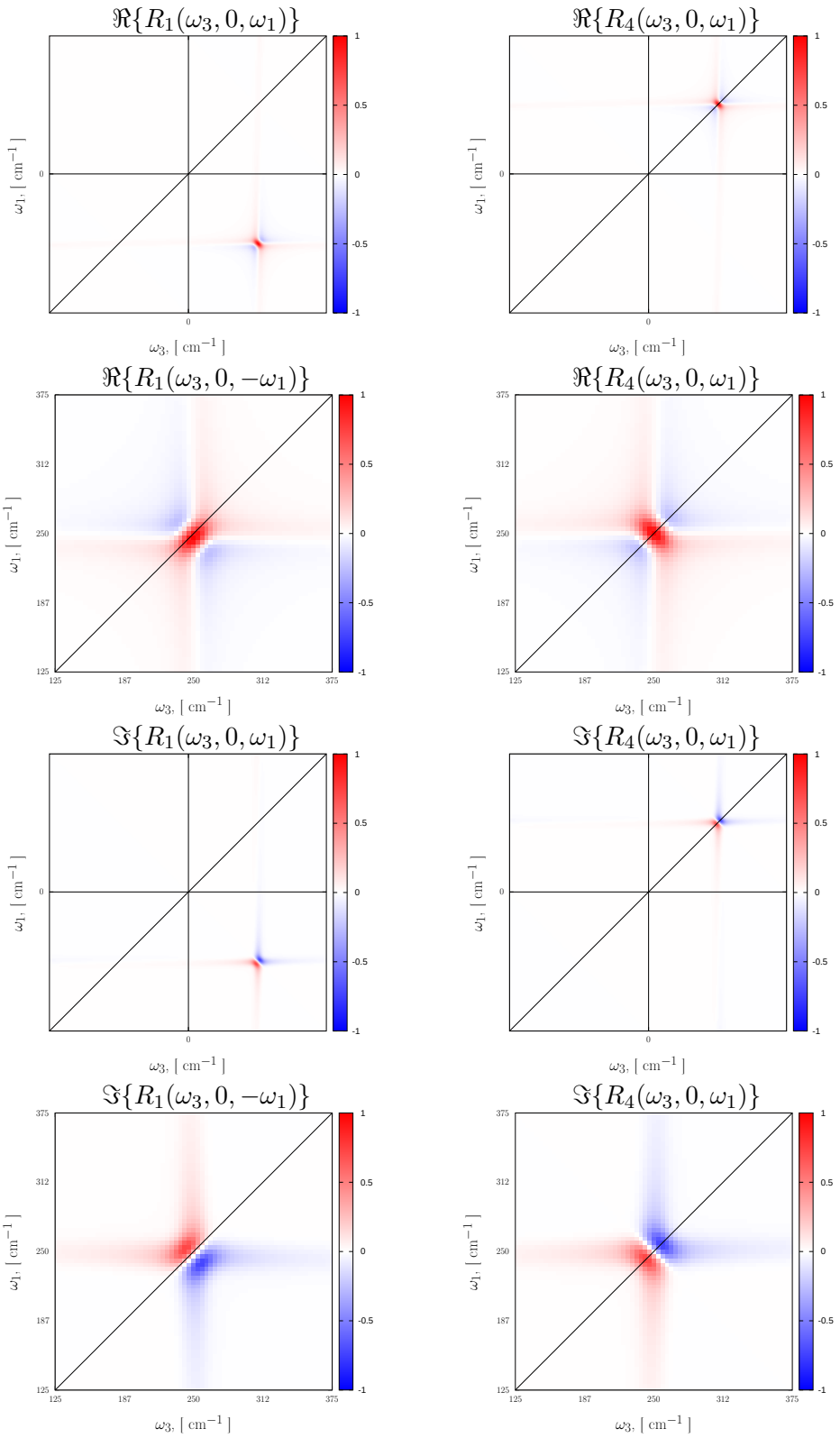

Figure C.7: The rephasing (R_1) and non-rephasing (R_4) response functions in frequency domain. The value of t_2 is set to zero, FWHM=20 cm^{-1}.

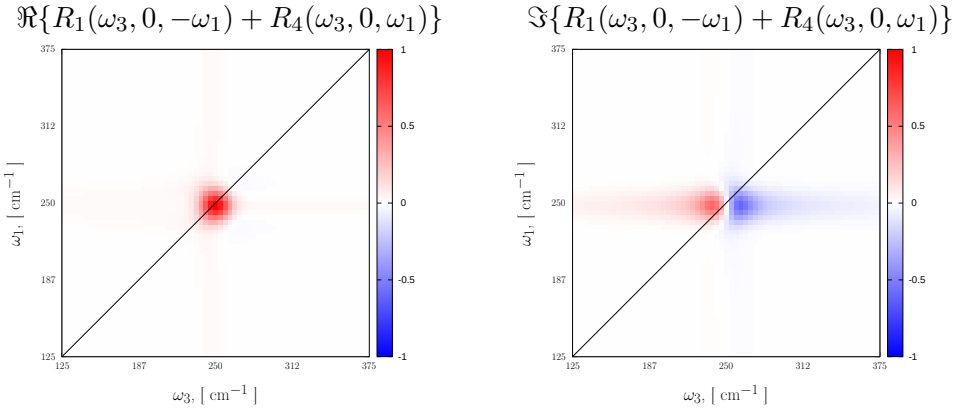

Figure C.8: The absorptive ($\Re\{R_1(\omega_3,0,-\omega_1)+R_4(\omega_3,0,\omega_1)\}$) and dispersive ($\Im\{R_1(\omega_3,0,-\omega_1)+R_4(\omega_3,0,\omega_1)\}$) signals are calculated as sums of real and imaginary parts of the rephasing and non-rephasing signals, respectively. The value of t_2 is set to zero, FWHM=20 cm^{-1}.

harmonic oscillator and are suited well to describe both the rephasing and the non-rephasing effects on the spectrum. The anharmonic effects will be described in Sec. C.05 for example of the R_3 and R_6 terms.

In the case of a single oscillator with population time t_2 set to 0 fs and without relaxation the terms $R_1 = R_2$ and $R_4 = R_5$ are pairwise equal. Therefore we will consider only R_1 and R_4 in this section.

For now, we will omit the discussion of the relaxation effects and consider only the oscillating part of the response functions.

$$\begin{aligned} R_1(t_3,0,t_1) &\propto \mathrm{e}^{-i\omega t_3}\mathrm{e}^{+i\omega t_1} \\ R_4(t_3,0,t_1) &\propto \mathrm{e}^{-i\omega t_3}\mathrm{e}^{-i\omega t_1} \end{aligned} \tag{C.04.1}$$

The difference between both terms in Eq. (C.04.1) results in the different oscillation pattern (see Fig. C.6). As in Sec. C.01 and in analogy with Fig. C.3 we introduce a phenomenological Gaussian-broadening with FWHM=20 cm^{-1} to improve the appearance of the 2D spectra and postpone the introduction of the homogeneous and inhomogeneous broadening to the later sections.

The real and imaginary parts of the response function in the frequency domain are represented in Fig. C.7. The signal from the non-rephasing diagram (R_4) appears in the first quadrant of the spectrum, whereas the rephasing diagram yields a peak in the forth quadrant. If we invert the ω_1-axis of the rephasing signal, we will map it into the first quadrant (lower four spectra of the Fig. C.7). The sum of the real parts of rephasing and non-rephasing diagrams ($\Re\{R_1(\omega_3,0,-\omega_1)\}+\Re\{R_1(\omega_3,0,\omega_1)\}$) gives us very sharp absorptive signal and the sum of the imaginary parts ($\Im\{R_1(\omega_3,0,-\omega_1)\}+\Im\{R_1(\omega_3,0,\omega_1)\}$) gives us a dispersive signal (see

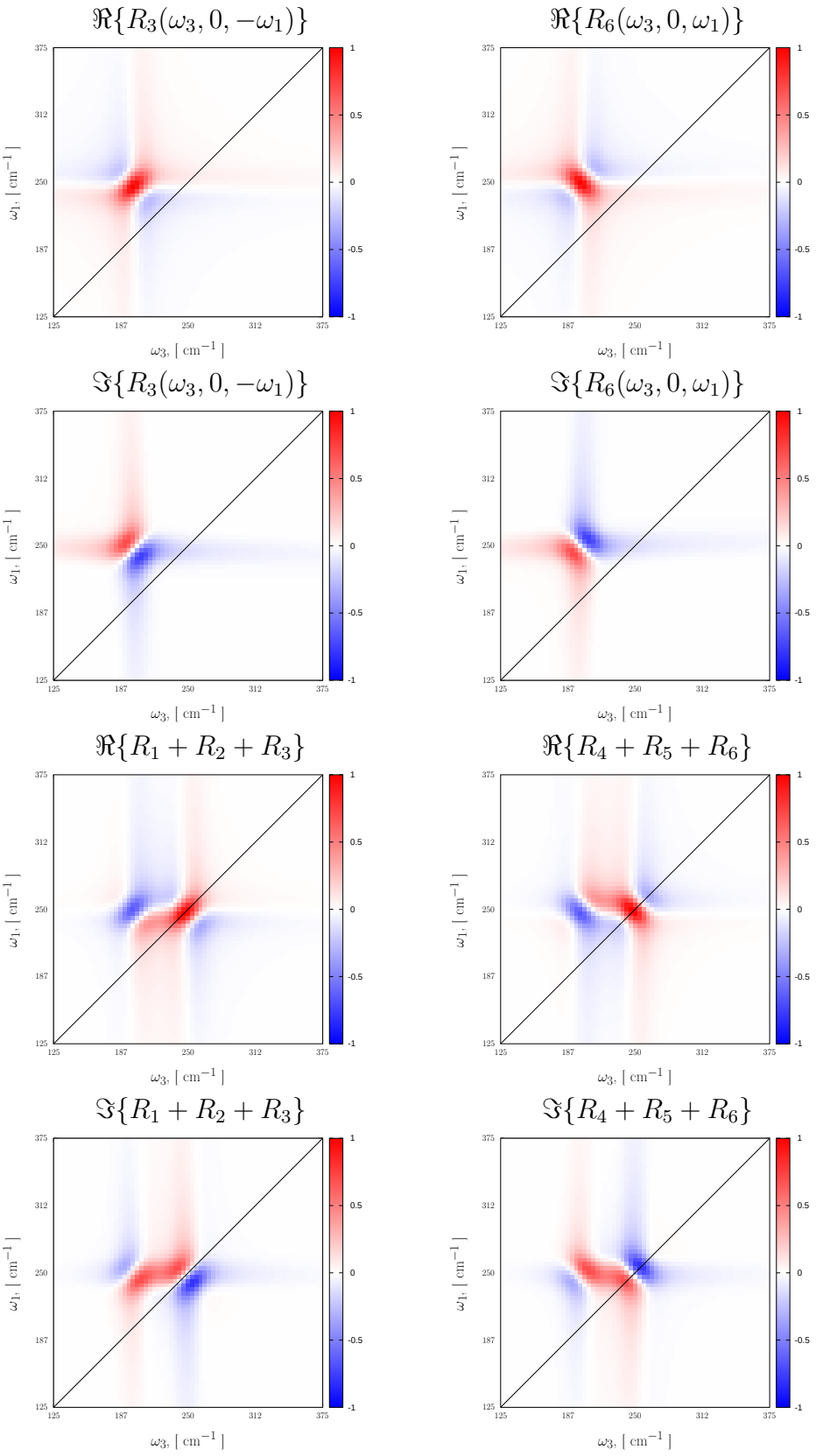

Figure C.9: The anharmonicity effects in 2D spectra shown for the example of the rephasing (R_3) and non-rephasing (R_6) response functions (upper four spectra) and sums of rephasing and non-rephasing terms (lower four spectra) in frequency domain. The value of t_2 is set to zero, FWHM=20 cm^{-1}.

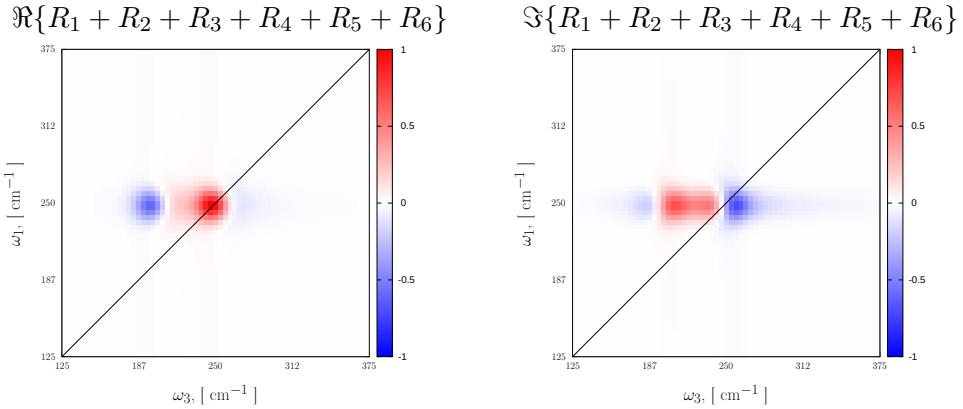

Figure C.10: Absorptive ($\Re\{R_1+R_2+R_3+R_4+R_5+R_6\}$) and dispersive ($\Im\{R_1+R_2+R_3+R_4+R_5+R_6\}$) spectra of a single anharmonic oscillator. The distance between the maximum and the minimum in the absorptive spectrum is 50 cm^{-1}. The value of t_2 is set to zero, FWHM=20 cm^{-1}.

Fig. C.8 and Ref. [1]). Though the separation in the pure absorptive and dispersive signals is desirable, more common in 2D spectroscopy are the mixed signals, which result from the superposition of real and imaginary parts of the response function. The peak shape that corresponds to mixed signal is referred to as *phase-twist* [30].

C.05 Anharmonic oscillator

To consider the signal from the diagrams R_3 and R_6 we need more than one excited level and a non-vanishing transition dipole moment between the first and the second excited levels. We set the anharmonicity $(\omega(0\rightarrow 1)-\omega(1\rightarrow 2))$ to $\Delta\omega = 50$ cm^{-1} to avoid the peak-overlap and make the spectral feature well recognizable. The Hamiltonian matrix becomes

$$\widehat{H} = \begin{pmatrix} 0 & 0 & 0 \\ 0 & \omega_{01} & 0 \\ 0 & 0 & \omega_{02} \end{pmatrix}, \tag{C.05.1}$$

with $\omega_{01} = 250$ cm^{-1}, $\omega_{02} = 450$ cm^{-1} and $\Delta\omega = 2\omega_{01} - \omega_{02} = 50$ cm^{-1}. Using the harmonic approximation for climbing up the vibrational ladder, the dipole matrix for the three lowest states becomes [1]

$$\widehat{\mu} = \begin{pmatrix} 0 & 1 & 0 \\ 1 & 0 & \sqrt{2} \\ 0 & \sqrt{2} & 0 \end{pmatrix} = \underbrace{\begin{pmatrix} 0 & 1 & 0 \\ 0 & 0 & \sqrt{2} \\ 0 & 0 & 0 \end{pmatrix}}_{\widehat{b}} + \underbrace{\begin{pmatrix} 0 & 0 & 0 \\ 1 & 0 & 0 \\ 0 & \sqrt{2} & 0 \end{pmatrix}}_{\widehat{b}^\dagger}. \tag{C.05.2}$$

With equations (C.05.1) and (C.05.2) we can compute the third order response functions for the terms R_3 (two left upper spectra in Fig. C.9) and R_6 (two right upper spectra in Fig. C.9). After that we compute sums of the rephasing signals and non-rephasing signals (two lower left and right spectra in Fig. C.9 respectively). In Fig. C.10 we compute the sum of real and imaginary parts of all six terms of the response function. The upper spectrum in Fig. C.10 is the absorptive spectrum of one anharmonic oscillator with $\omega = 250$ cm^{-1}, an anharmonicity of $\Delta\omega = 50$ cm^{-1}, and FWHM = 20 cm^{-1}.

C.06 Three oscillators

Before considering dissipation problems and computing real system Hamiltonians and transition dipole operators we want to examine yet another benchmark consisting of three (an)harmonic oscillators. The resulting case is more complex than it may seem to be at first glance. At first we define three harmonic oscillators with frequencies $\omega_{01}^a = 2880$ cm^{-1}, $\omega_{01}^b = 2950$ cm^{-1} and $\omega_{01}^c = 3220$ cm^{-1}. With the weak pulse approximation only first and second excited states need to be considered. Taking into account all possible excitation combinations (3^3) we will get a 27 dimensional Hamiltonian matrix. For example, one of the possible excited configurations is $(1, 0, 2)$ and it denotes a combination of the first excited level of the first harmonic oscillator, the ground state of the second, and the second excited level of the third vibrational mode. We have chosen frequencies of two CH and one NH stretching modes because they are usually well separated from other vibrational modes and therefore easier to separate from other frequencies in a measured spectrum (see Chap. E).

The transition dipole operator for the three oscillators in the same basis has the form

$$\widehat{\mu}^{3\mathrm{O}} = \mathbf{1} \otimes \mathbf{1} \otimes \widehat{\mu} + \mathbf{1} \otimes \widehat{\mu} \otimes \mathbf{1} + \widehat{\mu} \otimes \mathbf{1} \otimes \mathbf{1}, \tag{C.06.1}$$

where $\widehat{\mu}$ is the transition dipole operator of a single oscillator as defined in Eq. (C.05.2), $\mathbf{1}$ is a unity matrix with dimensions equal to the number of single oscillator levels. For simplicity reasons we used the same transition dipole moments for all three oscillators. If needed, those values can always be adjusted.

In Fig. C.11 we show the real parts of the first six response functions from Fig. C.5 (the same response functions were calculated for one anharmonic oscillator in Sec. C.04 and Sec. C.05). The lowest two spectra in Fig. C.11 are again the sums of the real and imaginary parts of the six response functions, respectively. The quite complex appearance of the third order response functions for three harmonic oscillators adds up to three sharp absorptive peaks at the respective harmonic frequencies.

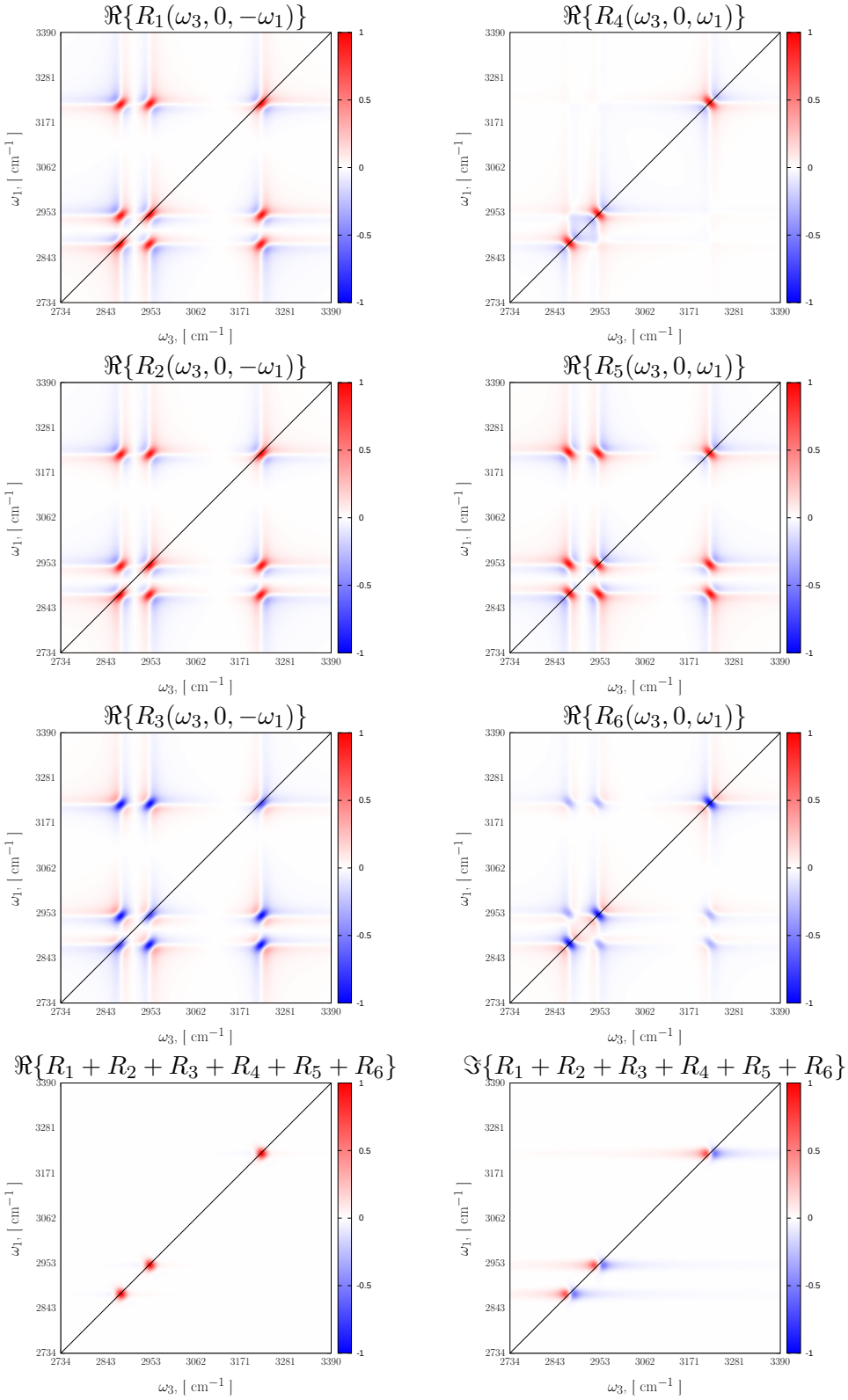

Figure C.11: The real parts of third order response functions of three harmonic oscillators (see Sec. C.06), their sum and the sum of imaginary parts of these response functions. The value of t_2 is set to zero, FWHM is set to 20 cm^{-1}.

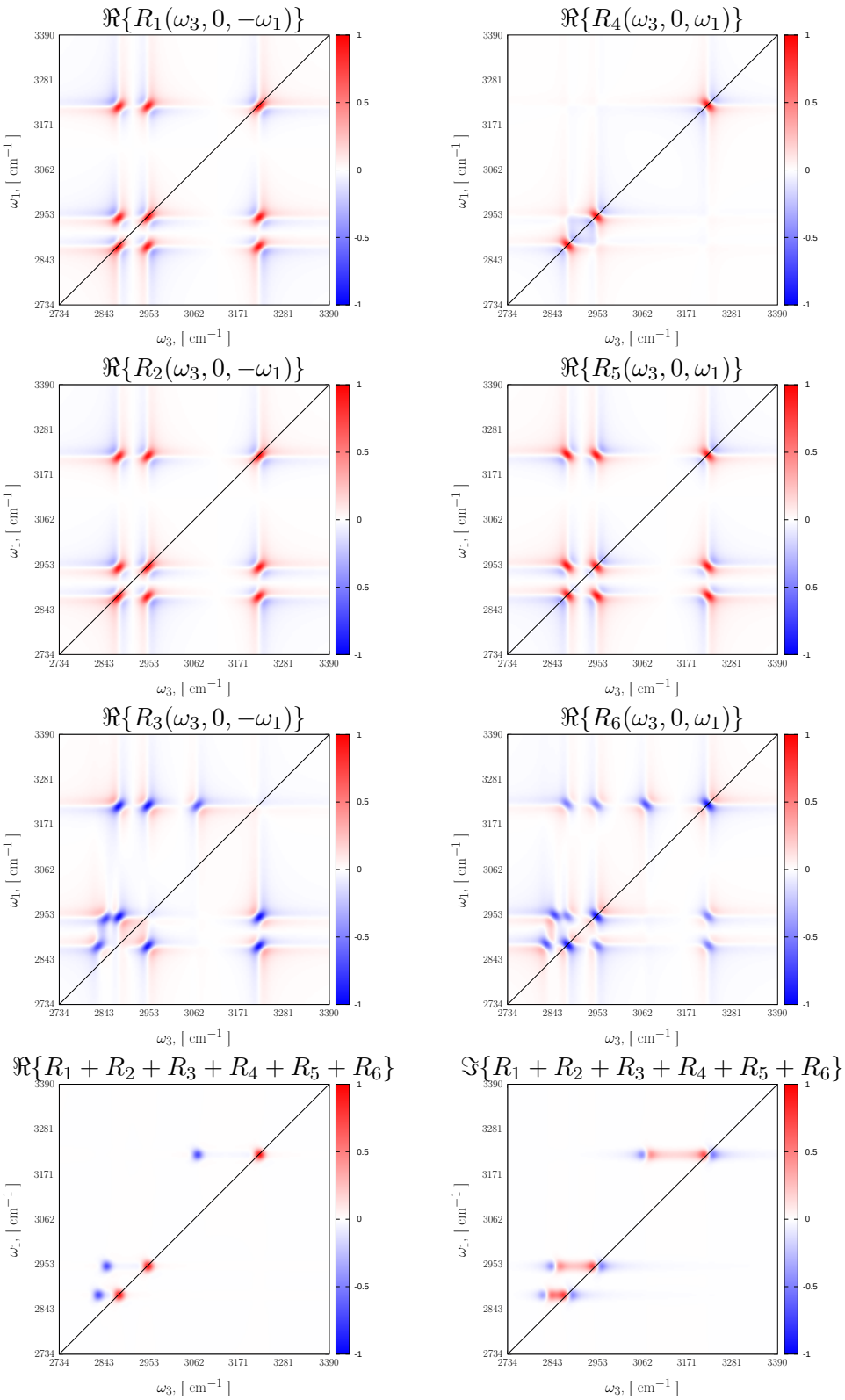

Figure C.12: The real parts of third order response functions of three anharmonic oscillators (see Sec. C.06), their sum and the sum of imaginary parts of these response functions. The value of t_2 is set to zero, FWHM=20 cm^{-1}.

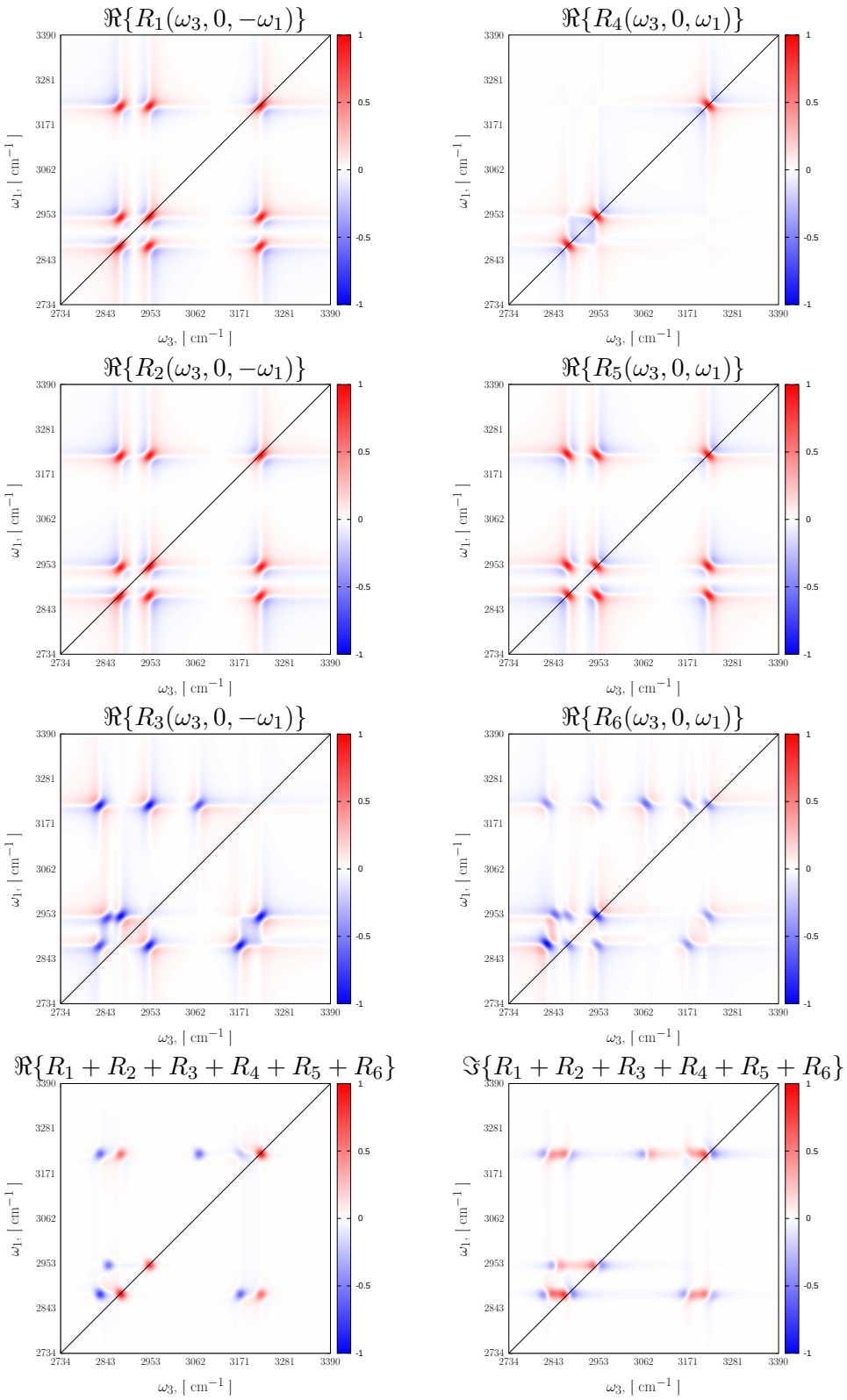

Figure C.13: The real parts of third order response functions of three anharmonic oscillators with additional coupling between $(1,0,0)$ and $(0,0,1)$ states (see Sec. C.06), their sum and the sum of imaginary parts of these response functions. The value of t_2 is set to zero, FWHM is set to 20 cm^{-1}.

In a next step we add the anharmonic effects to the previously defined oscillators, setting $\Delta\omega^a = 2\omega^a_{01} - \omega^a_{02} = 50$ cm^{-1}, $\Delta\omega^b = 2\omega^b_{01} - \omega^b_{02} = 100$ cm^{-1} and $\Delta\omega^c = 2\omega^c_{01} - \omega^c_{02} = 150$ cm^{-1}, thus changing the energies of all states that include a second excitation in any of the vibrational modes. The dipole operator and the dimensionality of the problem remain unchanged. The influence of the anharmonicity on the response functions and the sum spectra can be seen from Fig. C.12. As it was shown in Sec. C.05, only the terms R_3 and R_6 are influenced by the introduction of anharmonicities. In the sum spectra in Sec. C.05 new negative peaks appear to the left from the positive diagonal peaks. The horizontal distance between the positive and the negative peak is equal to the anharmonicity $\Delta\omega^i$ $(i = a, b, c)$ of the oscillator.

Let us now assume, that the energy of the state $(1, 0, 1)$ is $\epsilon^{(1,0,1)} = \epsilon^{(1,0,0)} + \epsilon^{(0,0,1)} - \delta^{(1,0,1)}$. If the energy of the state $(1, 0, 1)$ is not equal to the sum of the energies of states $(1, 0, 0)$ and $(0, 0, 1)$ ($\delta^{(1,0,1)} \neq 0$), we will observe cross peaks between $(1, 0, 0)$ and $(0, 0, 1)$ vibrational modes. We have not changed the structure of the Hamiltonian and dipole matrices. For the value of $\delta^{(1,0,1)} = 50$ cm^{-1} the 2D spectra are presented in Fig. C.13. As before we show the real parts of the third order signals and the sums of their real and imaginary parts in Fig. C.13. As in the case of the anharmonicity effects the coupling between the oscillators influences only the R_3 and R_6 response functions. The changes in those response functions result in the appearance of two new cross peaks between the first and the third normal modes, which is consistent with the literature [1].

We have changed the energy of a combined state without introducing any non-diagonal elements into the Hamiltonian matrix and therefore the system is in the eigenbasis at the beginning (τ_0). However if the Hamiltonian matrix is non-diagonal, which is usually the case, computation of its exponential function is not trivial anymore. One has to either diagonalize the matrix and transform the density matrix and dipole operators into the eigenbasis

$$\begin{aligned} \tilde{H} &= \mathbf{U}^\dagger \widehat{H} \mathbf{U} \\ \tilde{\mu} &= \mathbf{U}^\dagger \widehat{\mu} \mathbf{U} \\ \tilde{\rho} &= \mathbf{U}^\dagger \rho \mathbf{U} \\ \mathrm{vec}\,(\tilde{\rho}) &= \mathbf{U}^\dagger \otimes \mathbf{U}^\dagger \mathrm{vec}\,(\rho)\,, \end{aligned} \tag{C.06.2}$$

or approximate the exponential function without diagonalizing the matrix. While the first approach is faster for the smaller, dense matrices, the second is getting preferable for bigger and sparser matrices.

C.07 Chebyshev polynomial propagator

A very nice overview of the methods to compute the exponential function of a matrix without diagonalizing it is given in Ref. [22]. One of those methods is the Chebyshev polynomial approximation, which was suggested for use as a short-time propagator in Refs. [31,32]. As it was mentioned in the previous section, the Hamiltonian and dipole matrices we intend to use are extremely sparse (only a few percent of the matrix elements are non-zeros) and we want to take advantage of this property in our computational routines and storage formats. Before we continue with the implementation details, we want to refer to [33] that covers the necessary basics of matrix computations. For information about sparse matrix formats and their applications we recommend Refs. [34–36].

Since the fill-in and sparsity patterns of the matrices that will be used later are unknown and both factors influence the performance of the matrix operations very strongly, we will test our routines for dense matrices, which is expected to be the worst possible performance scenario.

without permutation

	matrix:	f164			
	vector:	f164			
#CPUs	1	2	4	8	12
CSR	743	401	322	268	264
CSRd	839	450	339	275	264
dense			317		
	matrix:	f164			
	vector:	c128			
#CPUs	1	2	4	8	12
CSR	940	480	360	277	265
CSRd	805	466	352	276	264
	matrix:	c128			
	vector:	c128			
#CPUs	1	2	4	8	12
CSR	1310	845	526	396	355
CSRd	1677	885	589	472	442
dense			682		

with a random permutation

	matrix:	f164			
	vector:	f164			
#CPUs	1	2	4	8	12
CSR	1130	623	444	306	270
CSRd	1148	658	475	305	270
dense			378		
	matrix:	f164			
	vector:	c128			
#CPUs	1	2	4	8	12
CSR	1154	684	424	295	269
CSRd	1156	681	425	297	269
	matrix:	c128			
	vector:	c128			
#CPUs	1	2	4	8	12
CSR	1824	1042	691	505	448
CSRd	1984	973	548	343	290
dense			685		

Table C.1: Symmetric (Hermitian) dense matrices with a dimension 20000 filled with random data of real (`f164`) or complex (`c128`) type were multiplied 500 times with a vector of real or complex type. Matrix-vector products were performed for CSR, CSRd (or MSR) [34, 35] and NumPy Array data storage format. The walltime in seconds is estimated for different matrix types and different CPU numbers.

A Chebyshev polynomial approximation for the exponential function in Hilbert and Liouville space was implemented for the current work. We have used the Python and C programming languages, and the shared memory multiprocessing (OpenMP) libraries [37]. The routine is written to be compatible with any matrix-vector multiplication available in the code. The NumPy [38] package suite has

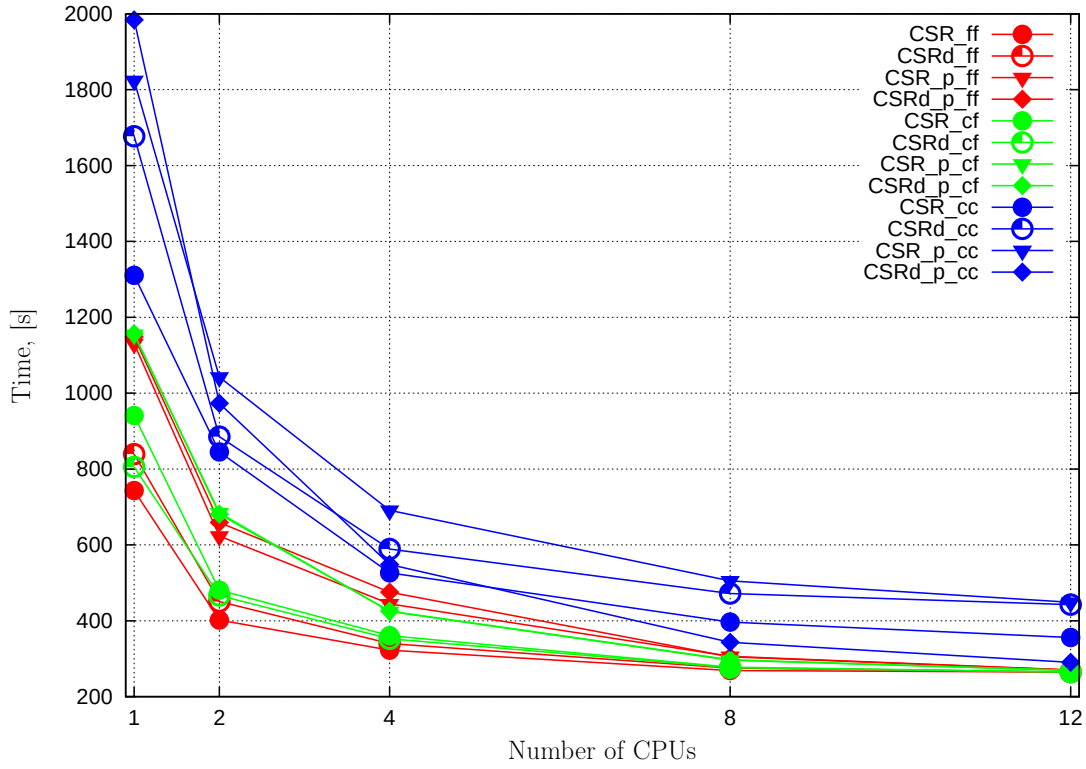

Figure C.14: Walltime (in seconds) as a function of CPU numbers used for the matrix-vector products (data from Tab. C.1). Only CSR and CSRd (or MSR) [34, 35] data storage types are shown, `_p` indicates that a random permutation was used and `_ff (float64-float64)`, `_cf (complex128-float64)` and `_cc (complex128-complex128)` indicate the types of matrix and vector.

a fast matrix-vector multiplication (`dense` in Tab. C.1). But this routine can not handle sparse matrix formats and is therefore inappropriate for large matrices (dimensions larger then 20000-50000). It is not parallelized and has problems with handling data of different numeric data types at its current version.[§] A permutation function ($\vec{y} = \mathbf{A}p(\vec{x})$ instead of $\vec{y} = \mathbf{A}\vec{x}$) can sometimes be very useful in applications and is implemented as well.

The performance of the implemented routines was tested on randomly generated dense square matrices with dimension 20000. The times in seconds needed to perform 500 matrix-vector products for different data types, storage formats and CPU counts is presented in Tab. C.1. The test matrices were symmetric if `float64` and Hermitian if `complex128` data types were used. The comparison to

[§]NumPy version 1.4.1 is used.

standard, not parallelized, NumPy matrix-vector products for `float64-float64` and `complex128-complex128` data types with and without a random permutation is shown in Tab. C.1. The `complex128-float64` matrix-vector products are also implemented, but no comparison to the NumPy routine is given, because of the very poor simultaneous handling of different numeric data types by the current version of NumPy, which results in inadequate performance times (more than 3000 instead of ≈ 400 seconds).

In Fig. C.14 we plot the times presented in Tab. C.1 as a function of the CPU number. Using two CPUs instead of one reduces the walltime almost by a factor of two. Using four CPUs reduces the walltime by further 25 percent. Larger CPU counts reduce the total time further but not as significantly as two to four processors.

C.08 Semiclassical approximation in practice

So far we have considered only the origin and positions of the spectral features in 2D spectra. Now we are going to take a closer look at their shape. The physical reasons, why the peaks do not appear to be infinitesimally sharp in the spectra are discussed in Sec. B.07 and B.08. Since the spectral features are not easily recognizable if they are infinitesimal sharp, a phenomenological Gaussian broadening (with a FWHM set to 20 cm^{-1}) was applied throughout Sec. C.02.

At this point we want to apply the theory from Sec. B.07 to our previously computed spectra. Two parameters are introduced – the homogeneous vibrational dephasing time T_2^* (or the homogeneous dephasing rate $(T_2^*)^{-1}$) which is usually about 0.5 to 2 ps for molecules in the liquid state or solution and the fluctuation amplitude $\Delta\omega$ up to 100 cm^{-1} (inhomogeneous broadening), which is equivalent to a rate of approximately 0.5 ps^{-1}.

In Fig. C.15 we show the same third order response functions as in the lowest left spectrum of Fig. C.13. Instead of the Gaussian broadening we are now using semiclassical homogeneous and inhomogeneous dephasing with different values for the $(T_2^*, \Delta\omega)$ tuples. The larger the $\Delta\omega$, the longer the peaks along the diagonal and the smaller the T_2^*, the broader the peaks. This result is in direct agreement to the literature [1] for a Photon-Echo experiment.

A big advantage of the semiclassical approximation is its flexibility. The homogeneous and the inhomogeneous effects can be included into every approximation used in this work independently and at a low computational cost.

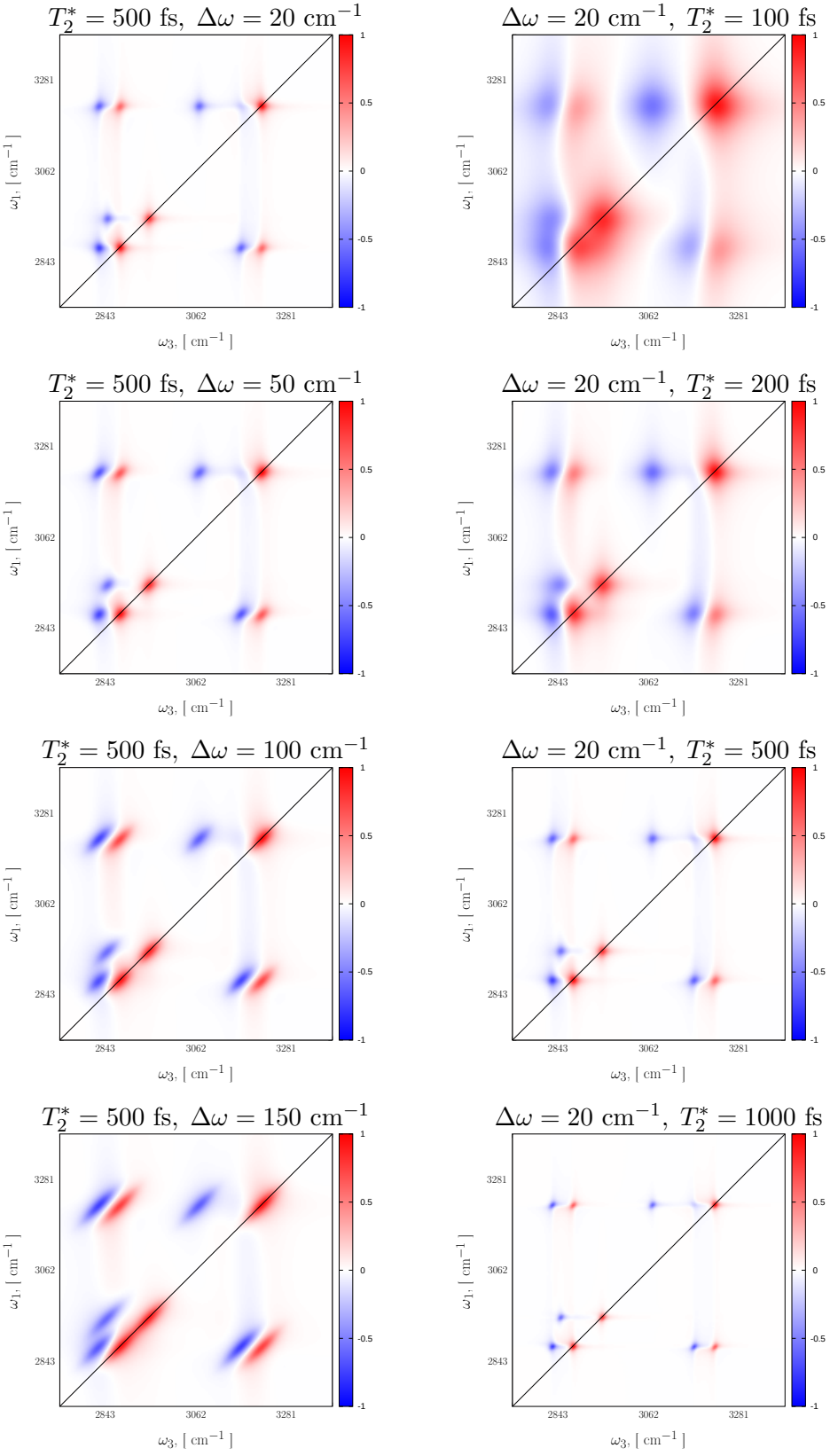

Figure C.15: Illustration of the semiclassical approximation of dephasing for the example of the third order response functions (compare to lowest left spectrum in Fig. C.13). T_2^* is the homogeneous dephasing time and $\Delta\omega$ is the fluctuation amplitude.

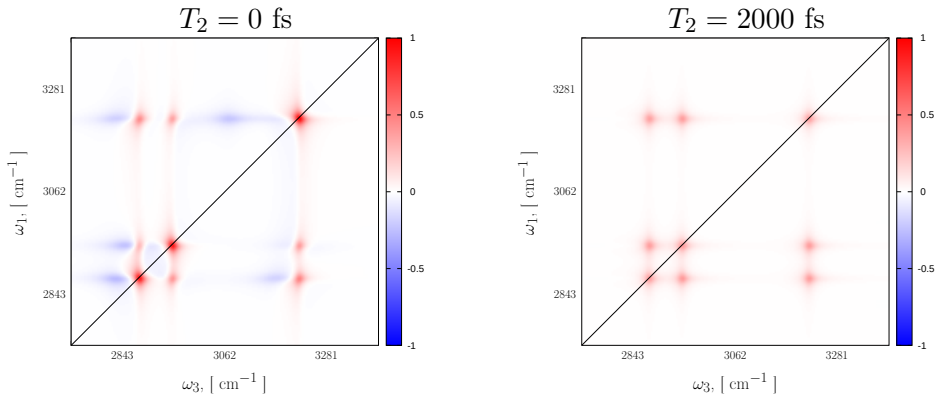

Figure C.16: Third order response functions computed using the relaxation matrix introduced in the Eq. (C.09.1). Relaxation rates to the ground state are set to ≈ 1000 fs^{-1}, all other relaxation rates set to 0. No semiclassical dephasing.

C.09 Introducing a relaxation matrix

In Sec. B.08 we have introduced the concept of a relaxation matrix along with some conditions it must fulfill. Now we want to take a closer look at Eq. (B.08.7) and its possible implementation. Applying the rules of the vectorization operators, we can write

$$\begin{aligned}
\mathrm{vec}\left(\widehat{W}\rho\right) &= \mathbf{1}\otimes\widehat{W}\,\mathrm{vec}\left(\rho\right) \\
&= \sum_k \frac{\gamma_k}{2}\left(2\left(\widehat{\sigma}_k^\dagger\right)^T\otimes\widehat{\sigma}_k - \mathbf{1}\otimes\widehat{\sigma}_k^\dagger\widehat{\sigma}_k - \left(\widehat{\sigma}_k^\dagger\widehat{\sigma}_k\right)^*\otimes\mathbf{1}\right)\mathrm{vec}\left(\rho\right) \\
&= \sum_k \frac{\gamma_k}{2}\left(2\widehat{\sigma}_k^*\otimes\widehat{\sigma}_k - \mathbf{1}\otimes\widehat{\sigma}_k^\dagger\widehat{\sigma}_k - \left(\widehat{\sigma}_k^\dagger\widehat{\sigma}_k\right)^*\otimes\mathbf{1}\right)\mathrm{vec}\left(\rho\right) \qquad \text{(C.09.1)}
\end{aligned}$$

assuming that the operators $\widehat{\sigma_k}$ are real, this expression can be simplified to

$$= \sum_k \frac{\gamma_k}{2}\left(2\widehat{\sigma}_k\otimes\widehat{\sigma}_k - \mathbf{1}\otimes\widehat{\sigma}_k^T\widehat{\sigma}_k - \widehat{\sigma}_k^T\widehat{\sigma}_k\otimes\mathbf{1}\right)\mathrm{vec}\left(\rho\right) \qquad \text{(C.09.2)}$$

using the properties of the direct matrix product we can further write

$$= \left(\sum_k \gamma_k\,\widehat{\sigma}_k\otimes\widehat{\sigma}_k - \mathbf{1}\otimes\sum_k\frac{\gamma_k}{2}\widehat{\sigma}_k^T\widehat{\sigma}_k - \sum_k\frac{\gamma_k}{2}\widehat{\sigma}_k^T\widehat{\sigma}_k\otimes\mathbf{1}\right)\mathrm{vec}\left(\rho\right) \qquad \text{(C.09.3)}$$

with $\widehat{\Sigma} = \sum_k \frac{\gamma_k}{2} \widehat{\sigma}_k^T \widehat{\sigma}_k$ the previous expression can be written as

$$= \left(\sum_k \gamma_k \, \widehat{\sigma}_k \otimes \widehat{\sigma}_k - \mathbf{1} \otimes \widehat{\Sigma} - \widehat{\Sigma} \otimes \mathbf{1} \right) \mathrm{vec}\,(\rho)\,. \tag{C.09.4}$$

In Eq. (C.09.4) the operator $\widehat{\Sigma}$ can be computed before the direct matrix product, which is computationally cheaper than the sum of direct products. This equation represents the Lindblad-Kossakowski approximation [19, 20] in the Liouville space for the vectorized density matrices. The operators σ_k can be chosen depending on the required sophistication, with relative rates γ_k of the respective processes. This way, we may easily incorporate any dissipative processes in question.

For the purposes of this work, we define the lowering operators σ_k and the raising operators σ_k^T. The index k runs over all allowed transitions. The rates γ_k can be chosen depending on the required broadening or estimated from experimental data. To fulfill the detailed balance condition (see Eq. (B.08.1)) the rate of any upward transition (σ_k^T) is equal to the respective downward transition (σ_k) rate times the respective Boltzmann factor

$$\frac{\gamma_{0\to1}}{\gamma_{1\to0}} = \exp\left\{ -\frac{\hbar\omega_{01}}{k_B T} \right\}, \tag{C.09.5}$$

with Boltzmann constant k_B and temperature $T = 300$ K (room temperature). The density matrix at τ_0 is populated with respect to the Boltzmann factors (thermalized)

$$\rho(0)_{ij} \propto \exp\left\{ -\frac{\hbar\omega_i}{k_B T} \right\} \delta_{ij}. \tag{C.09.6}$$

One of the main computational challenges in the description of the relaxation processes with the Liouville space based methods is the dimensionality of the problem. The dimensions of the $\mathbf{1} \otimes \widehat{W}$ operator is $N^2 \times N^2$ and even if this operator can remain sparse, the density matrix has to be a dense matrix with dimensions $N \times N$ (or vector with dimensions $N^2 \times 1$). This results in highly super linear scaling of the computational cost of the method with system size.

To examine the relaxation on example third order response functions for the relaxation operator defined in Eq. (C.09.4) we set the relaxation processes $\gamma_k \sigma_k$ equal to the dipole matrix elements times the parameter γ. The parameter γ gives us a possibility to increase or decrease the overall relaxation rate. In Fig. C.16 we calculate spectra with population times (T_2) set to 0 (top spectrum) and 2000 fs (bottom spectrum). The intensities of the peaks in the bottom spectrum are much lower (about 40%) than in the top spectrum. Another important change is the lower intensity of the negative bands in the upper spectrum in Fig. C.16 in comparison to Fig. C.13 and Fig. C.15. The reason for that is the relaxation from the excited state during the t_1 and t_3 periods of time.

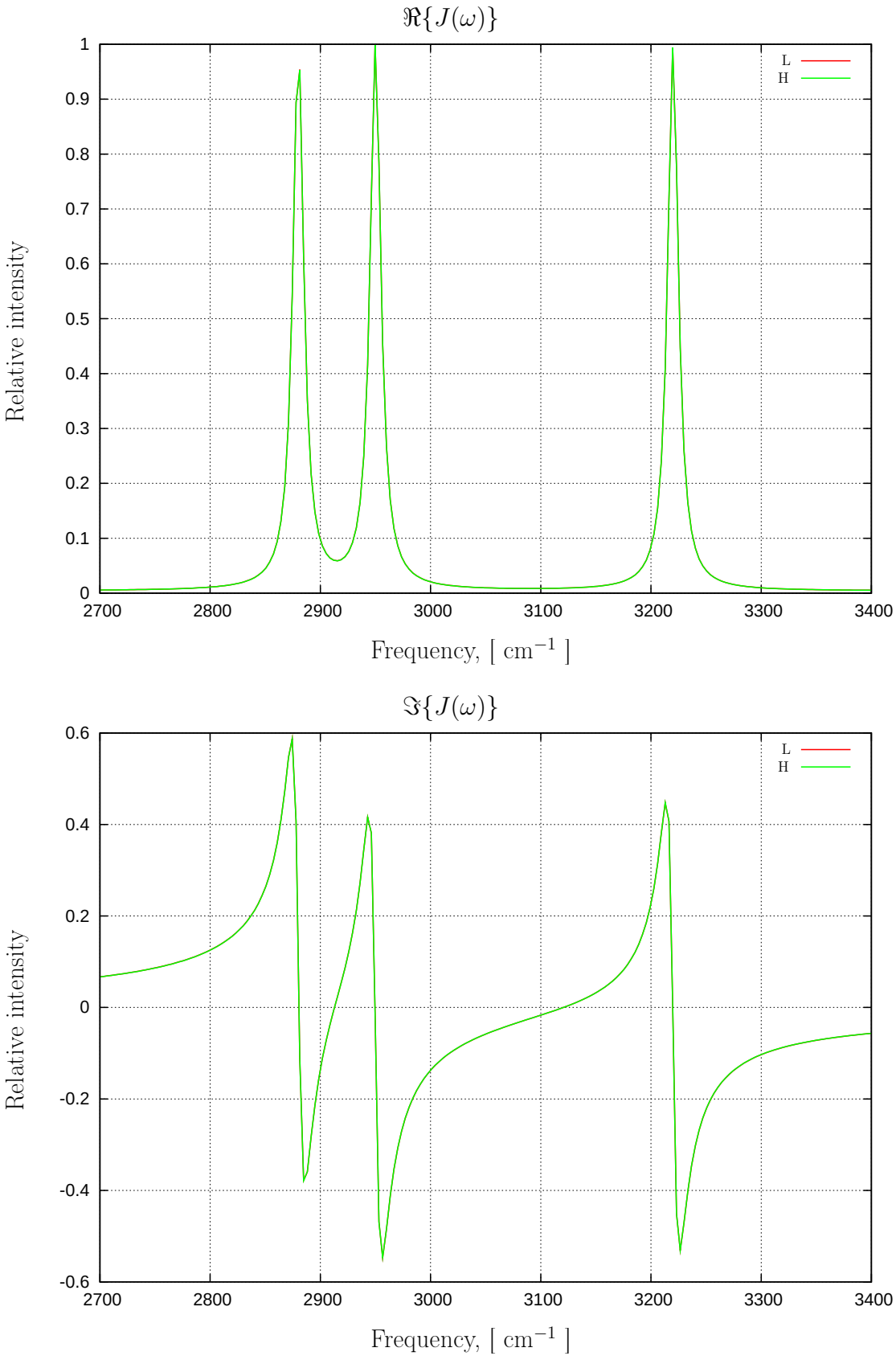

Figure C.17: Real ($\Re\{J(\omega)\}$) and imaginary ($\Im\{J(\omega)\}$) parts of the first order response function ($J(\omega)$) computed in Liouville space (L) compared to those computed in doubled Hilbert space (H). The jump probability is set to 0 (no quantum jumps).

C.10 Wavefunction based propagation

The disadvantage of the unfavourable computational cost of the Liouville space based methods is even more apparent when dealing with the dissipation, as described in Sec. C.09.

In Sec. B.09 we have shown, that the random environmental effects can be equally described by the master equation in Liouville space and by the quantum stochastic differential equations in Hilbert space. Before introducing the quantum jump approach from Sec. B.11 we want to examine a *no-jump* Hilbert space propagation, with the relaxation matrix defined the same way as in Sec. C.09.

The comparison of the first order response functions computed in Liouville space to those computed in doubled Hilbert space without quantum jumps is presented in Fig. C.17. For the first order response functions ($J(\omega)$) computed in this section a 5 cm^{-1} resolution was used.¶

The spectra in Fig. C.17 are identical. This means, that our benchmark system is simple enough and can be described with a pure state. Therefore no quantum jumps are needed. In the next chapter we will use the algorithm presented in Sec. B.11 for the example of molecular Hamiltonians, which can not be described with pure states anymore.

C.11 Chemical exchange

We want to consider the dynamics of a chemical exchange process because its description requires more than a pure state and is therefore a good example for the introduction of both the doubled Hilbert space propagation (Sec. B.10) and the Monte Carlo Sampling algorithm (Sec. B.11).

We will start with the three anharmonic oscillators we have introduced in Sec. C.06 and change the fundamental frequency of the third oscillator by 100 cm^{-1} ($\omega_{01}^{c_2} = 3320$ cm^{-1} instead of 3220 cm^{-1}) mimicking e.g. a change of this oscillators environment by some external process. The dipole matrix of the modified system is equal to the dipole matrix of the original system $\widehat{\mu}_2^{3AO} = \widehat{\mu}^{3AO}$. If we want to allow chemical exchange between those two systems, we will have to include both of them into the propagation thus doubling the dimensionality of the problem. The new Hamiltonian matrix will become

¶ If we want a response function with a maximal frequency of 7000 cm^{-1} and the frequency resolution of 10 cm^{-1}, we will need 1400 points per time dimension and zero filling up to at least 2048 points for 1D-FFT. For the 2D third order response function we have to compute 1,960,000 (1400×1400) and store 4,194,304 (2048×2048) points (of complex data type). This example shows that computing and saving first order response function does not present any difficulties. On the other hand the resolution limit for the third order response functions has to be considered more carefully.

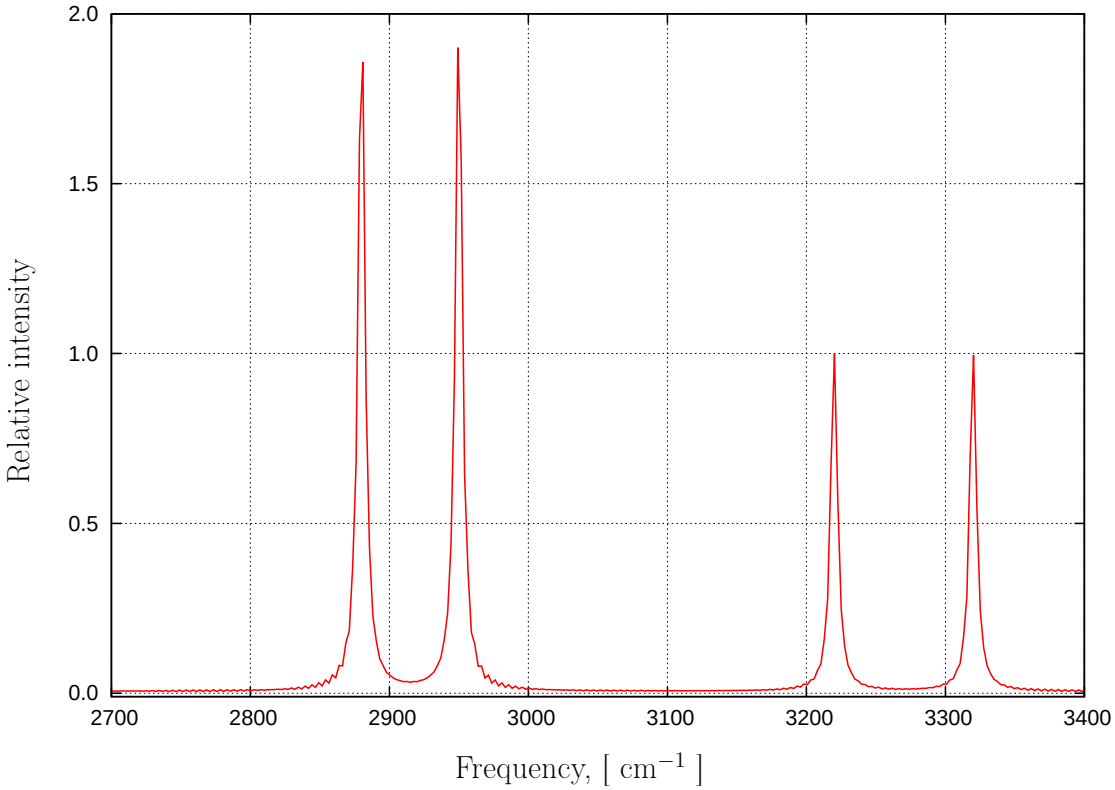

Figure C.18: The real part of the first order response function ($J(\omega)$) for the doubled three oscillator system. The first two oscillators have frequencies $\omega_{01}^{a} = 2880$ cm^{-1} and $\omega_{01}^{b} = 2950$ cm^{-1} in both states. The third oscillator has frequencies $\omega_{01}^{c_1} = 3220$ cm^{-1} and $\omega_{01}^{c_2} = 3320$ cm^{-1}. The rate of chemical exchange r_0 is set to 0.

$$\widehat{H}^{\mathrm{II}} = \begin{pmatrix} \widehat{H} & 0 \\ 0 & \widehat{H}_2 \end{pmatrix}, \tag{C.11.1}$$

with the Hamiltonian matrix $\widehat{H}$ taken from Sec. C.06 and the modified Hamiltonian matrix $\widehat{H}_2$. The doubled dipole matrix will become

$$\widehat{\mu}^{\mathrm{II}} = \begin{pmatrix} \widehat{\mu}^{\mathrm{3AO}} & 0 \\ 0 & \widehat{\mu}^{\mathrm{3AO}} \end{pmatrix}. \tag{C.11.2}$$

We will also introduce the exchange operator in accordance with Refs. [9, 30]

$$\widehat{X} = \begin{pmatrix} 0 & \mathbf{1} \\ \mathbf{1} & 0 \end{pmatrix}, \tag{C.11.3}$$

where $\mathbf{1}$ is the unity matrix of the dimension equal to the dimension of $\widehat{H}$.

In Fig. C.18 we show the real part of the first order response function ($J(\omega)$) for the doubled system with exchange rate $r_0 = 0$. Using the same normalization factor as in Fig. C.17 we see that peaks of the first two oscillators overlap causing the doubled intensities of these bands, whereas the intensities of the peaks at 3220 and 3320 cm^{-1} are equal to 1.

In Fig. C.19 we introduce chemical exchange with different probabilities of exchange transitions (relative rates). The spectrum without exchange is presented in red. With a low probability of exchange (green spectrum) the peaks are getting smaller and broader. The blue spectrum has a higher exchange rate and is close to coalescence (both peaks nearly disappeared). Even higher rates lead to single sharp peak at 3270 cm^{-1} (purple and black spectra) by motional narrowing.

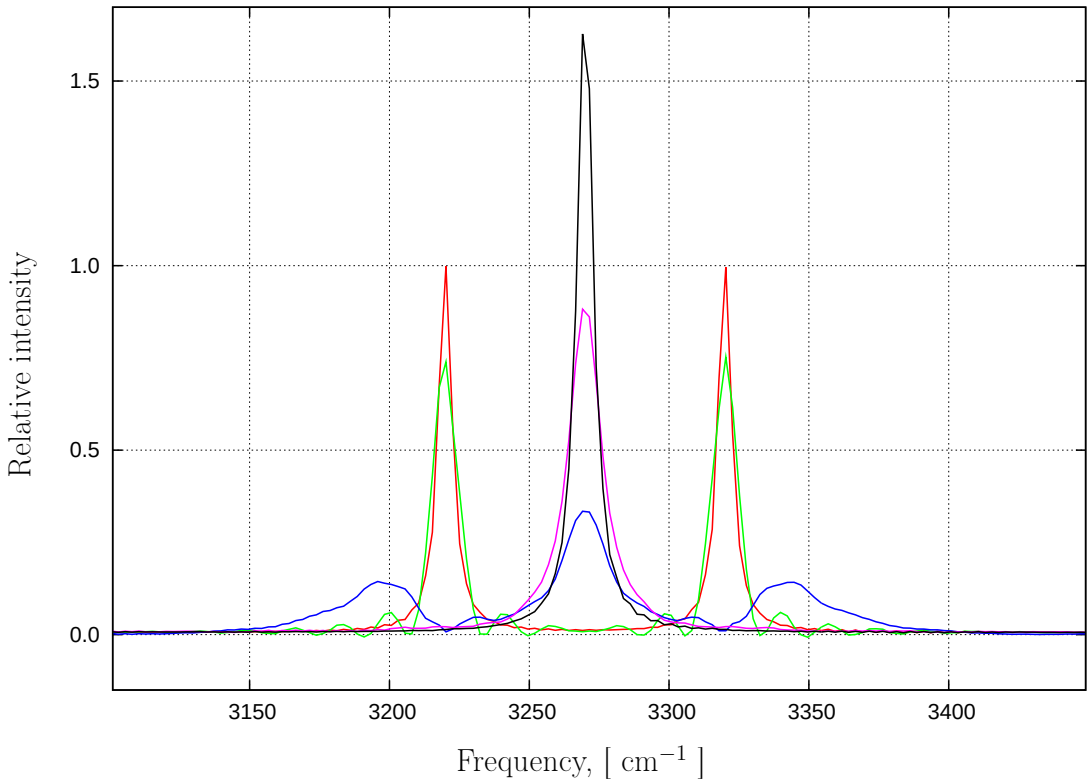

Figure C.19: The real part of the first order response function ($J(\omega)$) for the doubled three oscillator system in the spectral window between 3100 and 3450 cm^{-1}. The relative rates of the chemical exchange are $r_{\mathrm{red}} = r_0 = 0 < r_{\mathrm{green}} < r_{\mathrm{blue}} < r_{\mathrm{purple}} < r_{\mathrm{black}}$.

In Fig. C.20 we examine the third order response functions for the same doubled three anharmonic oscillator system with chemical exchange. The population time T_2 is set to zero. With exchange rate equal to zero ($r_0 = 0$) we can see two

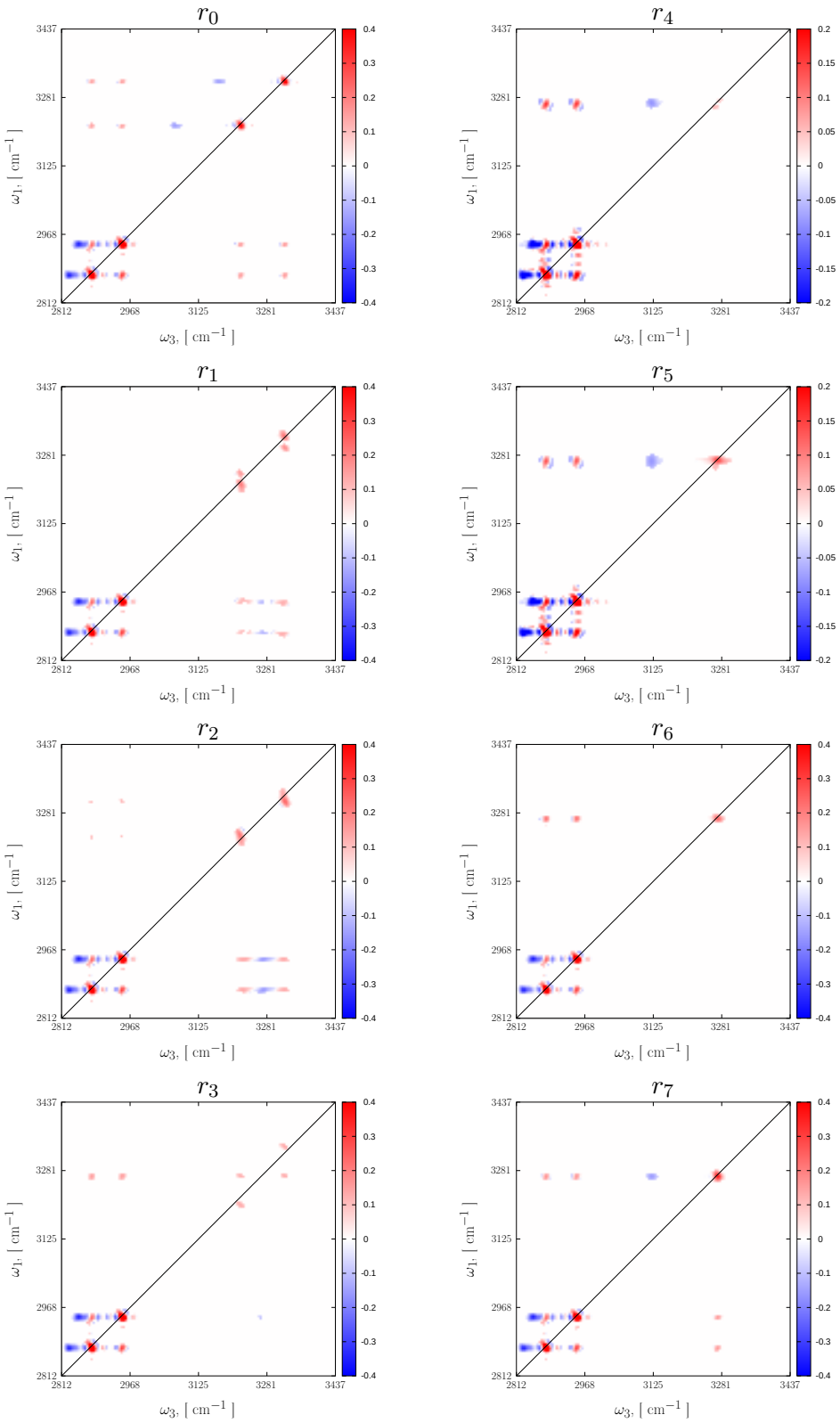

Figure C.20: Third order response functions computed using the Monte Carlo Sampling algorithm (Sec. B.11) for the doubled three anharmonic oscillator system with chemical exchange (see text). The relative rates of exchange are: $r_0 = 0 < r_1 < r_2 < r_3 < r_4 < r_5 < r_6 < r_7 \to \infty$. The r_4 and r_5 spectra are magnified two times. Population time $T_2 = 0$.

peaks at 2880 and 2950 cm^{-1} with intensity normalized to 1 and two peaks at 3220 cm^{-1} and 3320 cm^{-1} with half of the intensity in correspondence to the first order response function in Fig. C.18. The increase of the relative rate reduces the intensity of the last two peaks and elongates them in the frequency time domain (r_1 and r_2). With exchange rate r_3 we observe the onset of coalescence represented by the blue spectrum in Fig. C.19. Further increase of the exchange rate leads to almost complete disappearance of both peaks (r_4 and r_5). After that a sharp peak appears at 3270 cm^{-1} (r_6, r_7) due to motional narrowing.

In Fig. C.21 we take a lower exchange rate (r_1 from previous example) and increase the population time T_2. After 750 fs the exchange cross peaks appear in the spectrum, while chemical exchange would not be detectable in 1D spectra of this system.

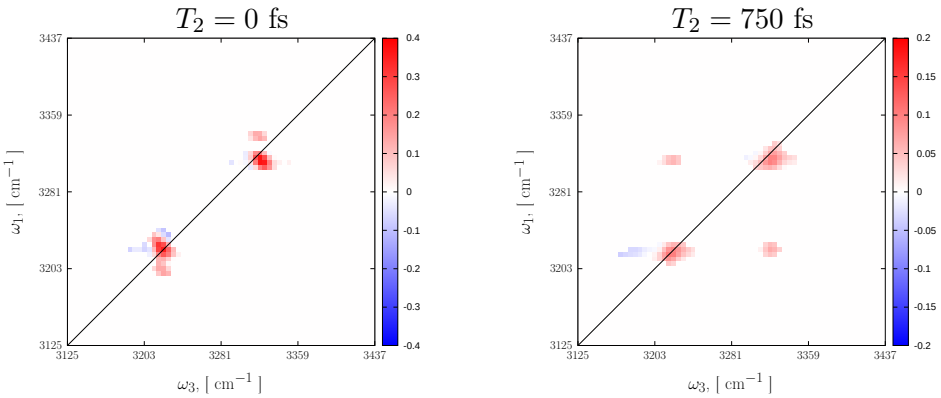

Figure C.21: Third order response functions computed using the Monte Carlo Sampling algorithm (Sec. B.11) for the doubled three anharmonic oscillator system with chemical exchange for the population times $T_2 = 0$ and 750 fs (see text).

Chapter D

Monte Carlo Sampling of Liouville Space Pathways

As a benchmark system for the Monte Carlo Wave Packet Sampling we are going to use the water (Sec. D.01) and formamide (Sec. D.02) molecules. Their Hamiltonian and dipole matrices were computed within the scope of our institute collaboration [39]. The theory behind the build-up of vibrational configuration interaction (VCI) matrices was described in [36,40–43] and will not be further discussed in this work. In this chapter we plot 2D spectra with the first time domain along the abscissa and third time domain along the ordinate.

D.01 Dihydrogen monoxide

With only three atoms and three normal modes, the water molecule (Fig. D.1) is one of the simplest benchmark systems to study vibrational motions. The 38

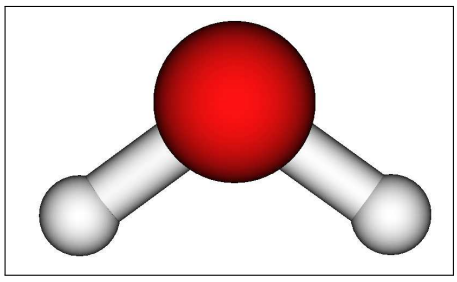

Figure D.1: Optimized geometry of water molecule (see Appendix G.01).

dimensional Hamiltonian and dipole matrices are computed with the semiclassical PM3 method [44, 45] and the configuration selection algorithm presented in [39].

$(0,0,0)$	$(3,0,0)$	$(2,2,0)$	$(3,0,2)$
$(1,0,0)$	$(0,3,0)$	$(2,0,2)$	$(2,3,0)$
$(0,1,0)$	$(0,0,3)$	$(1,3,0)$	$(2,0,3)$
$(0,0,1)$	$(2,1,0)$	$(1,0,3)$	$(0,4,1)$
$(2,0,0)$	$(2,0,1)$	$(0,3,1)$	$(0,3,2)$
$(0,2,0)$	$(1,2,0)$	$(0,2,2)$	$(2,2,1)$
$(0,0,2)$	$(1,0,2)$	$(2,1,1)$	$(1,3,1)$
$(1,1,0)$	$(0,2,1)$	$(1,2,1)$	$(0,4,2)$
$(1,0,1)$	$(0,1,2)$	$(1,1,2)$	
$(0,1,1)$	$(3,0,1)$	$(4,0,1)$	

Table D.1: 38 vibrational configurations of water that survive the configuration selection algorithm [39]. Three numbers in parentheses represent three normal modes and their excitation levels.

The configurations selected this way can be found in Tab. D.1. The configuration list consist of the ground state, fundamentals, first and second overtones and combination modes.

The red spectrum in Fig. D.2 is the linear absorption spectrum of a water molecule computed from the Hamiltonian eigenvalues with intensities proportional to the squares of the transition dipole moments [2]. The peaks are plotted with an artificial Lorentz-type broadening of 2 cm^{-1}. The z axis lies perpendicular to the molecular plane and therefore there is no dipole moment change along the z axis and no linear absorption associated with the z component of the dipole moment (purple spectrum in Fig. D.2). The peaks at 1672 cm^{-1} and 3809 cm^{-1} are associated with the change of the y component of the dipole moment and present symmetric OH bend and stretch vibrations (front blue line in Fig. D.2). The second blue spectrum is computed as the first order response function in doubled Hilbert space with the algorithm described in Sec. B.11. The necessary number of quantum jumps per trajectory is lower than 20 and one needs less than 10 trajectories for convergence. The small peak at 3295 cm^{-1} is the first overtone of the symmetric bending mode. The almost disappearing peak at around 2000 cm^{-1} (encircled) is a higher combination mode and it appears in the spectrum due to the aliasing effect described in Sec. C.02.

The linear absorption spectrum associated with the x component of the dipole moment (front green line in Fig. D.2) consists of the asymmetric OH stretch at 3691 cm^{-1}. As in the case of the y component, the second green spectrum is computed in doubled Hilbert space with the algorithm described in Sec. B.11. The number of quantum jumps per trajectory is again lower than 20 and one needs less than 10 trajectories for convergence. We normalize all spectra to the

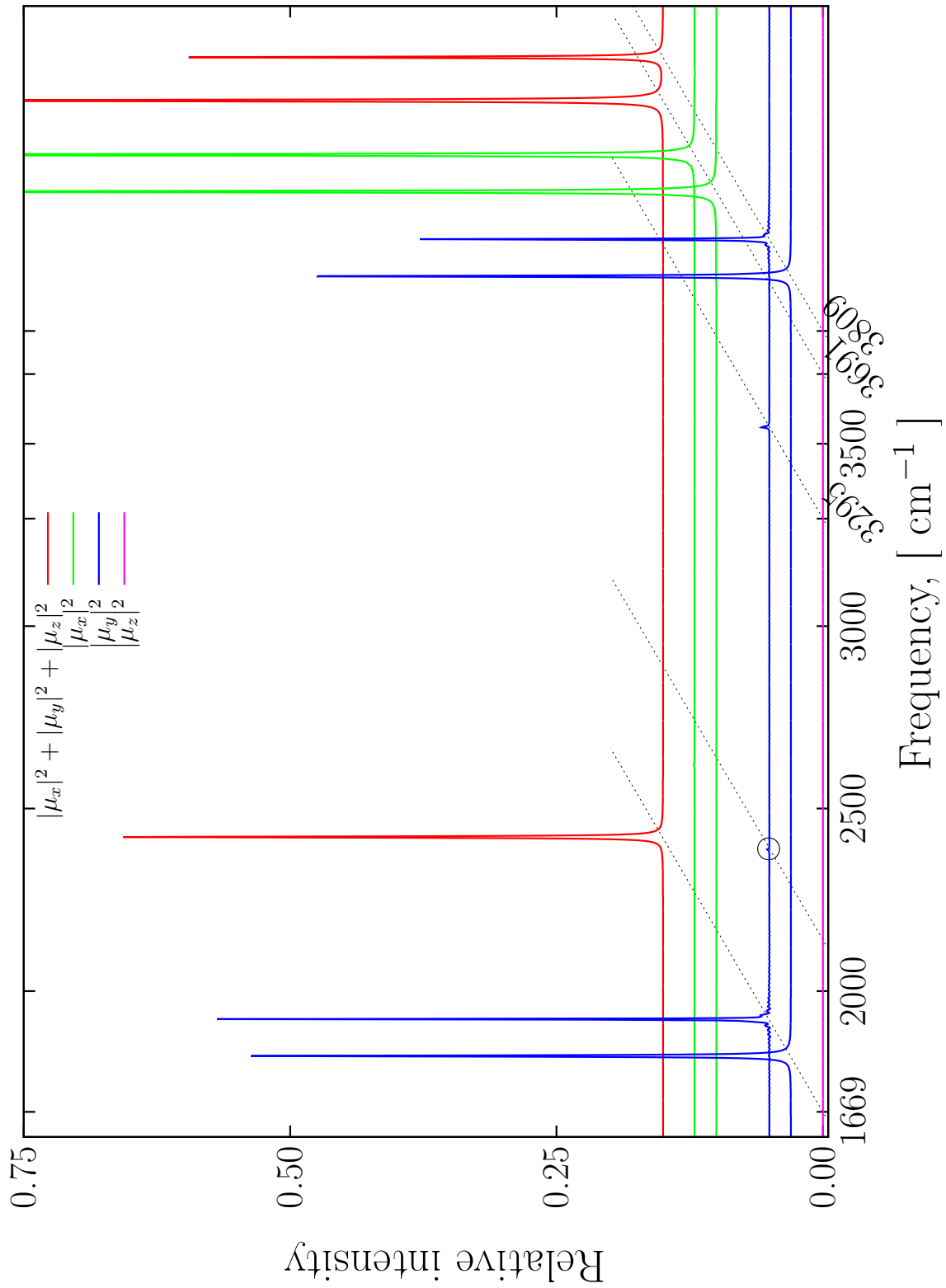

Figure D.2: Total linear absorption spectrum of the water molecule (red) and its x (front green), y (front blue) and z (purple) transition dipole moment components computed as eigenvalue spectra and x (second green), y (second blue) components computed as first order response functions using the Monte Carlo sampling algorithm described in Sec. B.11. The intensity of the x component of the dipole moment is normalized to 1 (off scale).

intensity of this band.

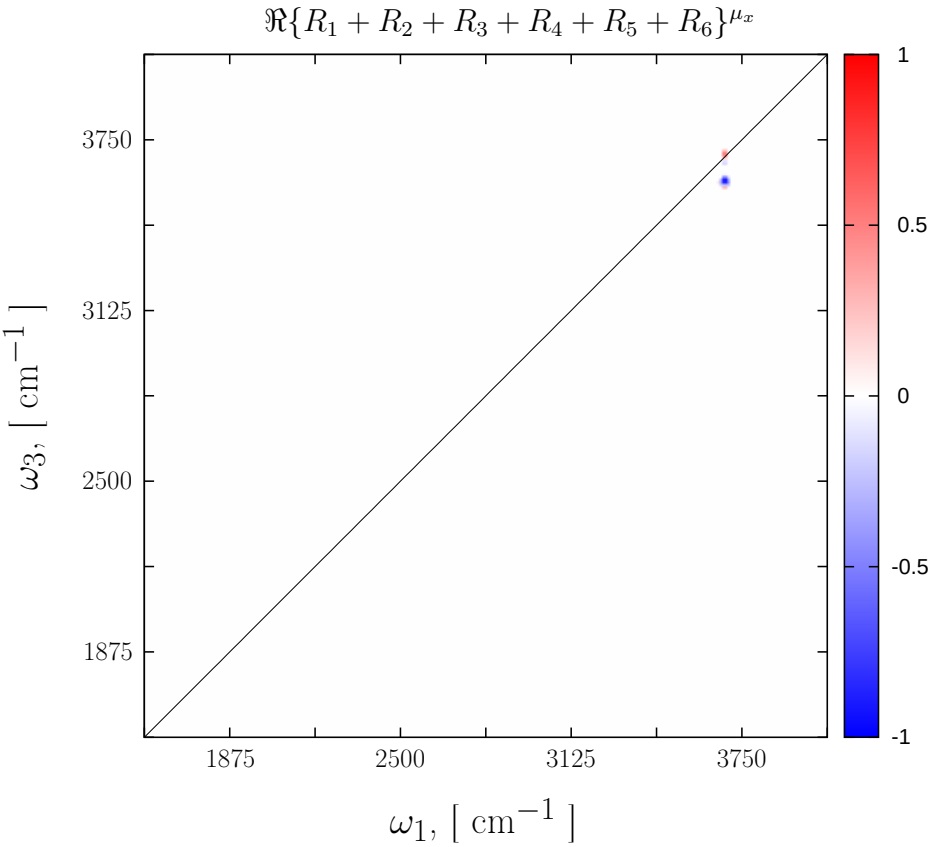

Figure D.3: The real parts of the third order response functions associated with the y component of the transition dipole moment computed using the Monte Carlo Wave Packet Sampling approach (see Sec. C.03 and Sec. B.11). The value of t_2 is set to zero. The intensity of the negative band is normalized to 1.

After the examination of the linear absorption spectra we want to take a closer look at the third order response functions computed with the Monte Carlo sampling algorithm. In Fig. D.3 we show the third order response function associated with the x component of the transition dipole matrix. The intensity of the highest signal in the spectrum is normalized to one. We can see the sharp absorptive signal is visible on the diagonal at 3691 cm^{-1} and a strong anharmonic peak with negative sign appears below it. Since it is the only asymmetric band, no other structure is visible in the spectrum.

The situation is very different for the y component of the transition dipole operator. In the upper spectrum in Fig. D.4 we see the expected diagonal peaks and their anharmonic counter parts at 1672 cm^{-1} and 3809 cm^{-1}. Those peaks

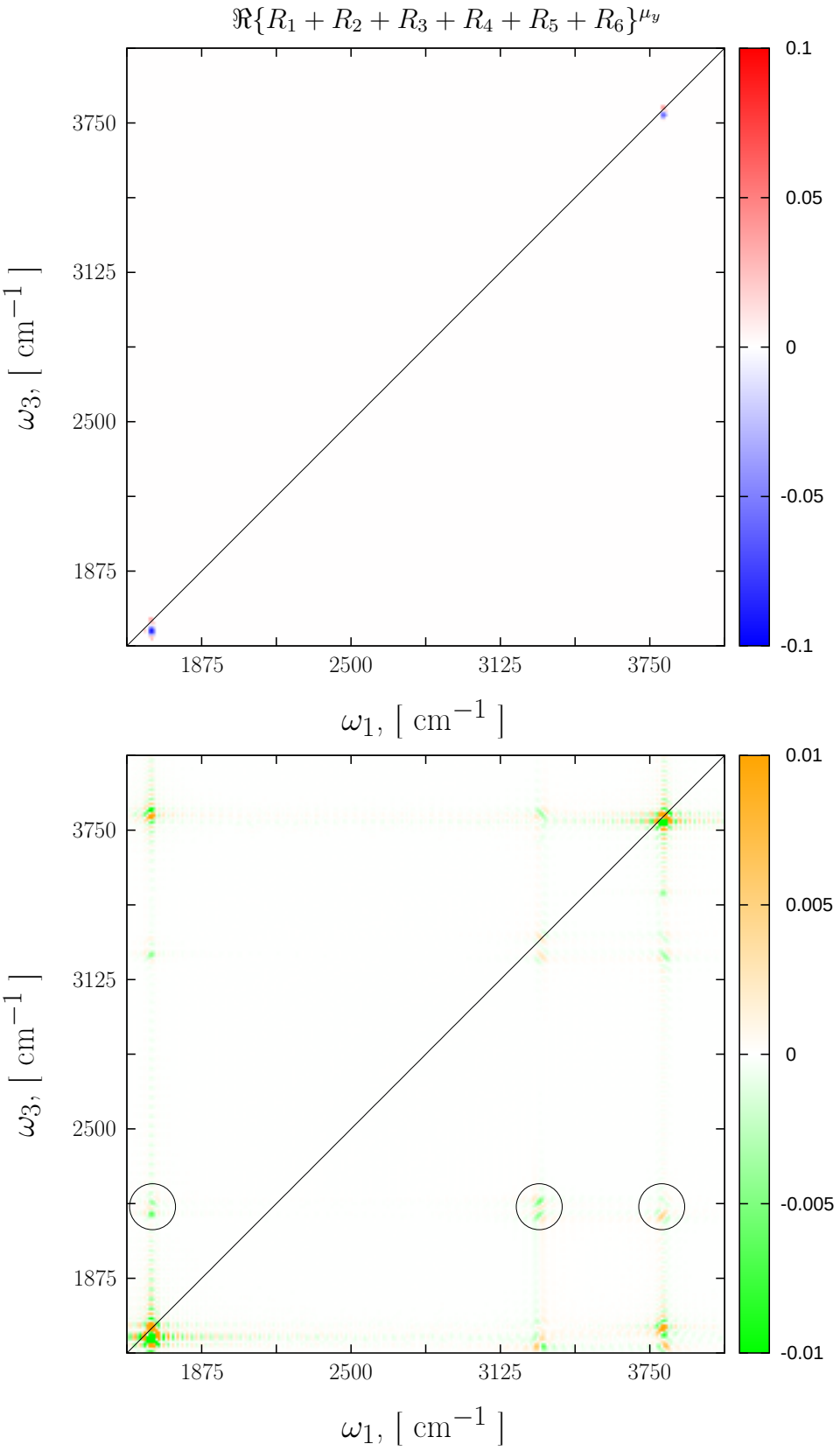

Figure D.4: The real parts of the third order response functions associated with the y component of the transition dipole moment computed using the Monte Carlo Wave Packet Sampling approach (see Sec. C.03 and Sec. B.11). The value of t_2 is set to zero. The same normalization constant as in Fig. D.3 was used. The lower spectrum is magnified ten times to show the fine structure of the spectrum. Aliased bands are indicated by circles.

are weaker than the x component peak. We use the same same normalization constant as in Fig. D.3 for comparison purposes. After tenfold magnification of the signal (lower spectrum in Fig. D.3) we observe a quite complex fine structure in the spectrum. The cross peaks with the overtone and the aliased band (indicated by circles) appear in the spectrum. This interaction is expected because of the symmetry of the underlying vibrational motions.

To generate the spectra in Figs. D.3 and D.4, the Monte Carlo sampling with only five trajectories per Feynman path and the Feynman paths denoted R_1, R_2, R_3, R_4, R_5 and R_6 in Chap. C were used.

D.02 Formamide

Formamide (see Fig. D.5) is the smallest model amide and is, with its six atoms and 12 normal modes, both a simple and interesting benchmark molecule. The VCI and

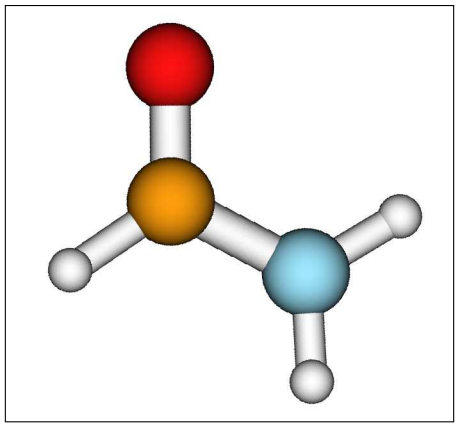

Figure D.5: Optimized geometry of formamide (see Appendix G.01).

transition dipole matrices of formamide used in this work are 1146 dimensional and were computed using the semiclassical PM3 method [44, 45], and the configuration selection algorithm presented in [39]. The normal modes of formamide with their respective VCI eigenvalues are shown in Fig. D.6.

In Fig. D.7 we show the total linear absorption spectrum (red) of formamide, as well as its x (green), y (blue) and z (purple) components. The eigenvalue spectra (front spectra in Fig. D.7) are compared to the Monte Carlo Wave Packet Sampling results (back spectra in Fig. D.7). The peaks are plotted with an artificial Lorentz-type broadening of 10 cm^{-1}. The intensity of the z component band at 107 cm^{-1} is normalized to 1. Having computed the absorption spectra for frequency ranges of 8000 and almost 12000 cm^{-1} we have not found any visible aliasing in the spectral window between 0 and 4000 cm^{-1}.

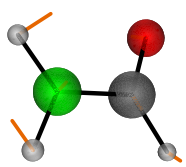

$(1,0,0,0,0,0,0,0,0,0,0,0)$
539 cm^{-1}

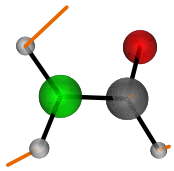

$(0,1,0,0,0,0,0,0,0,0,0,0)$
535 cm^{-1}

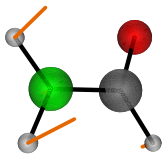

$(0,0,1,0,0,0,0,0,0,0,0,0)$
112 cm^{-1}

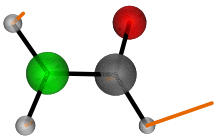

$(0,0,0,1,0,0,0,0,0,0,0,0)$
1001 cm^{-1}

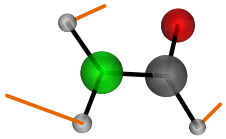

$(0,0,0,0,1,0,0,0,0,0,0,0)$
1082 cm^{-1}

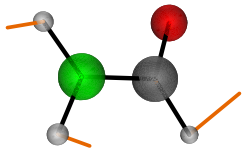

$(0,0,0,0,0,1,0,0,0,0,0,0)$
1189 cm^{-1}

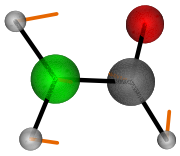

$(0,0,0,0,0,0,1,0,0,0,0,0)$
1365 cm^{-1}

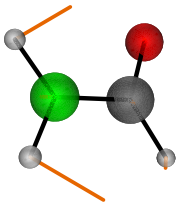

$(0,0,0,0,0,0,0,1,0,0,0,0)$
1621 cm^{-1}

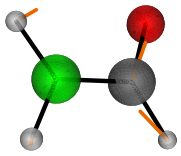

$(0,0,0,0,0,0,0,0,1,0,0,0)$
1941 cm^{-1}

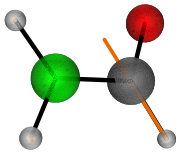

$(0,0,0,0,0,0,0,0,0,1,0,0)$
2988 cm^{-1}

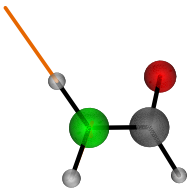

$(0,0,0,0,0,0,0,0,0,0,1,0)$
3351 cm^{-1}

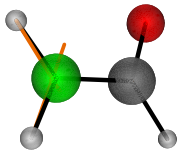

$(0,0,0,0,0,0,0,0,0,0,0,1)$
3398 cm^{-1}

Figure D.6: Normal mode basis of formamide. The orange lines represent the corresponding atomic displacements. Frequencies are based on PM3 calculations (see text).

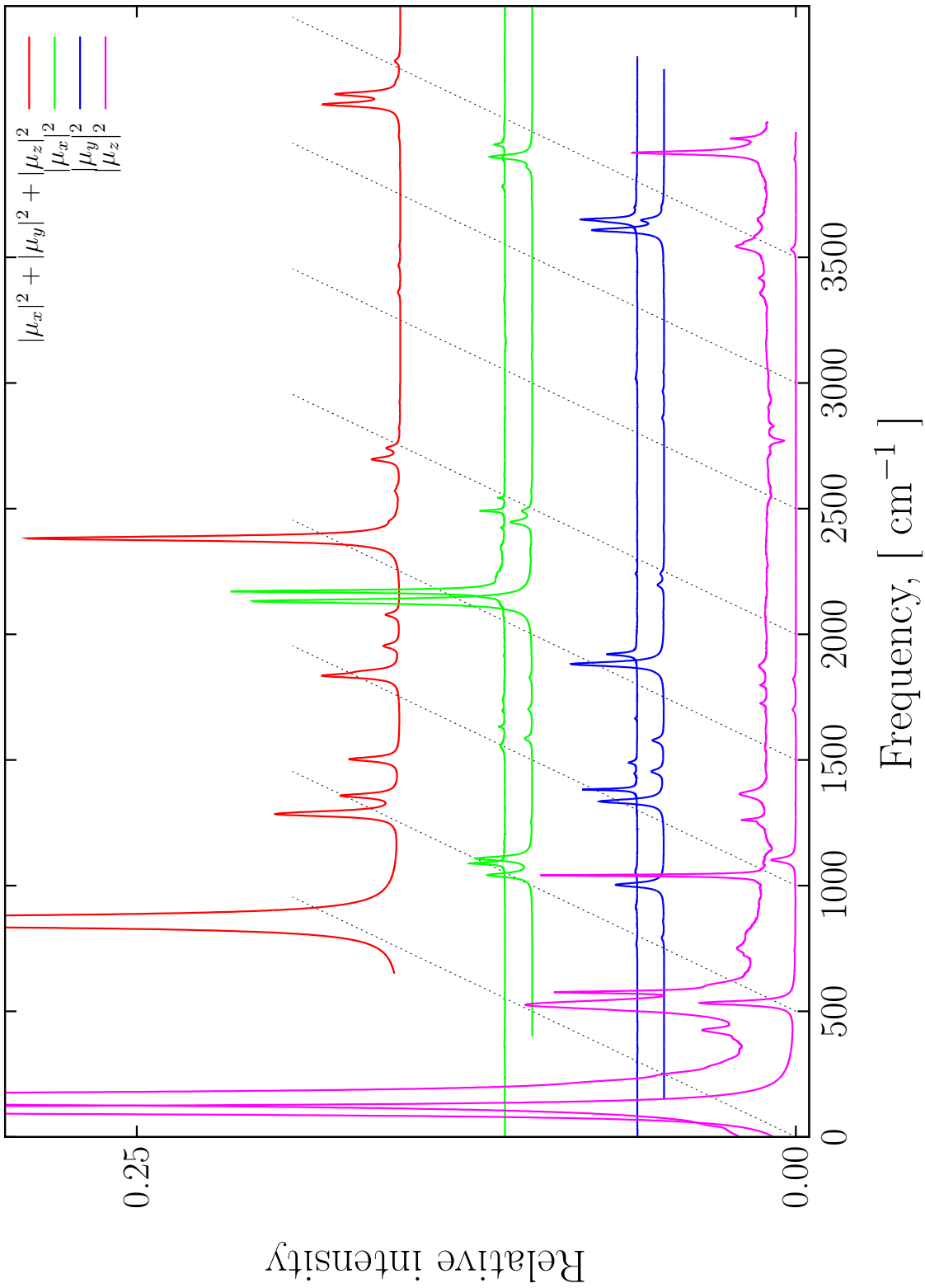

Figure D.7: Total linear absorption spectrum of formamide (red), its x (green), y (blue) and z (purple) transition dipole moment components computed as eigenvalue spectra and x (second green), y (second blue), z (second purple) components computed as first order response functions using the Monte Carlo sampling algorithm described in Sec. B.11. The intensity of the z component band at 107 cm^{-1} is normalized to 1 (offscale).

The linear absorption spectrum of formamide is very complex and can not be described with fundamental transitions only. We do not only see many new signals in the simulated spectra, but also the intensities of the peaks frequently differ. From the comparison between the front and back spectra of the same color in Fig. D.7 we can conclude that the fundamental excitations present an insufficient approximation for the linear absorption spectrum.

The 2D vibrational spectra of formamide are shown in Figs D.8, D.9, and D.10. As expected, the structure of the spectra is much more complex than in the case of the water molecule. As in the 1D spectrum we also see four diagonal peaks in Fig. D.8 (top spectrum), which is associated with the x component of the transition dipole moment. The diagonal peak at 539 cm^{-1} is associated with the in-plane NH_2 bending mode (see Fig. D.6). The highest intensity mode in this spectrum is the Amide II mode with the frequency 1621 cm^{-1}. It is the eighth normal mode of the molecule. The Amide II mode is coupled to the in-plane NH_2 band, Amide I, which is the second in intensity peak in the spectrum and is the ninth vibrational mode and is located at 1941 cm^{-1}. The fourth normal mode we observe is the symmetric NH_2 stretch mode (12th normal mode of formamide) at 3398 cm^{-1}. This vibrational motion is also coupled to the Amide II mode. Tenfold magnification of the signal unveils a complex pattern of couplings in the lower spectrum in Fig. D.8. Not only the peak at 1082 cm^{-1} becomes visible, but also many coupling bands not seen in the top spectrum of Fig. D.8.

The y component of the transition dipole moment shows three diagonal peaks in correspondence to the 1D spectrum and a coupling pattern between them (see top spectrum in Fig. D.9). The first diagonal peak corresponds to the fifth normal mode – NCO bending mode at 1082 cm^{-1}. We do not see the second NCO bending mode at 1189 cm^{-1} on the diagonal, because it has much smaller transition dipole moment than the first NCO band. Instead we observe a strong coupling of those two vibrational motions. It appears as a non-diagonal peak above the peak at 1082 cm^{-1}. The second diagonal peak is the Amide II mode at 1621 cm^{-1}. This mode is coupled to the NCO band at 1082 cm^{-1}. The third diagonal peak is the NH stretch at 3351 cm^{-1}. This vibrational motion is strongly coupled to the first overtone of the Amide II at 3231 cm^{-1} (peak below the diagonal). It is also coupled to the combination mode of its first excitation with the first excitation of the lowest energy out-of-plane NH_2 bending mode (peak above the diagonal). Yet another interesting fact is that the Amide II mode is coupled to the NH stretch, whereas the NCO bending mode at 1082 cm^{-1} is coupled to the combination mode of the NH stretch and out-of-plane NH_2 band. As in the case of the x component of the transition dipole operator, a tenfold magnification of the signal for the lower spectrum in Fig. D.9 shows richer and more complicated coupling patterns. The Amide I normal mode at 1941 cm^{-1} and its couplings appear in the spectrum.

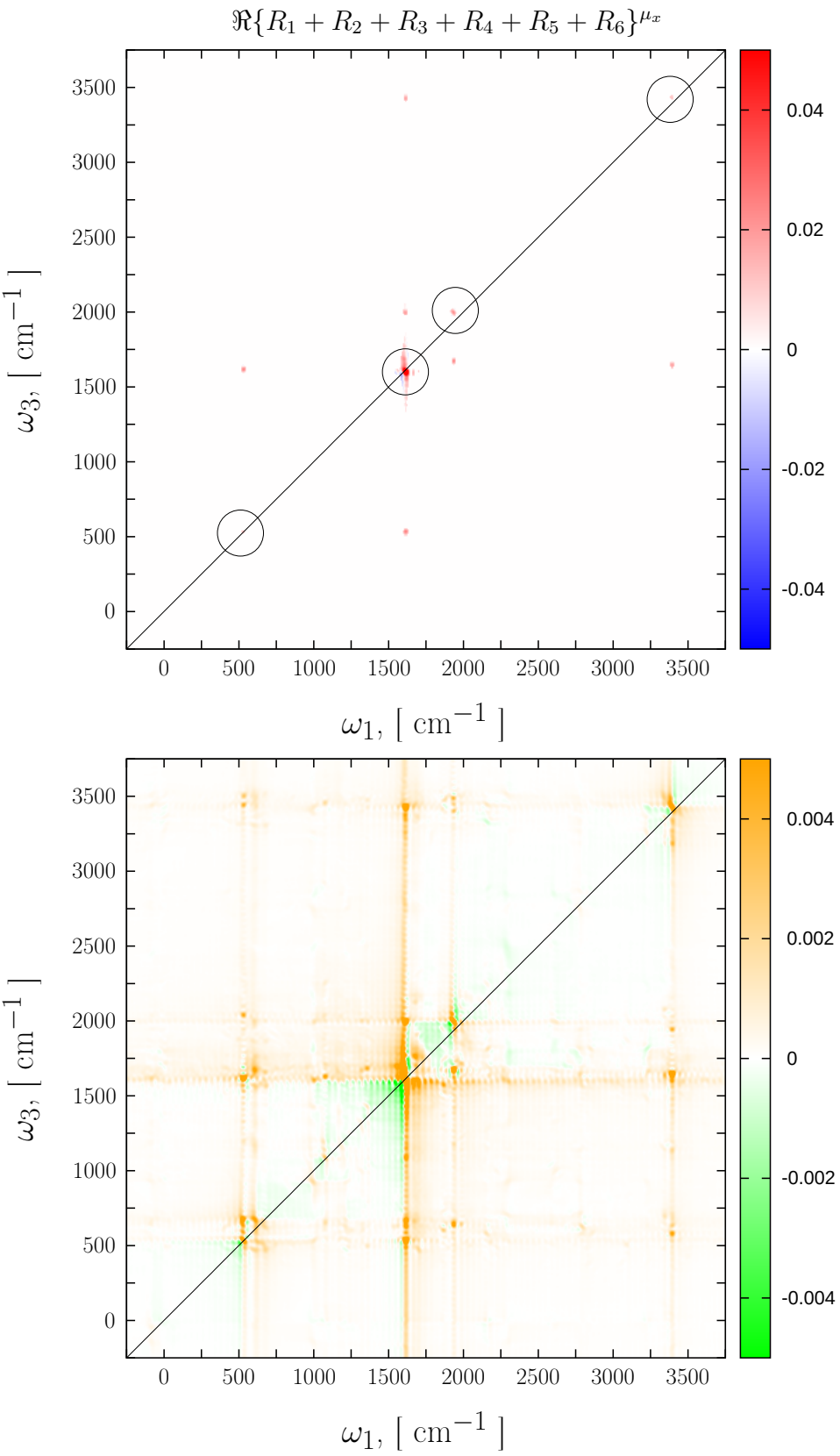

Figure D.8: The real parts of the third order response functions computed using the Monte Carlo Wave Packet Sampling approach (see Sec. C.03 and Sec. B.11) for the x component of the transition dipole moment of formamide. The lower spectrum is 10 times magnified.

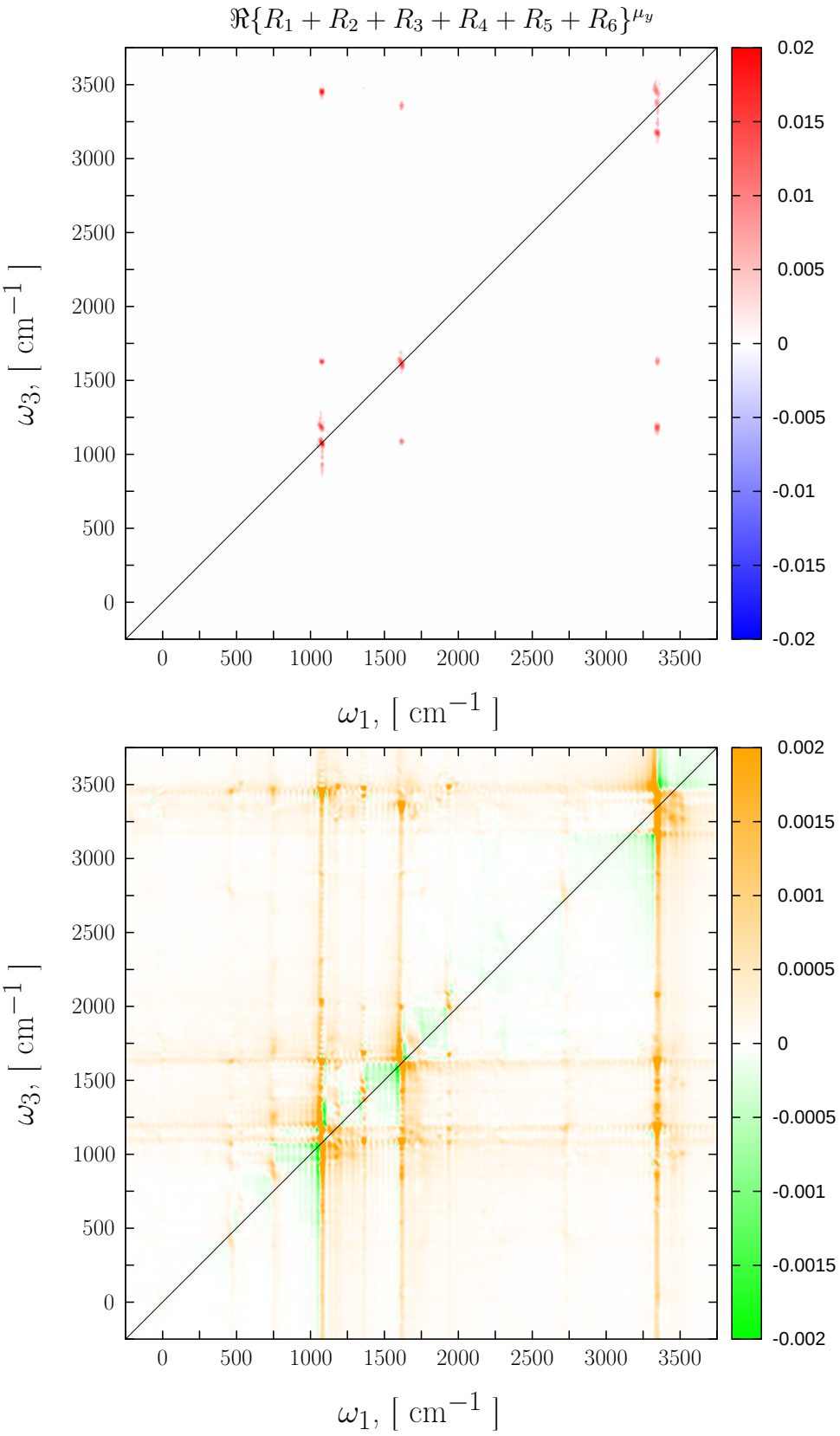

Figure D.9: The real parts of the third order response functions computed using the Monte Carlo Wave Packet Sampling approach (see Sec. C.03 and Sec. B.11) for the y component of the transition dipole moment of formamide. The lower spectrum is 10 times magnified.

The 2D signal associated with the z component of the transition dipole operator appears to be both simple and complicated at the same time. Simple because only few bands are visible in the normal (top spectrum of Fig. D.10) and the 25 times magnified (lower spectrum of Fig. D.10) spectra. The main complication of the signal is in the unusual structure of the bands. The most intensive band in the 1D spectrum appears not to be the out-of-plane NH_2 band, but the cross peak of the two out-of-plane bands at 112 and 535 cm^{-1}. That coupled motion has a huge dipole moment change associated with it, which explains its intensity. It is also coupled to NCO bending mode at 1082 cm^{-1} and NH stretch at 3351 cm^{-1}. Both normal modes do not appear by themselves in the spectrum, since both are in the xy plane of the molecule and therefore do not cause any change in the z component of the transition dipole matrix.

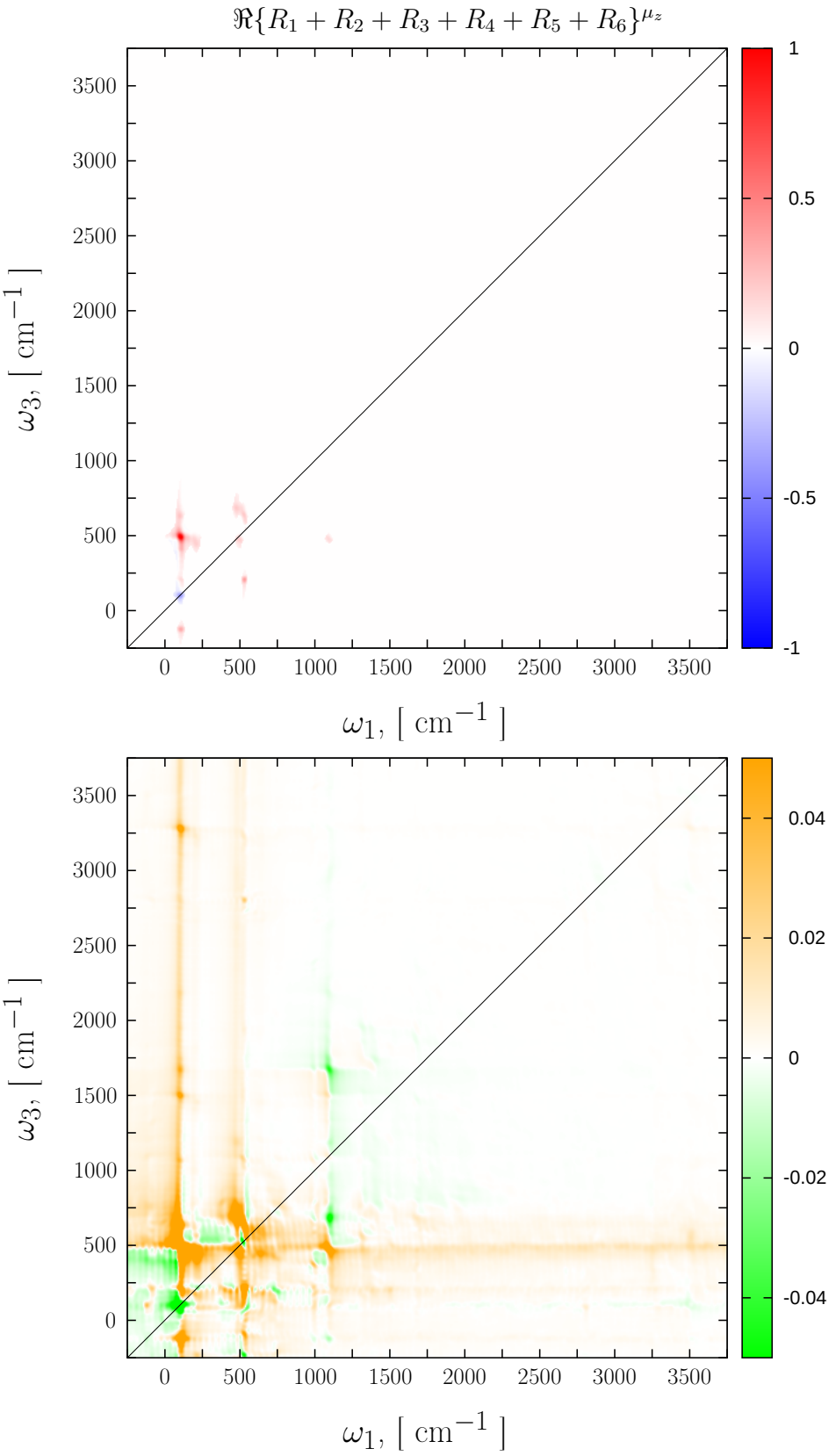

Figure D.10: The real parts of the third order response functions computed using the Monte Carlo Wave Packet Sampling approach (see Sec. C.03 and Sec. B.11) for the z component of the transition dipole moment of formamide. The lower spectrum is 25 times magnified.

Chapter E

Experimental inconveniences

The main purpose of the theory introduced in Chap. B and the methods developed in Chap. C is to understand the physics behind the spectral features and to be able to simulate (predict) multidimensional vibrational spectra. The first spectrum we have looked at was the carbon tetrachloride solution of 2-pyrrolidinone (see Fig. E.1). For this particular example we have found some discrepancies between

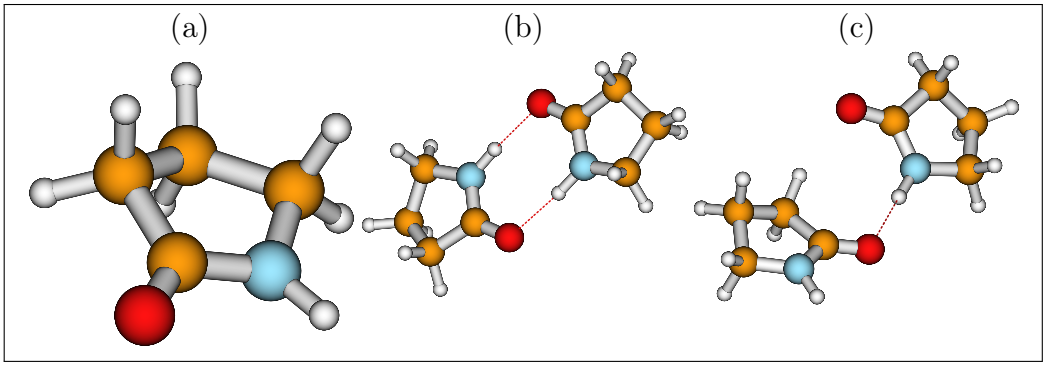

Figure E.1: a) 2-pyrrolidinone, b) doubly hydrogen bonded dimer (DHBD), c) single hydrogen bonded dimer (SHBD).

the theoretical expectations and the measured spectrum. Our investigation of those discrepancies is presented in this chapter, as well as it is published together with our experimental colleagues in Ref. [13].

E.01 Observations

The experimental one-dimensional FTIR absorption spectrum of 2-pyrrolidinone in carbon tetrachloride (1:50 volume concentration) measured in the mid IR spectral range (1500 - 3600 cm^{-1}) is presented in Fig. E.2 (top spectrum). The molecule 2-

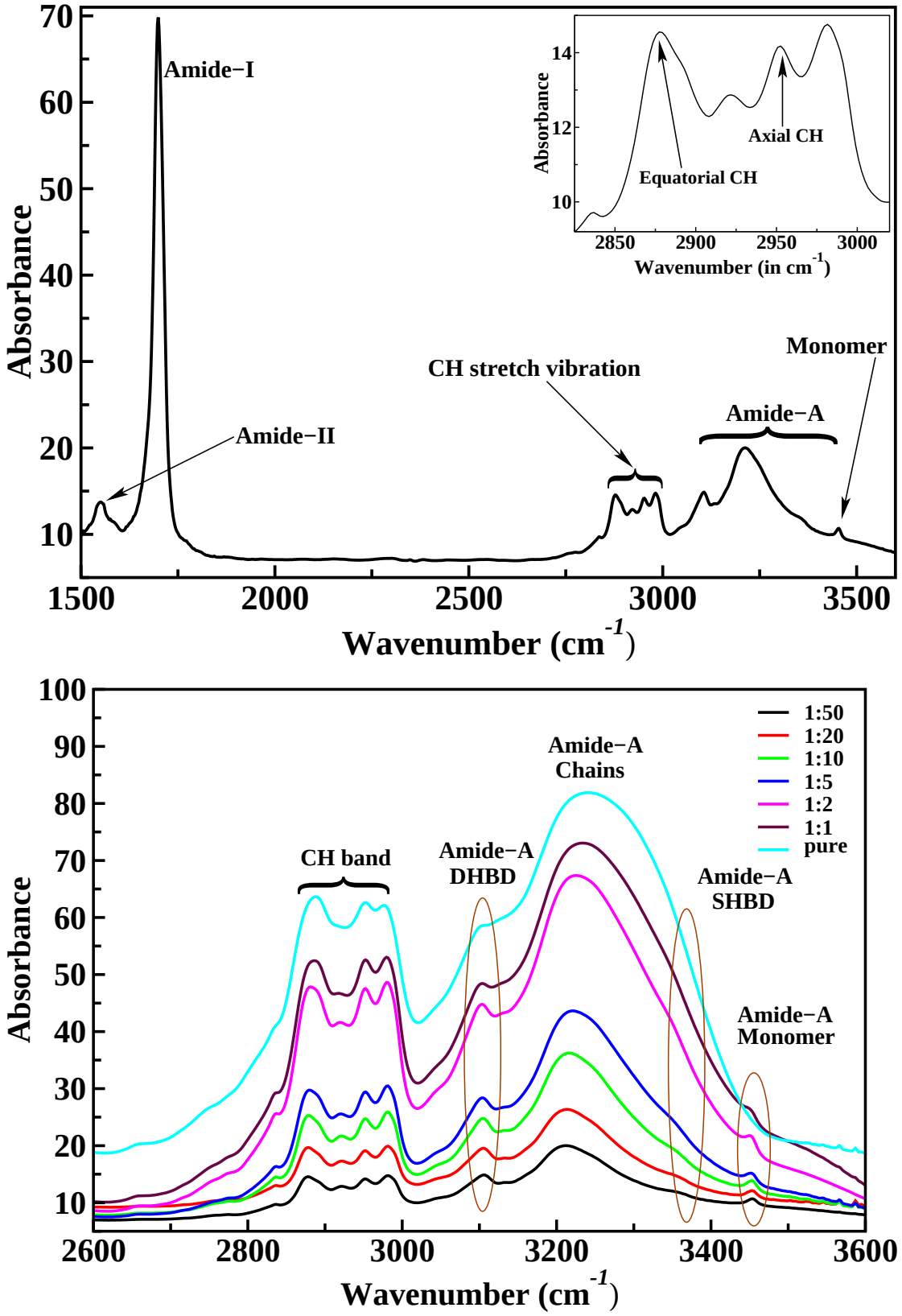

Figure E.2: Linear FTIR spectra of 2-pyrrolidinone in carbon tetrachloride at room temperature. Top spectrum at the sample concentration (1:50) and its inset is the enlarged view of the CH stretch vibrational band region. In the bottom spectrum the CH and amide-A vibrational band regions for different sample concentrations are shown.

pyrrolidinone is a γ-lactam* (see Fig. E.1–(a)) and we therefore expect the observed IR features to be related to the amide band and CH stretch vibrations. Indeed a very strong narrow peak (FWHM ~ 20 cm^{-1}) is observed at 1699 cm^{-1}. This well separated band is typical for an amide-I vibrational band which is essentially the CO double bond stretch vibration [46]. A narrow, small but well resolved peak is observed at 1550 cm^{-1}. This peak is assigned as amide-II band, which is basically a composition of CN stretch with the in-plane NH bending mode [47]. There is no noticeable feature in a broad spectral window between the amide-I band and ca. 2800 cm^{-1}. Four narrow small peaks are observed in the spectral range from 2837 cm^{-1} to 2977 cm^{-1}. They can be assigned to the CH stretch vibrational band [48] of the 2-pyrrolidinone molecule. The well resolved peak centered at 2878 cm^{-1} is strongly involved with the symmetric CH stretch vibration while the peak at 2952 cm^{-1} is involved with the antisymmetric CH stretch vibration [48]. We expect the amide-A band, which is essentially the NH stretch vibration of 2-pyrrolidinone, to be found at ca. 3450 cm^{-1} [48, 49]. And indeed a narrow small peak is observed at 3452 cm^{-1}. All the typical vibrational bands of a single 2-pyrrolidinone molecule appear at their expected spectral positions.

Yet, three peaks remain unassigned. The first peak, the most prominent feature of the vibrational spectrum, is a broad (FWHM ca. 165 cm^{-1}) absorption band centered at 3212 cm^{-1} partly covering a smaller and narrower second peak at ca. 3106 cm^{-1} as well as an even smaller third shoulder peak at 3360 cm^{-1}. The obvious question arises, what is the origin of these three peaks? In a recent work, Pandey *et.al.* [49] also found a similar broad band at 3212 cm^{-1} and they assigned it to the amide-A band from the doubly hydrogen bonded dimer (DHBD) of 2-pyrrolidinone but they did not comment on the smaller peaks.

Apart from hydrogen bond formation we also have to consider lactam-lactim tautomerization [50] as displayed in Fig. E.3. However, the lactim tautomer is

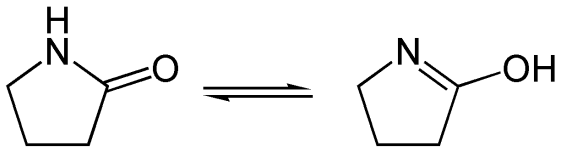

Figure E.3: Lactam-lactim-tautomerization [50].

found to be thermodynamically unfavorable and negligible at room temperature [51]. Also, the vibrational frequencies of the lactim OH have to be expected substantially higher than the monomer NH frequencies (about at 3600 cm^{-1}).

Amides like 2-pyrrolidinone are known to form intermolecular hydrogen bonds [52,53]. In particular 2-pyrrolidinone can form singly and doubly hydrogen bonded

*A lactam is a cyclic amide with $\beta = 2, \gamma = 3$, etc. carbon atoms outside the carbonyl bond.

species (see Fig. E.1). And since the frequencies of vibrations coupled by a hydrogen bond depend on the number and strengths of the hydrogen bonds [54], we expect different vibrational frequencies of singly and doubly hydrogen bonded dimers and larger oligomers.

Dimers of 2-pyrrolidinone are cyclic (see Fig. E.1–(b)) when they are doubly hydrogen bonded or linear (see Fig. E.1–(c)) when they are singly hydrogen bonded. Trimers and higher oligomers are expected to predominantly form linear chains, since ring formation becomes statistically very unfavourable for large oligomers. Therefore the broad absorption band at 3212 cm^{-1} is assumed to be caused by a distribution of 2-pyrrolidinone oligomers. This assumption will be studied in the next sections.

E.02 Quantum chemical and experimental insights

In this section we are going to compare the observations made in Sec. E.01 with theoretical results.

	EXP.	MP2		
		6-31G	6-31G† (Δ_{PCM})	TZVP
Amide-II	1522.16		1470.34 (-29)	1462.58
		1560.69	1559.43 (-15)	1506.45
Amide-I	1695	1684.46	1755.26 (-12)	1773.28
CH	2837	2904.08	2890.95 (7)	2899.46
CH	2883	2890.49	2877.84 (-38)	3003.43
CH	2920	2919.31	2917.14 (-5)	3044.17
CH	2952	2963.11	2955.85 (3)	3041.44
CH	2980	3000.47	2999.02 (19)	3040.74
		3014.34	3011.94 (-1)	3050.67
Amide-A	3452	3482.75	3558.96 (-10)	3498.74
Amide-A(g)	3473			

Table E.1: Selected set of anharmonic frequencies (in cm^{-1}) of 2-pyrrolidinone. 6-31G† is a combined 6-31G/6-31G** basis set. The numbers in brackets represent the frequency deviations (in cm^{-1}) induced by the solvent as modelled by the PCM approach (see text). The gas phase value of the amide-A frequency was taken from Ref. [49].

To describe the spectral features of the measured linear vibrational spectrum we first performed geometry optimizations of the monomer (Fig. E.1 – (a)) using MP2 and different basis sets (see Appendix G.01) within the GAUSSIAN package suite [55]. By 6-31G† we denote a combined 6-31G/6-31G** basis set, in which

6-31G** was used for O, N, and the H atom of the NH group, whereas 6-31G was used for all other atoms. The anharmonic frequencies were computed with the PT2 method [56, 57] at the same levels of theory. Results for selected modes with frequency assignments for the monomer are presented in Tab. E.1.

doubly hydrogen bonded dimer				singly hydrogen bonded dimer			
	EXP.	MP2			EXP.	MP2	
		6-31G	6-31G† (Δ_{PCM})			6-31G	6-31G† (Δ_{PCM})
NH		3087.72	3118.33 (-2)	NH	3360	3339.44	3331.36 (-16)
NH	3106	3238.60	3151.10 (94)	NH	3452	3478.45	3558.53 (-6)

Table E.2: Anharmonic frequencies (in cm^{-1}) of 2-pyrrolidinone double and single hydrogen bonded dimers. 6-31G† is a combined 6-31G/6-31G** basis set. The numbers in brackets represent the frequency deviations (in cm^{-1}) induced by the solvent as modelled by the PCM approach (see text).

The influence of the solvent (CCl_4) was examined for monomers and dimers based on the polarizable continuum model (PCM) with parameters ($\varepsilon_r = 2.2$ and scaled van der Waals surface cavity) built into GAUSSIAN [55]. The frequency deviations in wavenumbers introduced by PCM (presented in brackets as Δ_{PCM} values) for monomer and dimers are much smaller than the broadening effects studied in this work and therefore have negligible impact on the simulated spectra. Based on the monomer results, we optimized geometries (see Appendix G.01) and computed anharmonic frequencies for the double and single hydrogen bonded dimers (see Tab. E.2). Complete tables with the computed anharmonic frequencies can be found in Appendix G.02.

The frequencies computed with GAUSSIAN (see Tab. E.1 and Tab. E.2) are plotted together with a measured (1:50) spectrum in Fig. E.4. With the support of our calculations with different quantum chemical methods and basis sets we confirm the assignment of some questionable bands in the NH region: the amide-A of the doubly hydrogen bonded dimer at 3106 cm^{-1} and the amide-A of the singly hydrogen bonded dimer as the small peak at 3360 cm^{-1}. The main feature, the broad peak at 3212 cm^{-1} cannot be described by the frequencies of monomer or dimers and has to be approached differently.

The shortcoming of the monomer and dimer bands to explain the broad band at 3212 cm^{-1} supports the hypothesis of oligomer chains. To examine this hypothesis further, we perform a series of concentration dependent (2-pyrrolidinone in CCl_4) FTIR measurements [13]. The comparison between the volume and molar concentrations used is shown in Tab. E.3. The measurements are presented in the bottom spectrum of Fig. E.2. The absorption band at 3452 cm^{-1}, which we assigned to the amide-A from the 2-pyrrolidinone monomer, remains at the same spectral position irrespective of the sample concentration, only the relative peak

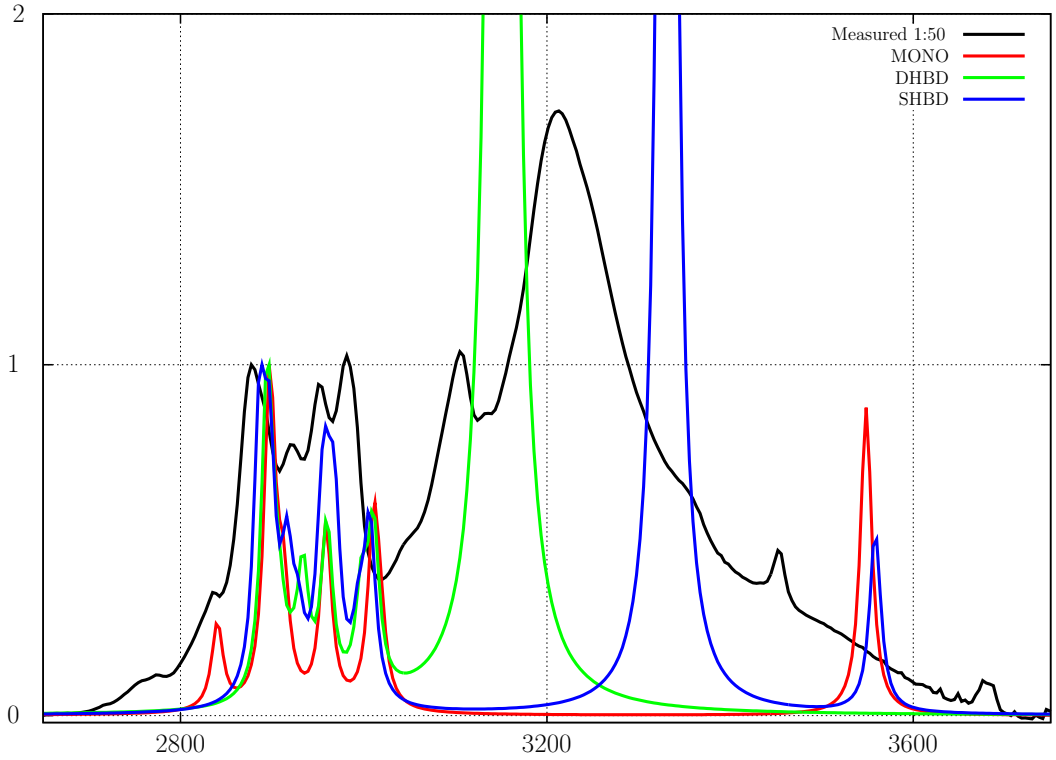

Figure E.4: Measured linear absorption spectrum of 1:50 (2-pyrrolidinone:CCl_4) solution, with MP2/6-31G† using PCM computed anharmonic spectra of 2-pyrrolidinone monomer, SHBD, and DHBD. The computed spectra were plotted as Lorentz-functions with FWHM=20 cm^{-1}. The maximum intensity of the CH band at $\approx$ 2900 was normalized to 1 for each spectrum, respectively.

size decreases with increasing sample concentration. In the pure sample, where the monomer concentration is expected to be very small, there is no peak observed at 3452 cm^{-1}. This is also in accordance with our assignment of the monomer's amide-A band.

The spectral shape and position of the peak at 3106 cm^{-1}, which we assigned to the doubly hydrogen bonded dimers, remains the same irrespective of the sample concentration. In contrast to the monomer peak intensity, the intensity of the amide-A band from the doubly hydrogen bonded dimers increases with increased sample concentration. This behavior reflects that the relative concentration of doubly hydrogen bonded dimers increases with the sample concentration.

The shape of the broad band centered at 3212 cm^{-1}, which we assigned to the amide-A band from singly hydrogen bonded chains of 2-pyrrolidinone, also depends on the sample concentration (see bottom spectrum in Fig. E.2). As the

$V(C_4NOH_7)$:$V(CCl_4)$	C, [mol/L]
1:0	13.1
1:1	6.6
1:2	4.4
1:5	2.2
1:10	1.2
1:20	0.6
1:50	0.2

Table E.3: Comparison between volume and molar concentrations used in the experiment.

sample concentration increases, the blue side edge of the peak falls faster than in the diluted sample. Specifically, the peak of the SHBD at 3360 cm^{-1} seems to gain more relative intensity as the concentration increases.

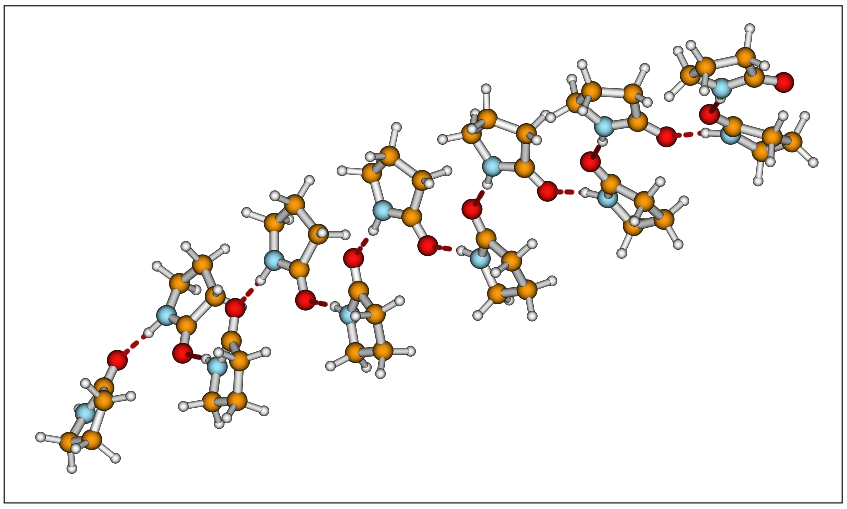

Figure E.5: 2-pyrrolidinone dodecamer.

In contrast, the CH_2 band shape and relative intensity does not depend on the sample concentration noticeably. This means, the CH_2 group is spectroscopically identical in all 2-pyrrolidinone species and can therefore always be calculated as in a monomer. In our calculation we find that the well separated peaks at 2955 cm^{-1} and 2890 cm^{-1}, have very local character and make up for most of the intensity of the CH vibrational band. The two peaks almost exclusively represent the axial (2955 cm^{-1}) and the equatorial (2890 cm^{-1}) CH stretch vibrations of the two CH bonds adjacent to the NH group. This assignment is of particular interest for dynamical experiments, like two-dimensional spectroscopy, since the axial and

equatorial CH bond interconvert as the 5-membered ring undergoes conformational change. Signatures of chemical exchange between equatorial and axial CH stretch vibrations have to be expected.

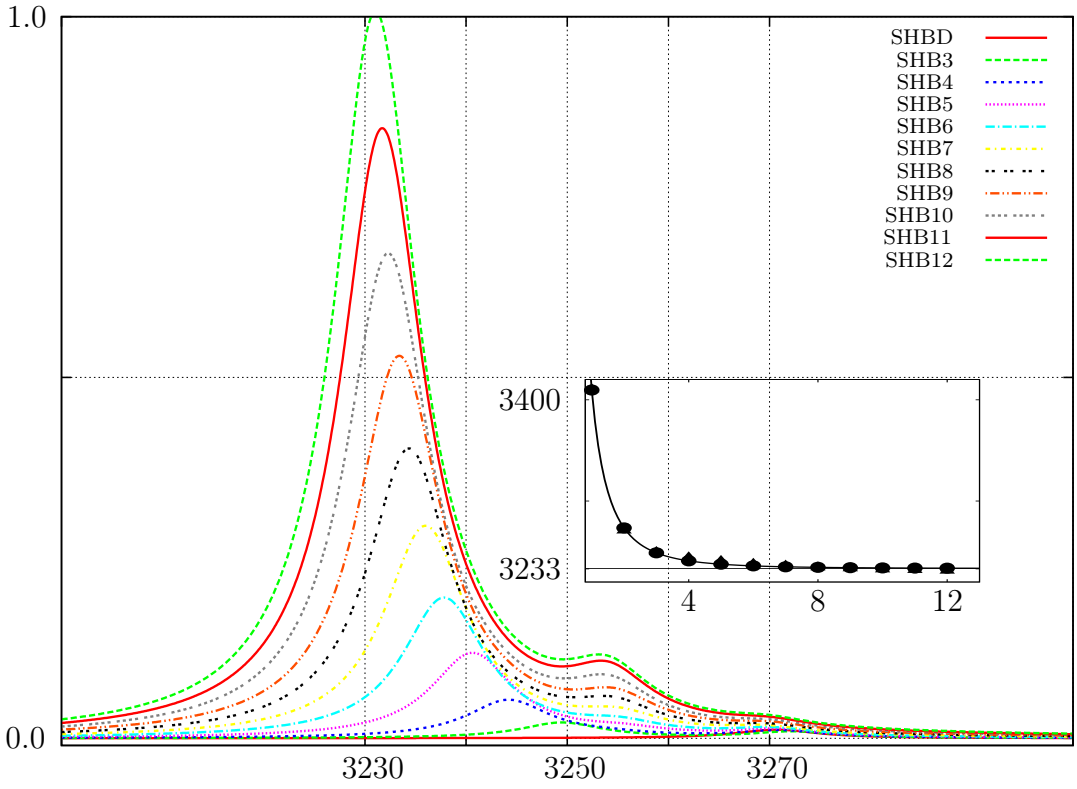

Figure E.6: Computed harmonic PM3 frequencies in wavenumbers for singly hydrogen bonded 2-pyrrolidinone chains plotted as Lorentz-functions with FWHM=100 cm^{-1}. The extrapolation of the lowest tight-binding eigenvalue for the infinite 2-pyrrolidinone chain is displayed in the inset (frequency as a function of chain length). See Sec. E.03 for details.

So far we were able to assign all but one spectral features and gain some indications that it originates from different 2-pyrrolidinone oligomers. In order to describe the vibrational frequencies of hydrogen bonded 2-pyrrolidinone oligomers, we first construct oligomer chains using the monomer geometry optimized with MP2 and 6-31G† basis set. Only the relative positions of the monomers to each other are optimized using the semiclassical PM3 method [44, 45]. The harmonic frequencies and their intensities are then computed with the PM3 method and presented in Fig. E.6 as Lorentz functions with FWHM=100 cm^{-1}. It is obvious that the harmonic frequencies cover the range between 3200 and 3400 cm^{-1}.

The anharmonic frequency computations are very expensive for oligomers. Therefore, we have to restrict the analysis of anharmonic effects in the buildup of the singly hydrogen bonded oligomer chains to the SHBD example. We found that the anharmonicity of the NH stretching mode is almost the same for the hydrogen bonded and the free NH mode. Its value for the 2-pyrrolidinone monomer is $\Delta_{\text{mono}} = 164$ cm^{-1}. Whereas the anharmonicity of the hydrogen bonded NH mode in SHBD is $\Delta_{\text{SHBD-NH-bond}} = 163$ cm^{-1} and the terminal (not hydrogen bonded) NH stretching mode is $\Delta_{\text{SHBD-NH-free}} = 166$ cm^{-1}. The influence of the hydrogen bonding on the anharmonic effects is very small (far bellow the expected broadening effects). Therefore the peak shifts observed in the spectrum can not be explained by the anharmonic effects and harmonic frequencies can be used for further approximations.

Another effect of 2-pyrrolidinone chains is the increasing dipole moment change and higher band intensity of the longer chains. This fact is supported by both the experiment (see Fig. E.2), in which the band at 3212 cm^{-1} has the highest intensity, as well as the harmonic frequency computation (see Fig. E.6), in which the intensity of red shifted bands (longer chains) is much higher than the intensity of blue shifted bands (shorter chains).

At this point we qualitatively understand the measured FTIR spectra. The next question would be, how does the concentration of 2-pyrrolidinone influence the distribution of oligomer concentrations and how does the latter influences the band intensity and shape? Further approximations have to be made for this purpose.

E.03 Vibrational tight-binding model

As the next approximation, we assumed an interaction Hamiltonian for the hydrogen bonded NH vibrational modes in the chain molecules, where the frequency of each hydrogen bonded NH stretch (α) is only influenced by its nearest neighbors through a coupling term (β), tight-binding (TB) interaction. The terminal NH bond (α') has a different frequency and is treated separately. The dimension of the model Hamiltonian matrix ($\mathbf{H}$) is given by the length (i.e. the number of NH oscillators) of the oligomer chain. Since we have computed harmonic frequencies for all chains from dimer to dodecamer, we obtain eleven matrices with dimensions from two to twelve. In the infinite ideal chain the matrix exhibits a band structure as shown in (E.03.1)

$$\mathbf{H} = \mathbf{H}_0 + \mathbf{H}' = \begin{pmatrix} \alpha & \beta & & & & & \\ \beta & \alpha & \beta & & & & \\ & & \ddots & & & & \\ & & & \beta & \alpha & \beta & \\ & & & & \beta & \alpha & \end{pmatrix} + \begin{pmatrix} 0 & 0 & & & & & \\ 0 & 0 & 0 & & & & \\ & & \ddots & & & & \\ & & & 0 & 0 & 0 & \\ & & & & 0 & \delta & \end{pmatrix}, \tag{E.03.1}$$

with $\delta = \alpha' - \alpha$. We assume that the harmonic frequencies from PM3 computations (λ) for different oligomers correspond to the eigenvalues of the same size TB-matrix. Since the TB-eigenvectors ($\mathbf{U}$) are well known, we can write

$$\widetilde{\lambda} = \mathbf{U}^T \mathbf{H} \mathbf{U} = f(\alpha, \beta, \alpha'). \tag{E.03.2}$$

It is obvious, that $\widetilde{\lambda}$ is a function of α, β, and α'. To estimate the optimal values of α, β, and α' for all oligomers simultaneously we solve the $\min(\lambda - \widetilde{\lambda}(\alpha, \beta, \alpha'))$ problem iteratively using the least-squares approach for all matrices at the same time. The resulting values are $\alpha = 3250$ cm^{-1}, $\beta = 7.6$ cm^{-1}, and $\alpha' = 3409$ cm^{-1}. These values are then used further for the Monte-Carlo simulations.

At first we inspect the case of the infinite straight 2-pyrrolidinone chain. We plot the lowest eigenvalues of the matrix $\mathbf{H}$ (the ones with the highest intensity) for all polymers computed with PM3 and fit these points to an exponential function using a least-squares approach (see the inset in Fig. E.6). With this function we estimate the asymptotic value of the lowest possible frequency of the infinite chain (3233 cm^{-1}), which is higher than the highest NH frequency (3151 cm^{-1}) of the doubly hydrogen bonded dimer. Since this asymptotic value is very close to the measured broad NH-band (3212 cm^{-1}) and anharmonic effects were found to be very small (see Sec. E.02), we will not apply any anharmonic corrections for the PM3 frequencies. Further, we assume that all geometry variations of the polymers in the solution that change vibrational frequencies are analogous to changes of the α and β values of the TB-matrix. Under those circumstances a statistical variation of α and β values will give us the inhomogeneously broadened spectrum of the considered oligomer.

We used the Monte-Carlo method [58] to compute the inhomogeneous broadening. The spectrum of each oligomer was treated separately. The variation of up to 30 wavenumbers for values of α and up to 5 wavenumbers for values of β was used in our Monte-Carlo sampling. After every Monte-Carlo step the eigenvalues of the changed TB matrix were computed. With these eigenvalues we compute a single homogeneously broadened Monte-Carlo spectrum (FWHM=100 cm^{-1}). The result of an average over 10000 such Monte-Carlo spectra gives us an inhomogeneously broadened spectrum. This procedure is repeated for every oligomer.

Since we assume that the Lambert-Beer law is valid for our system, we can compute the total vibrational spectrum as a sum of the computed DHBD and oligomer spectra multiplied with corresponding concentrations. Because the frequencies and intensities of SHBD were computed with both PM3 and MP2/6-31G† methods, we have scaled all PM3 intensities with the respective factor. The anharmonic frequencies of DHBD were used for the same reason. Since the model oligomer spectra include only NH frequencies and we expect CH normal modes to have mostly local character, we add the CH monomer spectrum multiplied by the total concentration in each case. As a result we expect a better reproduced CH region and higher intensity of the monomer NH band.

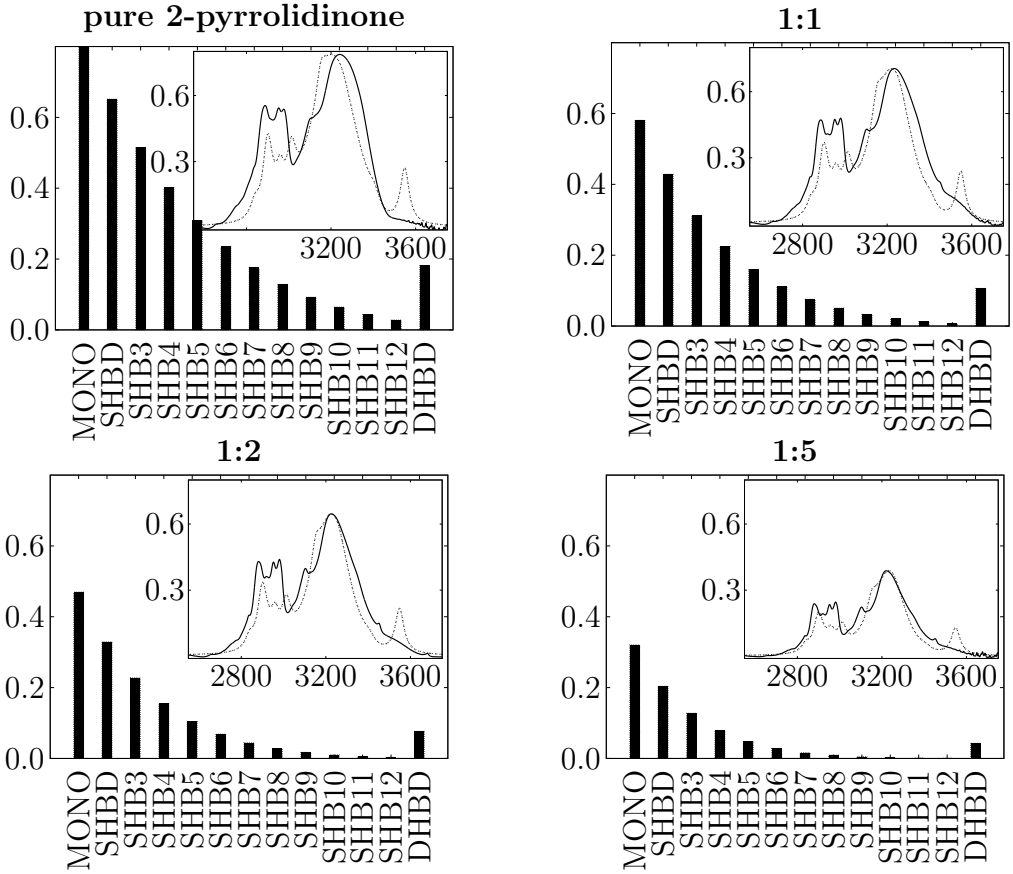

Figure E.7: This Figure is continued on page 89

The remaining question is how to get the concentrations of the computed species from the well-known total concentrations shown in Tab. E.3. We expect that the system is in equilibrium and assume that any chain size increasing reaction between any two reactants that leads to singly hydrogen bonded oligomers has the same rate. The reverse rate is set to be equal to the rate of the forward

reaction times a factor f.

$$k^{-1} = f \cdot k \tag{E.03.3}$$

The factor f ensures detailed balance and its computation goes far beyond the approximations made in our approach. We will simply treat it as variable to optimize. This assumption leads us to a classical textbook set of non-linear equilibrium equations. The set is defined by the rate of the forward reaction (k) and the parameter f.

The optimal values for k and f were found to be 0.01 and 10. Having these numbers one can solve the set of non-linear equations iteratively, which gives us concentrations of oligomers. The absolute concentrations in [mol/L] of all considered oligomers are displayed in the histograms in Fig. E.7. The singly hydrogen bonded oligomer chains are named SHBn with n being the chain length. Based on these concentrations we obtain sum spectra which we compare to the experimental results (see insets in Fig. E.7).

Considering all the approximations discussed above, the results seem surprisingly good. With such agreement between the experiment and theory, we may claim to understand the origins of the broad amide-A spectral feature, which was the main goal of this work.

Overall our model of hydrogen bonded 2-pyrrolidinone including chains reproduces the vibrational spectrum and specifically the amide-A band shape quite well considering its simplicity and lack of detailed rate constants for the hydrogen bond reactions of the different chain lengths. The quantitative details of the peak shape and position go beyond the scope of this work. Nevertheless, the comparison of spectra and calculations substantiates a microscopic picture of 2-pyrrolidinone in solution, where monomers, hydrogen bonded dimers and chains are in equilibrium with each other.

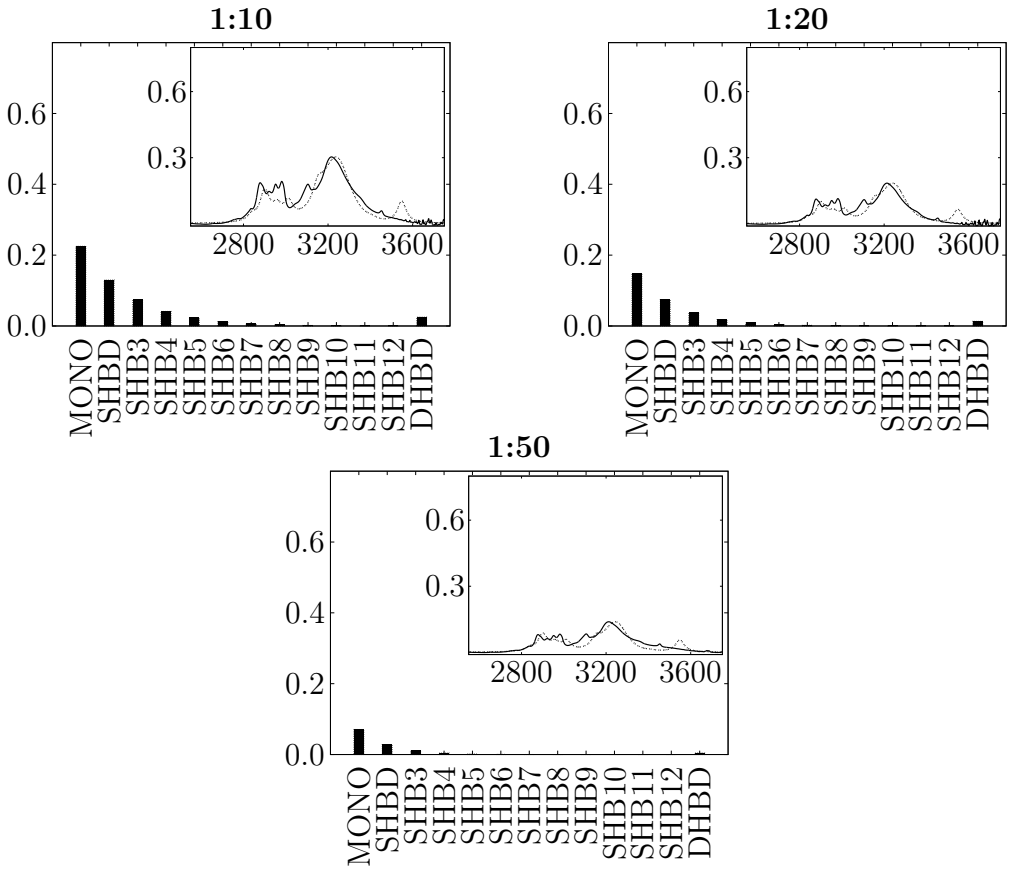

Figure E.7: Monomer and oligomer concentration distributions and corresponding measured (solid lines) and Monte-Carlo simulated (dashed lines) spectra displayed in the insets. The concentrations are given as absolute values in [mol/L]. The spectra are plotted in wavenumbers vs intensity. The intensities of the spectra are normalized with respect to the intensity of the CO-band of the pure 2-pyrrolidinone. The sum of the individual concentrations, each multiplied with the oligomer length, yield the total concentrations from Tab. E.3 (For details see text). First part of this figure is on page 87.

Chapter F

Conclusions and Outlook

In the course of this work we have developed a new method to compute multidimensional vibrational spectra based on the solution of a quantum stochastic differential equation in the doubled Hilbert space, which we call Monte Carlo sampling of Liouville space pathways. This method is based on the bottom-up buildup of the polarization function as a sum of its perturbative terms and is better suitable for the statistical sampling than the direct sampling of non-perturbative polarization functions in Liouville space mentioned in Sec. B.11.

Using the Monte Carlo sampling method we were able to go beyond very small systems or very crude approximations to obtain multidimensional vibrational spectra. We were able to compute third order response functions for systems with several thousands of states, which was not possible before to the best of our knowledge.

The Monte Carlo sampling method has some very distinct advantages. The first of them lies in its ability to simulate a very broad range of experiments starting with linear absorption and going to any number of pulse interactions. This may be necessary in the future, since every additional light-matter interaction of the system reveals more information about the system itself. For the example of formamide, we were able to show in Chap. D that the high intensity absorption band results from a combination of two out-of-plane bending modes and not just a fundamental transition. This example shows us that the signals in the linear absorption spectrum can be quite misleading and only higher order responses can reveal the real type of interaction underlying an apparently simple 1D spectrum. In the same way every additional interaction can unveil some new and important information about the system studied.

The next advantage of the Monte Carlo sampling method results from the way we build up the response functions as a sum of terms represented by Feynman diagrams. This approach allows us to choose the „important" perturbative terms beforehand on the basis of some approximations (rotating wave or low temperature approximations) and the distinct experiment we want to simulate. The chosen

Feynman diagrams can then be propagated and sampled independently. This way we have constructed an intrinsically parallel problem, that can be distributed via parallelization techniques in a straightforward manner across as many CPUs as terms in question.

The method presented in this work shows some very promising results but it still has a lot of space for further improvement. An open question so far is how to obtain elements of the relaxation matrix and their respective relaxation rates.

Chapter G

Appendices

G.01 Optimized geometries

- water
- PM3
- see Sec. D.01

	coordinates [Å]		
atoms	x	y	z
O	0.0000	0.0627	0.0000
H	0.7678	-0.4982	0.0000
H	-0.7678	-0.4982	0.0000

- formamide
- PM3
- see Sec. D.02

	coordinates [Å]		
atoms	x	y	z
O	1.1034	0.2411	0.0000
N	-1.1316	0.1741	0.0000
C	0.1061	-0.4610	0.0000
H	-1.2089	1.1632	0.0000
H	-1.9687	-0.3538	0.0000
H	0.1227	-1.5624	0.0000

- 2-pyrrolidinone
- MP2/6-31G†(PCM)
- see Sec. E.02

	coordinates [Å]		
atoms	x	y	z
H	-0.4910	-2.0224	-0.0155
N	-0.0876	-1.1001	-0.0853
C	-0.9061	0.0010	-0.0071
C	0.0072	1.2356	0.1356
C	1.4278	0.6975	-0.1856
C	1.3391	-0.8275	0.1361
O	-2.1464	-0.0134	-0.0356
H	1.9620	-1.4366	-0.5313
H	1.6316	-1.0397	1.1773
H	1.6518	0.8339	-1.2523
H	2.2173	1.1897	0.3949
H	-0.3268	2.0371	-0.5338
H	-0.0682	1.6063	1.1693

- doubly hydrogen bonded dimer
- MP2/6-31G†(PCM)
- see Sec. E.02

	coordinates [Å]		
atoms	x	y	z
H	-0.7618	-0.9885	0.0041
N	-1.7004	-0.5737	0.0303
C	-1.8778	0.7675	-0.0441
C	-3.3882	1.0518	-0.1329
C	-4.0383	-0.2997	0.2699
C	-2.9396	-1.3601	-0.0577
O	-0.9708	1.6364	-0.0568
H	-2.9223	-2.1901	0.6601
H	-3.0667	-1.7790	-1.0688
H	-4.2501	-0.3097	1.3479
H	-4.9746	-0.5041	-0.2635
H	-3.6588	1.8896	0.5205
H	-3.6338	1.3370	-1.1675
H	0.7635	0.9919	0.0047
N	1.7011	0.5746	0.0296
C	1.8770	-0.7668	-0.0442
C	3.3871	-1.0527	-0.1329
C	4.0389	0.2980	0.2697
C	2.9413	1.3596	-0.0573
O	0.9693	-1.6349	-0.0568
H	2.9246	2.1890	0.6612
H	3.0690	1.7793	-1.0680
H	4.2515	0.3077	1.3475
H	4.9751	0.5013	-0.2643
H	3.6565	-1.8907	0.5209
H	3.6325	-1.3387	-1.1673

- singly hydrogen bonded dimer
- MP2/6-31G†(PCM)
- see Sec. E.02

	coordinates [Å]		
atoms	x	y	z
H	3.4816	-1.8705	-0.7543
N	3.2041	-0.9624	-0.4129
C	1.9210	-0.7488	-0.0025
C	1.8544	0.6502	0.6277
C	3.1957	1.3108	0.2055
C	4.1532	0.1080	-0.0687
O	0.9887	-1.5748	-0.1147
H	4.8446	0.2961	-0.8998
H	4.7415	-0.1586	0.8235
H	3.0548	1.8874	-0.7185
H	3.6012	1.9848	0.9696
H	0.9599	1.1833	0.2820
H	1.7815	0.5328	1.7207
H	-0.7416	-0.8258	0.0372
N	-1.7030	-0.4812	0.0758
C	-2.0036	0.8208	-0.1948
C	-3.5404	0.9414	-0.2766
C	-4.0502	-0.3916	0.3324
C	-2.8633	-1.3811	0.1114
O	-1.1862	1.7501	-0.3597
H	-2.7636	-2.1122	0.9245
H	-2.9677	-1.9326	-0.8374
H	-4.2321	-0.2699	1.4092
H	-4.9763	-0.7539	-0.1310
H	-3.8821	1.8363	0.2571
H	-3.8289	1.0479	-1.3338

G.02 Anharmonic frequencies

2-pyrrolidinone

B3LYP	HCTH407		MP2					
6-31G	cc-pVDZ	TZVP	6-31G	6-31G†	6-31G**	6-311G**	cc-PVDZ	TZVP
137.06	142.10	146.69	138.90	131.66	139.91	140.12	137.48	132.74
191.63	182.92	178.88	184.50	172.22	206.78	215.13	218.67	202.71
461.53	457.24	460.44	459.25	457.41	467.06	465.53	464.93	458.90
511.37	473.23	470.08	503.16	465.96	485.00	478.54	483.85	467.07
603.26	549.30	555.48	581.09	548.20	550.40	548.21	540.49	539.22
661.21	624.99	626.53	628.14	631.36	639.35	632.84	629.56	631.34
684.17	680.38	682.13	674.25	691.21	679.37	679.96	669.82	693.46
815.16	782.03	784.46	816.18	812.49	824.69	814.40	811.65	813.59
876.46	857.66	854.70	880.32	882.74	901.86	887.62	885.72	883.66
905.37	869.25	876.63	909.76	909.88	921.36	907.84	900.91	911.25
921.51	896.70	891.65	931.63	928.45	937.62	926.98	927.72	925.58
994.04	976.73	977.39	997.12	1002.23	1014.54	1001.20	997.13	1001.99
1057.07	1032.34	1037.79	1054.59	1064.61	1085.49	1071.25	1065.15	1071.61
1099.15	1055.20	1053.98	1112.86	1109.63	1098.66	1081.16	1075.53	1083.34
1183.70	1128.89	1138.68	1192.32	1183.84	1191.02	1175.26	1161.35	1180.05
1209.03	1151.41	1167.70	1222.23	1213.75	1210.12	1190.69	1183.65	1194.12
1229.12	1184.12	1194.53	1238.14	1233.69	1249.31	1232.42	1220.52	1233.39
1245.75	1207.83	1219.69	1266.34	1260.88	1266.85	1247.82	1237.79	1253.97
1302.27	1228.84	1241.93	1320.40	1313.89	1314.58	1282.75	1277.24	1296.73
1330.03	1263.38	1273.35	1346.92	1339.73	1346.09	1323.91	1311.33	1330.55
1366.91	1304.24	1325.55	1375.62	1371.60	1369.20	1343.82	1335.26	1353.33
1432.66	1360.84	1390.78	1436.74	1433.49	1442.54	1418.95	1412.81	1423.70
1522.16	1376.20	1393.29	1481.99	1470.34	1500.16	1459.35	1417.50	1462.58
1444.53	1397.70	1419.68	1514.03	1511.67	1541.38	1497.15	1466.57	1498.33
1532.39	1479.27	1431.28	1560.69	1559.43	1536.19	1506.61	1404.93	1506.45
1712.87	1792.10	1754.14	1684.46	1755.26	1813.25	1803.64	1814.78	1773.28
2871.55	2819.76	2754.31	2904.08	2890.95	2941.43	2887.47	2849.29	2899.46
2945.79	2877.75	2876.80	2890.49	2877.84	3054.79	2993.21	2968.93	3003.43
2842.64	2877.14	2886.16	2919.31	2917.14	3023.05	3035.31	3010.85	3044.17
2944.92	2889.28	2899.88	2963.11	2955.85	3035.20	2996.49	3005.72	3041.44
2988.85	2913.50	2919.08	3000.47	2999.02	3080.10	3031.40	3036.99	3040.74
2996.47	2948.07	2942.21	3014.34	3011.94	3089.02	3040.70	3044.88	3050.67
3487.32	3454.18	3466.10	3482.75	3558.96	3550.98	3505.89	3484.59	3498.74

Anharmonic frequencies computed with GAUSSIAN [55] and PT2 [56, 57]. Refer to Sec. E.02 for details.

Hydrogen bonded dimers

doubly hydrogen bonded dimer				singly hydrogen bonded dimer			
B3LYP	HCTH407	MP2		B3LYP	HCTH407	MP2	
6-31G	cc-pVDZ	6-31G	6-31G†	6-31G	cc-pVDZ	6-31G	6-31G†
26.94	-2.65	20.49	15.84	3.88	5.47	10.07	14.46
60.36	37.84	55.53	51.49	27.26	33.50	29.90	33.94
88.89	65.32	83.92	77.64	74.04	75.36	67.33	62.40
100.84	128.42	92.76	88.10	76.37	49.17	64.38	66.95
110.64	52.97	103.28	102.48	89.23	73.84	85.95	90.29
134.84	82.44	138.59	146.38	118.19	113.49	112.47	112.71
141.18	141.24	143.99	146.73	142.13	150.40	138.65	151.62
151.21	147.40	140.97	150.93	159.18	166.32	161.88	161.99
206.94	188.65	200.21	188.84	201.81	183.17	195.93	174.63
216.73	189.44	206.42	191.03	205.80	183.49	196.06	189.96
469.47	456.37	467.52	468.57	464.81	475.34	463.99	464.05
496.38	460.94	491.49	497.27	476.46	475.87	474.01	475.07
545.05	520.51	539.43	543.00	521.17	491.75	516.86	484.70
553.54	529.04	545.59	547.00	547.98	525.45	540.25	544.54
632.61	610.42	633.66	633.14	614.63	562.34	597.41	566.30
638.79	616.52	635.55	636.52	632.76	613.11	630.97	629.43
691.37	677.12	687.70	681.62	666.79	621.69	645.76	631.73
698.65	669.25	693.09	687.48	690.25	666.84	685.14	677.17
818.43	745.26	821.48	814.67	694.32	690.27	688.08	696.91
819.59	778.11	823.28	817.83	815.55	719.55	818.29	764.83
883.27	777.96	882.09	815.63	825.41	783.91	827.80	806.98
884.88	776.91	886.39	860.28	880.82	790.34	833.02	822.57
904.26	860.40	874.62	888.05	881.43	861.82	884.12	887.18
900.65	864.26	911.02	882.96	877.67	867.81	881.84	890.73
921.60	869.31	912.33	915.83	910.92	869.41	914.09	915.06
922.61	868.96	930.70	916.57	911.90	869.82	915.92	915.47
925.05	900.97	931.43	929.71	919.22	900.88	931.13	927.67
964.32	898.98	918.89	929.82	924.38	900.04	935.41	932.83
1002.21	985.70	1004.47	1011.56	992.79	983.32	997.88	1003.35
1003.46	982.01	1007.34	1012.33	1001.88	983.41	1007.63	1011.17
1062.01	1034.87	1059.66	1077.11	1051.05	1031.97	1052.79	1061.39
1070.50	1035.84	1065.19	1083.32	1066.02	1034.77	1067.09	1080.79
1104.04	1091.73	1116.12	1112.68	1102.75	1053.93	1113.96	1110.91
1104.34	1073.47	1116.80	1113.35	1109.77	1083.46	1123.61	1122.24
1184.34	1125.73	1192.02	1182.54	1182.34	1123.40	1190.66	1181.28
1184.27	1126.82	1192.16	1183.55	1197.43	1132.34	1204.18	1194.74
1214.66	1156.77	1227.31	1221.40	1214.16	1153.21	1223.99	1217.70
1213.44	1157.20	1227.07	1221.76	1211.32	1164.11	1223.66	1220.53

1235.48	1185.54	1244.16	1241.75	1233.20	1178.60	1242.34	1239.69
1234.43	1186.03	1244.34	1242.25	1247.09	1192.64	1257.91	1255.13
1289.89	1217.02	1296.10	1297.74	1269.13	1219.21	1288.84	1284.41
1290.35	1220.66	1296.79	1299.08	1279.79	1232.51	1288.79	1286.67
1300.17	1248.23	1318.15	1314.97	1300.46	1244.95	1317.63	1314.63
1300.12	1251.01	1318.60	1315.34	1312.63	1246.29	1337.02	1335.16
1335.71	1267.30	1353.53	1351.47	1334.24	1263.79	1352.94	1345.04
1336.44	1269.81	1354.17	1353.25	1347.95	1273.89	1357.05	1352.00
1405.25	1344.82	1406.68	1400.70	1376.13	1314.28	1379.09	1375.16
1416.80	1353.89	1418.93	1422.80	1397.26	1366.49	1402.51	1395.65
1502.90	1355.11	1487.14	1495.54	1432.42	1355.04	1436.62	1439.11
1508.07	1363.88	1497.27	1502.64	1535.21	1368.53	1489.30	1484.27
1481.76	1382.03	1502.26	1500.70	1488.26	1382.83	1490.36	1483.62
1501.97	1382.90	1502.03	1496.90	1489.21	1383.47	1513.20	1517.93
1480.62	1440.12	1523.61	1522.42	1468.75	1401.92	1516.52	1514.73
1501.95	1448.10	1523.94	1530.38	1480.90	1469.21	1517.54	1515.08
1531.76	1465.61	1559.91	1556.92	1530.54	1463.39	1556.01	1556.85
1533.08	1449.88	1560.10	1557.92	1530.78	1477.49	1559.47	1555.92
1678.62	1722.65	1674.77	1720.17	1674.37	1750.59	1667.32	1724.53
1683.41	1756.89	1680.86	1741.79	1688.27	1764.49	1723.77	1747.38
2879.24	2784.52	2907.36	2894.57	2870.43	2802.70	2901.66	2885.99
2879.60	2812.15	2907.75	2894.68	2847.96	2818.82	2908.85	2897.00
2944.34	2865.99	2904.59	2902.57	2870.55	2852.45	2918.24	2917.48
2906.64	2865.81	2926.51	2908.68	2959.63	2854.53	2896.49	2887.17
2914.80	2861.23	2934.12	2933.57	2870.30	2863.99	2917.20	2915.67
2886.65	2861.15	2919.83	2921.41	2881.77	2865.93	2922.95	2928.56
2952.09	2898.09	2969.07	2959.89	2950.89	2866.66	2962.41	2954.12
2945.50	2898.15	2969.03	2959.83	2938.52	2865.70	2968.03	2959.14
2989.07	2900.01	2999.47	2997.67	3002.49	2906.98	2973.24	2967.93
2989.09	2900.17	2999.53	2997.59	2986.86	2931.69	2996.35	2994.63
2994.00	2914.13	3011.80	3010.75	2991.97	2937.37	3009.12	3007.79
2994.17	2915.18	3011.85	3010.66	2993.17	2917.24	3007.71	3005.55
2949.07	3063.01	3087.72	3118.33	3224.17	3266.20	3339.44	3331.36
3038.02	3056.83	3238.60	3151.10	3478.97	3448.37	3478.45	3558.53

Anharmonic frequencies computed with GAUSSIAN [55] and PT2 [56, 57]. Refer to Sec. E.02 for details.

Index

List of Figures

List of Tables

Bibliography

[1] P. Hamm and M. Zanni, *Concepts and methods of 2D infrared spectroscopy*. Cambridge University Press, 2011.

[2] E. B. Wilson, P. C. Cross, and J. C. Decius, *Molecular Vibrations: The Theory of Infrared and Raman Vibrational Spectra*. Dover, 1955.

[3] S. Krimm and J. Bandekar, "Vibrational spectroscopy and conformation of peptides, polypeptides, and proteins," vol. 38 of *Advances in Protein Chemistry*, pp. 181–364, USA: Academic Press, 1986.

[4] S. Mukamel, *Principles of Nonlinear Optical Spectroscopy*. USA: Oxford University Press, 1999.

[5] C. W. Gardiner, *Quantum Noise*. Springer-Verlag, 1991.

[6] S. Stenholm and M. Wilkens, "Jumps in quantum theory," *Contemporary Physics*, vol. 38, no. 4, pp. 257–268, 1997.

[7] H.-P. Breuer, B. Kappler, and F. Petruccione, "Stochastic wave-function approach to the calculation of multitime correlation functions of open quantum systems," *Phys. Rev. A*, vol. 56, no. 3, pp. 2334–2351, 1997.

[8] M. B. Plenio and P. L. Knight, "The quantum-jump approach to dissipative dynamics in quantum optics," *Rev. Mod. Phys.*, vol. 70, no. 1, pp. 101–144, 1998.

[9] T. Felbinger and M. Wilkens, "Stochastic wave-function simulation of two-time correlation functions," *J. Mod. Opt.*, vol. 46, no. 9, pp. 1401–1420, 1999.

[10] B. Wolfseder, *Modellrechnung zur Dynamik und zeitaufgelösten Spektroskopie von ultraschnellen Elektron-Transfer-Prozessen*. PhD thesis, Technische Universität München, 1997.

[11] B. Wolfseder and W. Domcke, "Multi-mode vibronic coupling with dissipation. application of the Monte Carlo wavefunction propagation method," *Chem. Phys. Lett.*, vol. 235, pp. 370–376, 1995.

[12] B. Wolfseder, L. Seidner, G. Stock, and W. Domcke, "Femtosecond pump-probe spectroscopy of electron-transfer systems: a nonperturbative approach," *Chem. Phys.*, vol. 217, pp. 275–287, 1997.

[13] K. S. Maiti, A. Samsonyuk, C. Scheurer, and T. Steinel, "Hydrogen bonding characteristics of 2-pyrrolidinone: a joint experimental and theoretical study," *Phys. Chem. Chem. Phys.*, vol. 14, pp. 16294–16300, 2012.

[14] K. Blum, *Density Matrix Theory and Applications*. New York, London: Plenum Press, 1996.

[15] H. Lütkepohl, *Handbook of Matrices*. Buffins Lane, Chichester, West Sussex: John Wiley and Sons, 1996.

[16] G. C. Schatz and M. A. Ratner, *Quantum Mechanics in Chemistry*. Mineola, New York: Dover, 2002.

[17] A. G. Redfield, "The theory of relaxation processes," *Adv. Mag. Reson.*, vol. 1, pp. 1–32, 1965.

[18] V. May and O. Kühn, *Charge and Energy Transfer Dynamics in Molecular Systems*. Berlin: Wiley-Vch, 2000.

[19] G. Lindblad, "On the generators of quantum dynamical semigroups," *Commun. Math. Phys.*, vol. 48, pp. 119–130, 1976.

[20] A. Kossakowski, "On quantum statistical mechanics of non-Hamiltonian systems," *Rep. Math. Phys.*, vol. 3, no. 4, pp. 247–274, 1972.

[21] J. Avery, *Creation and Annihilation Operators*. New York: McGraw-Hill, 1976.

[22] C. Moler and C. V. Loan, "Nineteen dubious ways to compute the exponential of a matrix," *SIAM Rev.*, vol. 20, no. 4, pp. 801–836, 1978.

[23] J. Dalibard, Y. Castin, and K. Mølmer, "Wave-function approach to dissipative processes in quantum optics," *Phys. Rev. Lett.*, vol. 68, pp. 580–583, Feb 1992.

[24] K. Mølmer, Y. Castin, and J. Dalibard, "Monte carlo wave-function method in quantum optics," *J. Opt. Soc. Am. B*, vol. 10, no. 3, pp. 524–538, 1993.

[25] W. Domcke. private communication.

[26] C. Scheurer. Theoretical Chemistry Toolkit.

[27] W. H. Louisell, *Quantum Statistical Properties of Radiation*. New York: John Wiley and Sons, 1973. Wiley Classics Library Edition Published 1990.

[28] K. Meyberg and P. Vachenauer, *Höhere Mathematik 2*. Berlin: Springer, 2003.

[29] Шилов and Гуревич, *Интеграл, мера и производная*. Москва: Наука, 1967.

[30] R. R. Ernst, G. Bodenhausen, and A. Wokaum, *Principles of nuclear magnetic resonance in one and two dimensions*. Oxford: Clarendon Press, 1991.

[31] H. Guo and R. Chen, "Short-time chebyshev propagator for the liouville-von neumann equation," *J. Chem. Phys.*, vol. 110, no. 14, pp. 6626–6634, 1999.

[32] C. Leforestier, R. H. Bisseling, C. Cerjan, M. D. Feit, R. Friesner, A. Guldberg, A. Hammerich, G. Jolicard, W. Karrlein, H.-D. Meyer, N. Lipkin, O. Roncero, and R. Kosloff, "A comparison of different propagation schemes for the time dependent schrödinger equation," *J. Chem. Phys.*, vol. 94, no. 1, pp. 59–80, 1991.

[33] G. Golub and C. V. Loan, *Matrix Computations*. The Johns Hopkins University Press, 3 ed., 1996.

[34] Y. Saad, *Iterative Methods for Sparse Linearsystems*. USA: International Thomson Publishing Inc., 1996.

[35] A. Meister, *Numerik linearer Gleichungssysteme*. Vieweg, 2 ed., 2005.

[36] A. Samsonyuk, "*Präkonditionierung des Eigenwertproblems im Schwingungs-CI Verfahren*." (Diplomarbeit, Technische Universität München), 2009.

[37] Open Multiprocessing (OpenMP). www.openmp.org.

[38] NumPy. Python and Scientific Computing. www.numpy.org.

[39] D. Strobush, *Ultrafast nonlinear IR spectroscopy on curved manifolds*. PhD thesis, Technische Universität München, in progress.

[40] M. Bounouar, *Theoretical Study of Anharmonic Vibrational Modes and Couplings with the VSCF Algorithm*. PhD thesis, Technische Universität München, 2007.

[41] K. Maiti, *High level ab initio potential energy surfaces and vibrational spectroscopy*. PhD thesis, Technische Universität München, 2007.

[42] A. Samsonyuk and C. Scheurer in progress.

[43] A. Samsonyuk and C. Scheurer, "Configuration space partitioning and matrix buildup scaling for the vibrational configuration interaction method," *J. Comp. Chem.*, vol. 34, pp. 27–37, 2013.

[44] J. J. P. Stewart, "Optimization of Parameters for Semiempirical Methods I. Method," *J. Comp. Chem.*, vol. 10, no. 2, pp. 209–220, 1989.

[45] J. J. P. Stewart, "Optimization of Parameters for Semiempirical Methods II. Applications," *J. Comp. Chem.*, vol. 10, no. 2, pp. 221–264, 1989.

[46] A. Warshel, I. K. Levitt, and S. Lifson, "Consistent force field for calculation of vibrational spectra and conformations of some Amides and Lactam rings," *J. Mol. Spec.*, vol. 33, pp. 84–99, 1970.

[47] L. P. DeFlores, Z. Ganim, R. A. Nicodemus, and A. Tokmakoff, "Amide I–II: 2D IR Spectroscopy Provides Enhanced Protein Secondary Structural Sensitivity," *Journal of the American Chemical Society*, vol. 131, no. 9, pp. 3385–3391, 2009.

[48] D. P. McDermott, "Vibrational assignments and normal-coordinate analyses of γ-Butyrolactone and 2-Pyrrolidinones," *J. Phys. Chem.*, vol. 90, no. 12, pp. 2569–2574, 1986.

[49] P. Pandey, A. K. Samanta, B. Bandyopadhyay, and T. Chakraborty *Vibrational Spectroscopy*, vol. 55, pp. 126–131, 2011.

[50] M. B. Smith and J. March, *March's Advanced Organic Chemistry: Reactions, Mechanisms, and Structure*. New York: John Wiley and Sons, 2001.

[51] A. E. Shchavlev, A. N. Pankratov, V. B. Borodulin, and O. A. Chaplygina, "DFT Study of the Monomers and Dimers of 2-Pyrrolidone: Equilibrium Structures, Vibrational, Orbital, Topological, and NBO Analysis of Hydrogen-Bond Interactions," *J. Phy. Chem. A*, vol. 109, pp. 10982–10996, 2005.

[52] H. Chung and A. Tokmakoff, "Temperature dependent downhill unfolding of ubiquitin. I. Nanosecond-to-millisecond resolved nonlinear infrared spectroscopy," *Proteins-Structure Function and BioInformatics*, vol. 72, no. 1, pp. 474–487, 2008.

[53] Z. Ganim, H. S. Chung, A. W. Smith, L. P. DeFlores, K. C. Jones, and A. Tokmakoff, "Amide I Two-Dimensional Infrared Spectroscopy of Proteins," *Acc. Chem. Res.*, vol. 41, no. 3, pp. 432–441, 2008.

[54] A. Novak, "Hydrogen bonding in solids," in *Structure and Bonding* (J. D. Dunitz, ed.), p. 177, Springer-Verlag: Berlin, 1974.

[55] M. J. Frisch, G. W. Trucks, H. B. Schlegel, G. E. Scuseria, M. A. Robb, J. R. Cheeseman, J. A. Montgomery, Jr., T. Vreven, K. N. Kudin, J. C. Burant, J. M. Millam, S. S. Iyengar, J. Tomasi, V. Barone, B. Mennucci, M. Cossi, G. Scalmani, N. Rega, G. A. Petersson, H. Nakatsuji, M. Hada, M. Ehara, K. Toyota, R. Fukuda, J. Hasegawa, M. Ishida, T. Nakajima, Y. Honda, O. Kitao, H. Nakai, M. Klene, X. Li, J. E. Knox, H. P. Hratchian, J. B. Cross, V. Bakken, C. Adamo, J. Jaramillo, R. Gomperts, R. E. Stratmann, O. Yazyev, A. J. Austin, R. Cammi, C. Pomelli, J. W. Ochterski, P. Y. Ayala, K. Morokuma, G. A. Voth, P. Salvador, J. J. Dannenberg, V. G. Zakrzewski, S. Dapprich, A. D. Daniels, M. C. Strain, O. Farkas, D. K. Malick, A. D. Rabuck, K. Raghavachari, J. B. Foresman, J. V. Ortiz, Q. Cui, A. G. Baboul, S. Clifford, J. Cioslowski, B. B. Stefanov, G. Liu, A. Liashenko, P. Piskorz, I. Komaromi, R. L. Martin, D. J. Fox, T. Keith, M. A. Al-Laham, C. Y. Peng, A. Nanayakkara, M. Challacombe, P. M. W. Gill, B. Johnson, W. Chen, M. W. Wong, C. Gonzalez, and J. A. Pople, "Gaussian 03, Revision C.02." Gaussian, Inc., Wallingford, CT, 2004.

[56] V. Barone, "Vibrational zero-point energies and thermodynamic functions beyond the harmonic approximation," *J. Chem. Phys.*, vol. 120, pp. 3059–3065, 2004.

[57] V. Barone, "Anharmonic vibrational properties by a fully automated second order perturbative approach," *J. Chem. Phys.*, vol. 122, p. 014108, 2005.

[58] D. Frenkel and B. Smit, *Understanding Molecular Simulations. From Algorithms to Applications.* USA: Academic Press, 2 ed., 2002.

Acknowledgements

So Long, and Thanks for All the Fish

Douglas Adams

There are many people to whom i owe my deepest gratitude for their friendship, support and help at the moments i needed it most:

- to Prof. Wolfgang Domcke and Dr. Christoph Scheurer, who taught me quantum mechanics, provided me with work, advise and help throughout my undergraduate and graduate studies;
- to Dr. Christoph Scheurer for supervising me during my diploma and PhD theses, for teaching me concepts of programming and system administration;
- to Dr. Maxim Gelin for being a great listener and showing me ways out from some dead ends in my research;
- to Ruth Mösch for being able to see the light at the end of the tunnel in all the bureaucracy;
- to all group members and non-theoretical friends for all the awesome boardgames, trainings, stage fights and tournaments, hikes, movies and a lot of other theoretical and practical fun;
- to my family for their love and continuous support for all these years.